

## ABSTRACT

Title of dissertation: Measurement of  $W\gamma\gamma$  Cross Section  
and Limits on Anomalous Quartic Gauge Couplings  
in Proton-Proton Collisions at 8 TeV  
with the CMS Detector

Christopher Anelli, Doctor of Philosophy, 2016  
University of Maryland Department of Physics

Dissertation directed by: Assistant Professor A. Belloni

Present the measurement of a rare Standard Model processes,  $pp \rightarrow W^\pm\gamma\gamma$  for the leptonic decays of the  $W^\pm$ . The measurement is made with  $19.4 \text{ fb}^{-1}$  of 8 TeV data collected in 2012 by the CMS experiment. The measured cross section is consistent with the Standard Model prediction and has a significance of  $2.9\sigma$ . Limits are placed on dimension-8 Effective Field Theories of anomalous Quartic Gauge Couplings. The analysis has particularly sensitivity to the  $f_{T,0}$  coupling and a 95% confidence limit is placed at  $-35.9 < \frac{f_{T,0}}{\Lambda^4} < 36.7 \text{ TeV}^{-4}$ . Studies of the  $pp \rightarrow Z\gamma\gamma$  process are also presented. The  $Z\gamma\gamma$  signal is in strict agreement with the Standard Model and has a significance of  $5.9\sigma$ .

Measurement of  $W\gamma\gamma$  Cross Section and Limits on Anomalous  
Quartic Gauge Couplings in Proton-Proton Collisions at 8 TeV  
with the CMS Detector

by

Christopher Ryan Anelli

Dissertation submitted to the Faculty of the Graduate School of the  
University of Maryland, College Park in partial fulfillment  
of the requirements for the degree of  
Doctor of Philosophy  
2016

Advisory Committee:

Assistant Professor Alberto Belloni, Chair

Professor Sarah Eno

Professor Abolhassan Jawahery

Associate Professor Zackaria Chacko

Professor Alice Mignerey, Dean's Representative

© Copyright by  
Christopher Anelli  
2016

## Dedication

To my parents Sheila and James,  
and sisters Lauren and Caitlin

## Acknowledgments

Many hands helped to make this thesis possible. The individuals acknowledged below represent only a partial list of those who gave generously of their time and effort.

I thank my advisor, Alberto Belloni, and the faculty and staff of the Maryland CMS group: Sarah Eno, Nick Hadley, Shabnam Jabeen, and Richard Kellogg. Special acknowledgement to Marguerite Tonjes for her management of the Tier 3 Cluster. I thank my fellow graduate students, Brian Calvert, Kevin Pedro, and Young Ho Shin, I could not have wished to work alongside a better group of students. I also express my gratitude to my analysis partners, Josh Kunkle. He patiently shared his knowledge of high energy physics and was an invaluable research mentor.

Lastly, I am fortunate to have met and become good friends with Alex Jeffers and David Angelaszek. I could not have made it through graduate school without their support, and I am indebted to them for many great memories.

# Contents

Table of Contents	iv
List of Tables	vii
List of Figures	ix
List of Abbreviations	xii
1 Introduction	1
2 Theory	4
2.1 Review of the Standard Model . . . . .	4
2.1.1 Leptons . . . . .	4
2.1.2 Quarks . . . . .	5
2.1.3 Gauge Bosons . . . . .	6
2.1.4 Quantum Field Theory . . . . .	7
2.1.4.1 Quantum Chromodynamics $SU(3)_C$ . . . . .	8
2.1.4.2 Electroweak Theory $SU(2)_L \times U(1)_Y$ . . . . .	9
2.1.5 Symmetry Breaking and the Higgs Boson . . . . .	11
2.1.6 Beyond the Standard Model . . . . .	11
2.2 Vector Gauge Couplings . . . . .	12
2.3 $W\gamma\gamma$ Production . . . . .	14
2.4 Anomalous Gauge Couplings . . . . .	15
2.4.1 Effective Field Theories . . . . .	16
2.4.2 Anomalous Couplings . . . . .	19
2.4.3 Unitarity . . . . .	20
3 Experiment	22
3.1 The Large Hadron Collider . . . . .	22
3.2 The Compact Muon Solenoid Detector . . . . .	27
3.2.1 Position Notation . . . . .	27
3.2.2 Inner Tracking System . . . . .	29
3.2.3 Electromagnetic Calorimeter . . . . .	29
3.2.4 Hadron Calorimeter . . . . .	31
3.2.5 Superconducting Magnet . . . . .	32
3.2.6 Muon System . . . . .	33
3.2.7 Triggers . . . . .	34
3.2.7.1 HO Minimum Ionization Bit Trigger . . . . .	35
4 Event Reconstruction	39
4.1 Track and Vertex Reconstruction . . . . .	40
4.2 Muon Reconstruction . . . . .	41
4.3 Electron Reconstruction . . . . .	43
4.4 Photon Reconstruction . . . . .	45

4.5	Particle-Flow . . . . .	46
4.6	Jet Reconstruction . . . . .	48
4.7	MET Reconstruction . . . . .	49
5	Event Simulation . . . . .	51
5.1	Generators . . . . .	51
5.2	PDF . . . . .	53
5.3	Reweighting . . . . .	55
5.4	Dressing Leptons . . . . .	56
5.5	Detector Simulation . . . . .	58
6	Data Analysis . . . . .	59
6.1	Samples . . . . .	60
6.1.1	Data Samples . . . . .	60
6.1.2	Monte Carlo Samples . . . . .	61
6.1.2.1	$W\gamma\gamma$ Samples . . . . .	61
6.1.2.2	aQGC Samples . . . . .	64
6.1.2.3	Background Samples . . . . .	65
6.1.2.4	Corrections to Monte Carlo . . . . .	65
6.2	Object and Event Selection . . . . .	66
6.2.1	Muon Selection . . . . .	66
6.2.2	Electron Selection . . . . .	68
6.2.3	Photon Selection . . . . .	68
6.2.4	Overlap Removal . . . . .	69
6.2.5	Event Selection . . . . .	69
6.3	Background Estimation . . . . .	71
6.3.1	Jets Faking Photons . . . . .	71
6.3.2	Electrons Faking Photons . . . . .	74
6.3.3	$Z\gamma\gamma$ Background . . . . .	74
6.3.4	Other Diphoton Backgrounds . . . . .	75
6.3.5	Negligible Backgrounds . . . . .	75
6.4	Summary of Signal and Background . . . . .	76
6.5	Fiducial Cross Section . . . . .	76
6.5.1	Definition of Fiducial Region . . . . .	77
6.5.2	Fiducial Acceptance . . . . .	78
6.5.3	$\tau$ Subtraction . . . . .	79
6.6	Selection for aQGC Study . . . . .	80
7	Statistical and Systematic Uncertainties . . . . .	83
7.1	Statistical Uncertainties . . . . .	83
7.2	Signal Simulation Systematics . . . . .	85
7.3	Background Systematics . . . . .	87

8	Results	90
8.1	Combined Cross Section . . . . .	90
8.1.1	Significance . . . . .	92
8.2	Limit Setting . . . . .	92
8.3	Other Triboson Measurements . . . . .	95
9	Extensions to $Z\gamma\gamma$	96
9.1	Feynman Diagrams . . . . .	96
9.2	Selection . . . . .	97
9.3	Backgrounds . . . . .	98
9.4	Fiducial Region . . . . .	98
9.5	Systematics . . . . .	99
9.6	Results . . . . .	100
10	Conclusion	102
A	Appendix	103
A.1	Unitarity . . . . .	103
A.2	Pseudorapidity . . . . .	104
A.3	Collision Energy Loss . . . . .	104
A.4	Blue Combination . . . . .	105
A.5	Optimization of Limit Setting . . . . .	105
	Bibliography	107



## List of Tables

2.1	Values of the weak isospin, the weak hypercharge, and the electric charge for the quarks and leptons. Quarks and leptons are broken up between the left-handed doublets and the right-handed singlets. . . .	10
4.1	Seed types and the selection criteria for the six iterations of the Combinatorial Track Finder . . . . .	41
6.1	Single lepton data sets from the CMS 2012 Run. Electron and muon channel each corresponds to an integrated luminosity of $19.4 \text{ fb}^{-1}$ . . .	61
6.2	List of Monte Carlo $W\gamma\gamma$ signal and backgrounds samples. The table gives the CMS Data Aggregation Service (DAS) name and the sample's full cross section. . . . .	62
6.3	The range and step sizes for Anomalous Quartic Couplings generated. Produced using the MadGraph Reweighting tool. . . . .	64
6.4	Summary table of the background estimates, the expected $W\gamma\gamma$ signal, and the number of observed events in the data. Estimates are broken up between the different regions of the detector. The expected number of signal and background events are normalized to the integrated luminosity for the data sample collected, $19.4 \text{ fb}^{-1}$ . . . . .	77
6.5	Definition of the Fiducial Region used for the $W\gamma\gamma$ Cross-Section measurements. $M_T$ is the transverse mass of the Candidate Lepton and Neutrino(s). . . . .	77
6.6	Fiducial Cut Flow for the $W\gamma\gamma$ signal. Weighted combination of ISR and FSR samples normalized to the $19.4 \text{ fb}^{-1}$ luminosity. . . . .	78
6.7	$\frac{C_{W\gamma\gamma}}{1-f_\tau}$ as function of Lead Photon $p_T$ with statistical and systematic errors. "Total" is the $\frac{C_{W\gamma\gamma}}{1-f_\tau}$ for all events with lead photon $p_T$ above 25 GeV . . . . .	80
7.1	Systematic and statistical uncertainties effecting the $W\gamma\gamma$ fiducial cross section measurement in the electron and muon channels. . . .	84
7.2	Systematic uncertainties on the expected number of $W\gamma\gamma$ reconstructed events. These are for the events with lead photon $p_T > 70 \text{ GeV}$ , separated between the electron and muon channel and by $\eta^\gamma\eta^\gamma$ . These values are used as nuisance parameters in the aQGC limit setting. . . . .	84
8.1	95% exclusion limits on the anomalous couplings for the combined electron and muon channels . . . . .	94
8.2	Comparison of the limits set on the $f_{T,0}$ coupling for the ATLAS $W\gamma\gamma$ , CMS $W\gamma\gamma$ and CMS $WV\gamma$ analyses. . . . .	95
9.1	Estimated background events, observed data, and expected signal for the $Z\gamma\gamma$ analysis. Results are separated by channel and photon region.	98

9.2	Definition of the Fiducial Region used for the $Z\gamma\gamma$ Cross-Section measurements. . . . .	99
9.3	For the $Z\gamma\gamma$ analysis, total fiducial acceptance factor divided by $1 - f_\tau$ for the electron and muon channels. . . . .	99
9.4	Systematic and statistical uncertainties affecting the $Z\gamma\gamma$ fiducial cross section for events with a leading photon having $p_T > 15$ GeV. . . . .	100
A.1	Unitarity bounds for the couplings considered in this analysis. Bounds are the vertex energy at which a theory with the given energy would violate unitarity. . . . .	104
A.2	Generator systematics for the expected number of $W\gamma\gamma$ events at $19.4 \text{ fb}^{-1}$ . MadGraph NLO calculation. The electron and muon channel are combined using the BLUE method. . . . .	106
A.3	Expected and observed limits on $f_{T,0}$ as a function of the sublead photon $p_T$ cut . . . . .	106

## List of Figures

2.1	Table of the Elementary Particles. The particles are arranged by type, the leptons, the quarks, the gauge bosons, and the recently discovered scalar Higgs Boson. . . . .	5
2.2	Diagram of the ground states of the Higgs field. From Griffiths [9] . . .	12
2.3	Feynman Diagram of Quartic Gauge Coupling in the $W\gamma\gamma$ process. All three bosons come from the same vertex, the coupling strength of which is prescribe by the structure of Electroweak theory and the values of physical constants. . . . .	15
2.4	Feynman Diagram on the left shows $W\gamma\gamma$ production where the photons are from triple gauge coupling (TGC) + ISR. Diagram on the right shows an example of photons radiated through ISR + FSR. . . .	16
2.5	Cross section of the $\mathcal{L}_{M,0}$ , $\mathcal{L}_{M,2}$ , and SM theories as a function of lead photon $p_T$ . The $\mathcal{L}_{M,0}$ and $\mathcal{L}_{M,2}$ operators contribute in the same underlying way to the WWAA vertex, only with coefficients differing by a factor of $2\frac{\cos^2\theta_w}{\sin^2\theta_w} \sim 7$ . . . . .	19
3.1	Layout of the LHC. The path of the two beams are shown in red and blue, and the location of the four main detectors at the beam crossings are indicated by stars. . . . .	23
3.2	Cumulative integrated luminosity for the CMS detector over the 2012 run at a center-of-mass energy of 8 TeV. . . . .	23
3.3	Cross section of an LHC cryodipole magnet showing the two beam pipes and the “twin-bore” magnet design. . . . .	25
3.4	LHC Injection Complex . . . . .	26
3.5	Labeled Components of the CMS detector . . . . .	26
3.6	Quadrant of the HCAL showing the layout of the Barrel (HB) , End-Cap (HE) , and Outer (HO) Hadron Calorimeters. Numbers on the top and the left show the segments in $\eta$ , while the numbers on the bottom and right are scintillating layers. . . . .	31
3.7	Layout of the Muon System. The drift tube (DT), resistive plate (RPC), and cathode strip (CSC) chambers are labeled. . . . .	33
3.8	For simulated data, distribution of the maximum HO RecHit energy for hits within $0.2 \Delta R$ of a L1 Muon. A clear MIP bump can be seen at 1 GeV separate from the noise pedestal. For the proposed L1 Muon + MIP trigger the black line represents a threshold energy cut of 0.3 GeV. . . . .	35
3.9	As a function of $p_T$ the efficiency of the L1 Muon + MIP Trigger compared to the current L1 Muon Trigger (left), and the efficiency as a function of $\eta$ (right). The location of the wheel separations are shown by the dotted black lines. . . . .	37

3.10	As a function of $p_T$ , the background reduction of the L1 Muon+MIP trigger compared to the current L 1 Muon trigger (red) and the efficiency (blue). The ratio of background reduction over efficiency is shown on the bottom plot. . . . .	37
4.1	Diagram of how different particles interact with the CMS detector. Charged particles leaves tracks in the Inner Tracker, electrons and photons deposit energy in the ECAL, hadrons deposit energy in the HCAL, and muons leave tracks in the Muon System . . . . .	39
5.1	Example of a proton-proton collision, showing the incoming protons, the hard parton interaction, the outgoing partons. The Initial and Final State radiation is also labeled. . . . .	53
5.2	Next, Next to Leading Order Parton Distribution Functions calculated by NNPDF. The PDF at two different energy scales are shown, $Q = 10$ GeV and $Q = 10$ GeV. NB that the gluon PDF is scaled down by a factor of 10. . . . .	54
5.3	Comparison of the lead photon distribution of events generated with a reweighting method (red) and the standard production method (blue). Figure on the left is for a SM sample and the Figure on the right is for a sample with a dimension-8 effective field theory, LM3, with $f_{M,3} = 500$ TeV <sup>-4</sup> . . . . .	56
5.4	Diagram of the dressing procedure. A generator, such as PYTHIA8 radiates photons off the born lepton. Dressing adds back on the photons that are within a $\Delta R$ cut of 0.1 . . . . .	57
6.1	Separation of the FSR (left) and ISR (right) enriched samples discriminated with $M_{\ell\nu} + M_{\ell\nu\gamma'}$ , where $\gamma'$ is the photon closest to the lepton. Because adding an additional particle never decreases the total mass of the system, the region $M_{\ell\nu\gamma'} < M_{\ell\nu}$ is empty. . . . .	63
6.2	Efficiency of the HLT_IsoMu24 trigger with respect to the off-line reconstructed muons. The selected muon's $p_T$ threshold is 25 GeV, just where the efficiency starts to flatten. . . . .	67
6.3	Shows a comparison of the real and fake photon templates as a function of charge hadron isolation. First bin corresponds to the tight region. On the left is the barrel region of the detector and on the right in the endcap. Figures are made for photons with $p_T$ between 25-40 GeV. . . . .	72
6.4	Lead photon $p_T$ distribution for the electron and muon channel. Shows the data, expected $W\gamma\gamma$ signal, as well as estimates for the jet misidentification, electron misidentification, and other di-photon backgrounds. . . . .	76

6.5	aQGC to SM yields for the LT0 dim-8 theory. Ratios are calculated using reconstructed muon events with a lead photon $p_T > 70$ GeV. The three plots show the three separate $\eta\gamma\eta\gamma$ classifications: (a) Barrel Barrel, (b) Barrel EndCap, and (c) EndCap Barrel. Limit setting power comes mainly from the Barrel Barrel events. Correlations between the samples caused by the reweighting procedure are accounted for when calculating the error bars and the fit. . . . .	82
8.1	Test statistic, $t_f$ (negative log likelihood ratio), value as a function of the $f_{T,0}$ coupling strength. The expected distribution is marked in black and the observed distribution in red. The $1\sigma$ and $2\sigma$ exclusion levels are shown in yellow and green. The 95 % confidence interval corresponds to coupling strength with a $t_f < 3.84$ . . . . .	94
9.1	Examples of $Z\gamma\gamma$ production, through double ISR (a) and through ISR plus FSR (b). Quartic and triple neutral gauge couplings are forbidden in the SM . . . . .	97
10.1	Ratio of the measured to theoretical cross sections for $W\gamma\gamma$ and $Z\gamma\gamma$ . Both cross sections are consistent with the SM prediction, the agreement for the $Z\gamma\gamma$ measurement is particularly strong. The theoretical cross sections are calculated at NLO, the yellow band marks the theoretical uncertainties. . . . .	102

## List of Abbreviations

aQGC	Anomalous Quartic Gauge Coupling
ATLAS	A Toroidal LHC ApparatuS
BSM	Beyond Standard Model
CERN	European Organization for Nuclear Research
CI	Confidence Interval
CL	Confidence Level
CMS	Compact Muon Solenoid
CMSSW	CMS Software
CP	Charge-Parity
CPU	Central Processing Unit
EB	ECAL Barrel
ECAL	Electromagnetic Calorimeter
EE	ECAL Endcap
EFT	Effective Field Theory
EM	Electromagnetic
FSR	Final-State Radiation
HB	HCAL Barrel
HCAL	Hadron Calorimeter
HE	HCAL Endcap
HF	HCAL Forward
HO	HCAL Outer
HPD	Hybrid Photodiode
HLT	High-Level Trigger
ISR	Initial-State Radiation
L1	Level 1
LEP	Large Electron-Positron Collider
LHC	Large Hadron Collider
LHE	Les Houches Event Format
LO	Leading Order
MC	Monte Carlo
MET	Missing Transverse Energy
NLO	Next-to-Leading Order
NNLO	Next-to-Next-to-Leading Order
PF	Particle Flow
PDF	Parton Distribution Function
PMT	Photomultiplier Tube
QED	Quantum Electrodynamics
QCD	Quantum Chromodynamics
QGC	Quartic Gauge Coupling
RBX	Readout Box
RMS	Root Mean Square
RPC	Resistive Plate Chamber

SiPM	Silicon Photomultiplier
SM	Standard Model
SPS	Super Proton Synchrotron
TPG	Trigger Primitive Generator
TTC	Timing, Trigger and Control
UFO	Universal FEYNRULES Output
WLS	Wavelength-Shifting

# Chapter 1

## Introduction

Physics searches for rules describing the motion of matter through space and time. At the beginning of the last century, the incompatibility of classical mechanics with observations of the hydrogen atom motivated the theory of quantum mechanics. Concurrently, weaknesses in classical mechanics' description of objects traveling near the speed of light lead to the development of special relativity. In the 1950's, special relativity and quantum mechanics were combined into a single quantum field theory capable of describing subatomic particles moving at relativistic velocities. The Standard Model (SM) is a quantum field theory describing the interactions of the known subatomic particles. Experimentally, particle accelerators have tested the SM over a wide range of energies, and its predictions have been repeatedly confirmed.

Within the SM, one of the most successful field theories is the Electroweak theory (EWK). Since the 1970's, the EWK sector has been experimentally studied. It is noteworthy that the first evidence came from the observations of a rare process, neutral current, neutrino scattering events detected by the Gargamelle experiment [1]. More recently, precise measurements of electroweak coupling strengths and the vector gauge boson ( $\gamma$ ,  $W$ ,  $Z$ ) masses by the LEP and Tevatron experiments set indirect limits on the mass of the Higgs boson. These precision measurements



placed an upper-bound at 151 GeV [2]. When the Higgs was directly observed in 2012 by the LHC ATLAS and CMS experiments, its mass, consistent with the electroweak limits, was measured at 125 GeV [3][4].

The startup of the LHC marks a new era in high energy physics. In Run 1, 8 TeV center-of-mass energies were achieved in proton-proton collisions, compared to 2 TeV proton-anti-proton collisions at the previous Tevatron accelerator. Dedicated detectors were constructed around the accelerator for the observation of these collisions. This dissertation uses collisions recorded by the Compact Muon Solenoid (CMS) detector. For the 2012 run, CMS recorded an unprecedented number of events corresponding to an integrated luminosity of  $19.4 \text{ fb}^{-1}$ .

Within CMS, a broad analysis program compares data to the SM predictions. For EWK physics, excesses in the production rate of multi-boson processes are a clear sign of new physics. Self-interactions of the the vector gauge bosons occurs through triple and quartic couplings. Triple gauge couplings are well constrained by the previous generation of accelerators, but because of their low cross sections, some of the quartic gauge couplings are just becoming observable at the LHC. Quartic couplings contribute to two classes of physics processes, vector boson scattering and triboson production. This dissertation focuses on the triboson class, and presents one of the first studies of the  $W\gamma\gamma$  and  $Z\gamma\gamma$  three boson final states. For both processes, fiducial cross sections are measured and compared with the predictions of the SM.

Quartic gauge boson couplings are also sensitive to the effects of Beyond the Standard Model (BSM) physics. For the  $W\gamma\gamma$  analysis, limits are set on dimension-

8 Effective Field Theories (EFT) that produce anomalous couplings in the  $WW\gamma\gamma$  vertex [5].

This dissertation is structured as follows. Chapter 2 reviews the SM focusing on the physics of  $W\gamma\gamma$  production and the signatures of anomalous Quartic Gauge Couplings (aQGC). Chapter 3 describes the experimental setup of the LHC accelerator and CMS detector. Chapter 4 covers the algorithms used by CMS for particle reconstruction and identification. Chapter 5 discusses the simulation of particle collisions. Chapter 6 details the  $W\gamma\gamma$  analysis including event selection and background estimates. Chapter 7 deals with the sources of statistical and systematic uncertainties. Chapter 8 interprets the analysis as a fiducial cross-section measurement and limits on dimension-8 EFT. Chapter 9 presents an extension of the analysis to measure the  $Z\gamma\gamma$  fiducial cross section. Finally, Chapter 10 gives the conclusion of the dissertation.

## Chapter 2

### Theory

#### 2.1 Review of the Standard Model

High energy physics is the study of the fundamental constituents of matter. Since the 1970's, the most successful description of these particles has been the Standard Model (SM). The SM plays two roles: firstly, it identifies and classifies the fundamental particles, and secondly it creates a framework for describing how they interact. This framework encompasses three of the four fundamental forces: strong, weak, and electromagnetic. Only the force of gravity is unexplained within the SM. To date, all tests of the SM have affirmed its predictions.

As shown in Figure 2.1, there are four categories of particles: quarks, leptons, gauge bosons, and the Higgs boson. Ordinary matter is composed of quarks and leptons, gauge bosons are the mediators of forces, and the Higgs gives particles their mass. Each particle also has a corresponding anti-particle. Following high energy convention, in this thesis if a distinction is not made between the particle and anti-particle both are being referenced.

##### 2.1.1 Leptons

There are three generations of leptons, each consisting of a charged lepton: electrons ( $e$ ), muons ( $\mu$ ), and taus ( $\tau$ ), as well as a neutral neutrino: ( $\nu_e$ ), ( $\nu_\mu$ ), ( $\nu_\tau$ ).

mass →	≈2.3 MeV/c <sup>2</sup>	≈1.275 GeV/c <sup>2</sup>	≈173.07 GeV/c <sup>2</sup>	0	≈126 GeV/c <sup>2</sup>
charge →	2/3	2/3	2/3	0	0
spin →	1/2	1/2	1/2	1	0
	<b>u</b> up	<b>c</b> charm	<b>t</b> top	<b>g</b> gluon	<b>H</b> Higgs boson
<b>QUARKS</b>					
	≈4.8 MeV/c <sup>2</sup>	≈95 MeV/c <sup>2</sup>	≈4.18 GeV/c <sup>2</sup>	0	
	-1/3	-1/3	-1/3	0	
	1/2	1/2	1/2	1	
	<b>d</b> down	<b>s</b> strange	<b>b</b> bottom	<b>γ</b> photon	
<b>LEPTONS</b>					
	0.511 MeV/c <sup>2</sup>	105.7 MeV/c <sup>2</sup>	1.777 GeV/c <sup>2</sup>	91.2 GeV/c <sup>2</sup>	
	-1	-1	-1	0	
	1/2	1/2	1/2	1	
	<b>e</b> electron	<b>μ</b> muon	<b>τ</b> tau	<b>Z</b> Z boson	
	<2.2 eV/c <sup>2</sup>	<0.17 MeV/c <sup>2</sup>	<15.5 MeV/c <sup>2</sup>	80.4 GeV/c <sup>2</sup>	
	0	0	0	±1	
	1/2	1/2	1/2	1	
	<b>ν<sub>e</sub></b> electron neutrino	<b>ν<sub>μ</sub></b> muon neutrino	<b>ν<sub>τ</sub></b> tau neutrino	<b>W</b> W boson	
					<b>GAUGE BOSONS</b>

**Figure 2.1:** Table of the Elementary Particles. The particles are arranged by type, the leptons, the quarks, the gauge bosons, and the recently discovered scalar Higgs Boson.

Both types of leptons interact via the weak force; charged leptons also carry unit charge and can interact electromagnetically. In these interactions, lepton number, for each generation, is conserved:  $L_\ell = n_\ell - n_{\bar{\ell}}$ . In the canonical example, when a muon decays to an electron, it also produces a muon neutrino and an anti-electron neutrino:  $\mu^- \rightarrow e^- + \nu_\mu + \bar{\nu}_e$ . In this way, the net muon lepton number ( $L_\mu$ ) remains one, and the net electron lepton number ( $L_e$ ) stays at zero.

### 2.1.2 Quarks

Like leptons, there are also six flavours of quarks, divided between three generation. For each generation there is an up-type quark of charge  $\frac{2}{3}$  and a down type quark of charge  $-\frac{1}{3}$ . The up-type quarks are the up (u), charm (c), and top (t), and the down-type quarks are the down (d), strange (s), and bottom (b). Quarks

interact via the strong, the electromagnetic, and the weak forces.

Lone quarks are not stable, and in nature quarks are found in bound, composite states called hadrons. There are two type of hadrons: baryons which are composed of three quarks (or three antiquarks) and mesons which are composed of a quark and an anti-quark. Protons (p) and neutrons (n) are examples of baryons, while pions ( $\pi^0$ ,  $\pi^\pm$ ) are examples of mesons. Recently, the LHCb Collaboration discovered a hadron composed of four quarks and an anti-quark, called pentaquarks [6].

In quark interactions, baryon number,  $B = \frac{1}{3}(n_q - n_{\bar{q}})$  is conserved. Note that, unlike for leptons, no distinction is made between quark generations. Because of baryon conservation, the proton, which is the lightest baryon, must be stable. Mesons, however are free to decay to a non-quark final states, ie  $\pi^- \rightarrow \mu\bar{\nu}_\mu$ .

### 2.1.3 Gauge Bosons

Gauge bosons are interpreted as the mediators of forces. The electromagnetic force is carried by the photon. The weak force, responsible for  $\beta$ -decay, is carried by the  $W$  and  $Z$ . The strong force, responsible for holding nucleii together, is carried by the gluon.

Both the photon and the gluon are massless and electrically neutral. The  $W$  boson has unit charge and a mass of about 80 GeV, the  $Z$  boson is neutral and has a mass of about 91 GeV.

## 2.1.4 Quantum Field Theory

The framework of the Standard Model is built on relativistic quantum field theory (QFT). QFT uses the Lagrangian formalism to determine the equation of motion of fields. The fields are quantized and their excitations are interpreted as physical particles.

In principle, from the SM Lagrangian the dynamics of the fields can be derived. In practice, though, analytic solutions are rarely possible. However, if the coupling strengths on Lagrangian operators is small, one can use perturbation theory. The lowest order calculation in perturbation theory is called the leading order (LO) calculation, incorporating the next term is the next-to-leading NLO calculation, and so on. In making these calculations, theorists and experimentalists frequently make use of Feynman diagrams. These are visual representations of the interactions with prescribed rules for calculating cross sections and branching ratios.

Since QFT is a relativistic theory, particles obey the kinematics of special relativity. Being a quantum theory, particles are distinguished by their quantum numbers. For example, particles have a quantum number called spin, related to angular momentum. Particles with half integer spin, such as quarks and leptons, are called fermions. These particles obey Fermi-Dirac statistics and the Pauli exclusion principle. Particles with integer spin, such as the gauge bosons and the Higgs, are called bosons. These particles obey Bose-Einstein statistics.

The framework of QFT also requires the existence of anti-particles, and defines them to have the same mass and as their partner, but opposite charge values.

Noether's theorem states that the symmetries of a Lagrangian correspond to conserved charges. The SM has an  $SU(3)_C \times SU(2)_L \times U(1)_Y$  symmetry, leading to conservation of color, left-handed chirality, and weak hypercharge. These charges are also quantum numbers.

In the SM, symmetries are also conserved under local transformations, so called gauge transformations. Gauge transforms introduce gauge fields which correspond to the SM gauge bosons. These gauge transforms also produce interaction terms between the gauge boson fields and the fermion fields. It is for this reason that the gauge bosons can be seen as mediators of the fundamental forces. The interaction terms also sets the strength with which particles will couple to each other.

In the following sections, the physical impact of the conserved charges and the gauge transforms is explored in more detail.

#### 2.1.4.1 Quantum Chromodynamics $SU(3)_C$

The  $SU(3)_C$  symmetry corresponds to the conservation of color. Drawing from the primary colors, particles are said to carry red, green, or blue color. Color-neutral "white" states contain all three of the primary colors or a color and its anti-color. In the SM, quarks each carry a single color. This is why three quark baryons and two quark mesons are stable. Further, conservation of color explains why baryon number is conserved, while meson number is not.

Gauging the  $SU(3)_C$  symmetry introduces 8 massless bosons, the gluons. Each gluon carries a color and anti-color charge. The interaction terms between the quarks

and the gluons are the realization of the strong force. Since the gluons are massless, the strong field has infinite range. However, in analogy with a spring being pulled, as two quarks are separated, the energy in the field increases. As the energy in the field grows, quark-antiquark pairs and gluons are produced from the vacuum. This process continues until the quarks have combined to form color neutral particles, hadrons. This is the process of hadronization. The tight cone of particles created by hadronization is known as a jet. A single quark or gluon from a high energy collision hadronizes many lower energy stable particles. For example in a 500 GeV jet, the average stable constituent particle carries a momenta of only 10 GeV [7].

A related concept is color confinement. Since particles carrying color hadronize until neutral states are formed, quarks are never observed in isolation. There is an exception, though. Quarks are asymptotically free, meaning at high energies the interaction strength between quarks decrease. High energy quarks can be considered unconfined, and more importantly, asymptotic freedom allows perturbative calculations to be made.

#### 2.1.4.2 Electroweak Theory $SU(2)_L \times U(1)_Y$

The  $SU(2)_L \times U(1)_Y$  symmetry gives conservation of weak isospin ( $T_3$ ) and weak hypercharge ( $Y$ ). All the fermions carry weak hypercharge, however only quarks and leptons with left-handed parity carry weak isospin. Isospin and hypercharge are related to the electric charge of a particle by the equation  $Q = T_3 + \frac{Y}{2}$ .

The fermions are grouped into multiplets depending on their chirality. Left



	Generation			Electroweak Charges		
	1 <sup>st</sup>	2 <sup>nd</sup>	3 <sup>rd</sup>	$T_3$	$Y$	$Q$
Quarks	$\begin{pmatrix} u \\ d' \end{pmatrix}_L$	$\begin{pmatrix} c \\ s' \end{pmatrix}_L$	$\begin{pmatrix} t \\ b' \end{pmatrix}_L$	$\begin{pmatrix} +\frac{1}{2} \\ -\frac{1}{2} \end{pmatrix}$	$\begin{pmatrix} +\frac{1}{3} \\ -\frac{1}{3} \end{pmatrix}$	$\begin{pmatrix} +\frac{2}{3} \\ -\frac{1}{3} \end{pmatrix}$
	$u_R$	$c_R$	$t_R$	—	$+\frac{4}{3}$	$+\frac{2}{3}$
	$d_R$	$s_R$	$b_R$	—	$-\frac{2}{3}$	$-\frac{1}{3}$
Leptons	$\begin{pmatrix} \nu_e \\ e \end{pmatrix}_L$	$\begin{pmatrix} \nu_\mu \\ \mu \end{pmatrix}_L$	$\begin{pmatrix} \nu_\tau \\ \tau \end{pmatrix}_L$	$\begin{pmatrix} +\frac{1}{2} \\ -\frac{1}{2} \end{pmatrix}$	$\begin{pmatrix} -1 \\ -1 \end{pmatrix}$	$\begin{pmatrix} 0 \\ -1 \end{pmatrix}$
	$e_R$	$\mu_R$	$\tau_R$	—	-2	-1

**Table 2.1:** Values of the weak isospin, the weak hypercharge, and the electric charge for the quarks and leptons. Quarks and leptons are broken up between the left-handed doublets and the right-handed singlets.

handed leptons and quarks are grouped into doublets, while the right handed quarks and charged leptons are grouped into singlets. In the SM, right-handed neutrinos do not exist. Table 2.1 illustrates the multiplet groupings and the values of  $T_3$ ,  $Y$ , and  $Q$  for the quarks and leptons.

The electroweak theory, has four gauge bosons, the  $\gamma$ ,  $W^\pm$ , and  $Z$ . The physics of the electroweak gauge bosons is the primary focus of this thesis, and a full discussion is reserved until discussion the nature of  $W\gamma\gamma$  production in Section 2.3.

Photons interact with the electrically charged particles, and  $Z$  bosons interacts with all fermions.  $W^\pm$  bosons, though, only interact with the left handed doublets. For leptons, the doublets are charged leptons grouped with neutrinos of the same generation. The  $W$  boson does not introduce any mixing between the lepton generations, and this is why Lepton number is conserved by generation. On the other hand, the quark doublets are groupings of up-type quarks with superpositions of the down-type quarks ( $d'$ ,  $s'$ ,  $b'$ ). This superposition means it is possible for quarks of different generations to mix, and why baryon number is not conserved by generation.

The strength of the mixing is given by the Cabibbo matrix. The diagonal values of the Cabibbo matrix are very close to 1, meaning there is still a strong preference for quarks to interact within the same generation.

### 2.1.5 Symmetry Breaking and the Higgs Boson

In the simplest version of electroweak theory, the gauge bosons should be massless, just like the gluons in quantum chromodynamics. However, both the  $W^\pm$  and  $Z$  have experimentally measured masses. These masses are explained by introducing a spontaneously broken symmetry into the electroweak theory [8]. The Higgs mechanism provides this symmetry breaking by introducing a non-zero vacuum expectation value (VEV) for the Higgs field ( $\phi$ ). Figure 2.2 shows the unstable equilibrium as a function of  $\phi$ . Confirmation of the Higgs mechanism was discovered in 2012, when both ATLAS and CMS observed a Higgs boson at a mass of 125. Through a separate mechanism, the Higgs field also imparts mass to the fermions. The fermion fields ( $\psi$ ) couple to the Higgs field ( $\phi$ ) through a Yukawa coupling:  $G_f \bar{\psi} \phi \psi$ .

### 2.1.6 Beyond the Standard Model

Despite the Standard Model's great successes, there are observed phenomena it cannot explain. In recent years, two beyond-the-Standard-Model (BSM) results have been the focus of much research. First, observations of neutrino oscillations require neutrinos to have a non-zero mass. Second, astronomical observations of the

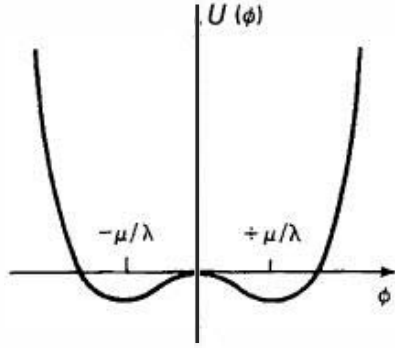


**Figure 2.2:** Diagram of the ground states of the Higgs field. From Griffiths [9]

Cosmic Microwave Background (CMB), the rotation curves of galaxies, gravitational lensing of galaxy clusters, and simulation of the growth of structure are all consistent with the result that most matter in the universe is made up of “dark” particles that attracts gravitationally but do not interact electromagnetically.

## 2.2 Vector Gauge Couplings

As described in Section 2.1.4.2, Electroweak Theory comes from an  $SU(2)_L \times U(1)_Y$  symmetry and leads to four gauge bosons. The Lagrangian describing the free fields of these gauge bosons is:

$$\mathcal{L} = -\frac{1}{4}W_{\mu\nu}^{a\dagger}W_a^{\mu\nu} - \frac{1}{4}B_{\mu\nu}B^{\mu\nu}, \quad a = 1-3,$$

where :

$$W_{\mu\nu}^a = \partial_\mu W_\nu^a - \partial_\nu W_\mu^a - gf_{abc}W_\mu^b W_\nu^c,$$

$$B_{\mu\nu} = \partial_\mu B_\nu - \partial_\nu B_\mu.$$

(2.1)

The  $W_{\mu\nu}^a$  operators are non-abelian, meaning they do not commute with each other. This is manifested in the final term,  $gf_{abc}W_\mu^bW_\nu^c$ , which is responsible for triple and quartic gauge couplings. It is common to rewrite the  $W$ 's in terms of the charge eigenstates, where  $W_\mu^\pm = \frac{1}{\sqrt{2}}(W_\mu^1 \pm iW_\mu^2)$  and the neutral  $W_\mu^3$ . The structure constant  $f_{abc}$  is antisymmetric and is only non-zero for indices corresponding to two charged  $W$ 's and a neutral  $W^3$ . As a result, triple or quartic couplings of only neutral gauge bosons are forbidden in the Standard Model.

In Section 2.1.5, we noted that the weak force bosons are given masses by the Higgs symmetry breaking mechanism. This has the effect that the neutral  $W_\mu^3$  and  $B_\mu$  fields become linear combinations of the physical  $Z$  boson and  $\gamma$  ( $A_\mu$ ). The Weinberg angle,  $\theta_w$ , is the amount by which the  $W_\mu^3$  and  $B_\mu$  are rotated into  $Z_\mu$  and  $A_\mu$ .

$$\begin{aligned} W_\mu^3 &= \cos\theta_w Z_\mu + \sin\theta_w A_\mu \\ B_\mu &= -\sin\theta_w Z_\mu + \cos\theta_w A_\mu \end{aligned} \tag{2.2}$$

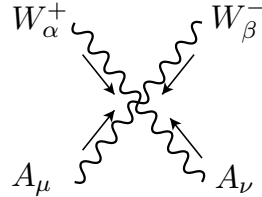
Experimentally  $\theta_w$  is measured as  $\sin^2\theta_w = 0.23$ . Since  $\theta_w$  is small, this means the  $W_\mu^3$  tends to be more  $Z$ -like, and the  $B_\mu$  more  $\gamma$ -like.

Taking the quartic terms of the SM Lagrangian and rewriting them in terms

of the physical fields of the physical particles, one gets:

$$\begin{aligned}
\mathcal{L}_{\text{QGC}} = & e^2 [A^\mu A^\nu W_\mu^- W_\nu^+ - A^\mu A_\nu W^{-\nu} W_\nu^+] \\
& + eg \cos \theta_w [A^\mu Z^\nu (W_\mu^- W_\nu^+ + W_\mu^+ W_\nu^-) - 2A^\mu Z_\mu W^{-\nu} W_\nu^+] \\
& + g^2 \cos^2 \theta_w [Z^\mu Z^\nu W_\mu^- W_\nu^+ - Z^\mu Z_\nu W^{-\nu} W_\nu^+] \\
& + g^2 [W^{-\mu} W^{+\nu} W_\mu^- W_\nu^+ - (W^{-\mu} W_\mu^+)^2]
\end{aligned} \tag{2.3}$$

The strength of quartic couplings are prescribed by physical constants and the structure of electroweak theory. As a result, measurements of these processes are a direct test of the SM. An example of a SM quartic vertex and its Feynman rule are shown below:



Feynman Rule for  $WWAA$  Vertex:

$$- ie^2 [2g_{\alpha\beta} g_{\mu\nu} - g_{\alpha\nu} g_{\beta\mu} - g_{\alpha\nu} g_{\beta\mu}] \tag{2.4}$$

### 2.3 $W\gamma\gamma$ Production

This thesis focuses on a rare Standard Model process,  $W\gamma\gamma$  production. We study this process in  $pp$  collisions where the  $W$  decays leptonically,  $pp \rightarrow \ell\bar{\nu}\gamma\gamma$ . This is a vector gauge coupling process and in particular, a quartic gauge coupling process (See Fig. 2.3). In the  $pp$  collision, a quark and a different flavor, anti-quark couple to a virtual  $W$ , that decays via a quartic vertex to a  $W$  and two photons.

Multiple Feynman diagrams, though, contribute to the  $pp \rightarrow \ell\bar{\nu}\gamma\gamma$  matrix

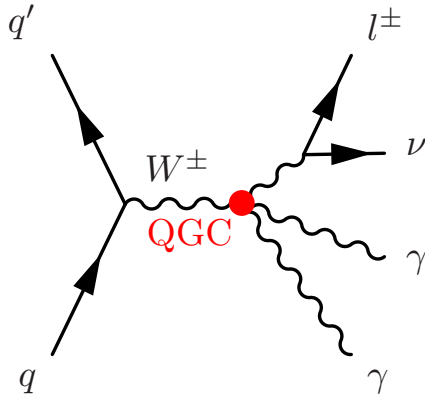


**Figure 2.3:** Feynman Diagram of Quartic Gauge Coupling in the  $W\gamma\gamma$  process. All three bosons come from the same vertex, the coupling strength of which is prescribed by the structure of Electroweak theory and the values of physical constants.

element. In addition to gauge couplings, photons are also produced through initial state radiation (ISR) off the incoming quarks or final state radiation (FSR) off the outgoing lepton. There are diagrams from triple gauge couplings plus an ISR or FSR photon and diagrams with two ISR photons, two FSR photons, or an ISR and an FSR photon. Examples of these Feynman diagrams are shown in Figure 2.4.

## 2.4 Anomalous Gauge Couplings

Quartic couplings are a test of the SM. If the coupling strengths deviate from their predicted values, this is strong evidence of new physics. In the following sections, we outline some theoretical models for how beyond the SM physics could affect the quartic vertices.

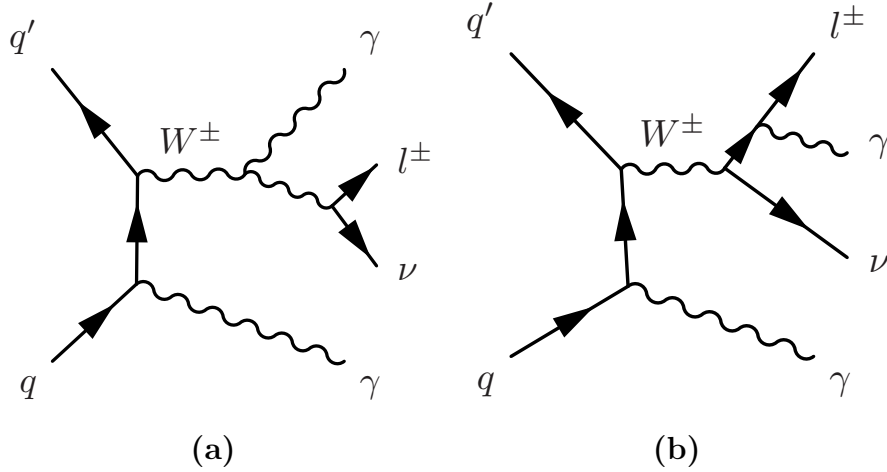


**Figure 2.4:** Feynman Diagram on the left shows  $W\gamma\gamma$  production where the photons are from triple gauge coupling (TGC) + ISR. Diagram on the right shows an example of photons radiated through ISR + FSR.

### 2.4.1 Effective Field Theories

Effective field theories (EFT) are designed to take into account the strongest aspects of the Standard Model: that there should be Lorentz invariance, a  $SU(3)_C \times SU(2)_L \times U(1)_Y$  gauge symmetry, and that the Standard Model should be recovered over already searched energies [10].

In any formalism, the Lagrangian density,  $\mathcal{L}$ , has mass dimension four. Operators are the components of the Lagrangian that are strictly the product of fields. In the SM, the operators have mass dimension four or less. Effective field theories introduce new operators of higher mass dimensions. Since the Lagrangian is still of dimension four, these new operators must be preceded by coefficients with dimensions of inverse powers of mass. When the energy of the interaction is small compared to the scale of this mass term,  $\Lambda$ , its contribution can be neglected. For this reason,  $\Lambda$  is also known as the energy scale of new physics. Since  $\frac{1}{\Lambda}$  should be

less than one, the impact of all but the lowest-order higher dimension terms can be ignored.

Dimension-6 effective field theories can produce QGCs, but they also produce TGCs. Strong limits on the dimension-6 EFTs are already set by experimental measurements of TGCs in the diboson final states. This analysis focuses on effective field theories that produce "purely" quartic gauge couplings, meaning QGCs without TGCs. The lowest order purely quartic gauge coupling model is of dimension-8. Using the EFT formalism, the aQGC Lagrangian can be written as,

$$\mathcal{L}_{\text{aQGC}} = \mathcal{L}_{\text{SM}} + \sum_i \frac{f_i}{\Lambda^4} \mathcal{O}_i + \dots \quad (2.5)$$

So that the  $SU(2)_L \times U(1)_Y$  symmetry, is respected, the EFT operators are built from fields in which this property is inherent. Following the naming conventions chosen by Eboli et al., we introduce:

$$\begin{aligned} \mathcal{D}_\mu &= \partial_\mu + \frac{i}{2} g \tau^I W_\mu^I + \frac{i}{2} g' B_\mu, \\ \hat{W}_{\mu\nu}^a &= \sum_j W_{\mu\nu}^j \frac{\sigma^j}{2}, \end{aligned} \quad (2.6)$$

$\mathcal{D}_\mu$  is the covariant derivative, and we will define  $\Phi$  as the Higgs doublet field. The dimension-8 effective field theories that effect the  $W\gamma\gamma$  process are listed below[5]. Following equation 2.5, each of these operators appear in the EFT Lagrangian weighted by a factor of  $\frac{1}{\Lambda^4}$  and an undetermined coefficient,  $f_i$ .



$$\begin{aligned}
\mathcal{L}_{M,0} &= Tr[\hat{W}_{\mu\nu}\hat{W}^{\mu\nu}] \times [(D_\beta\Phi)^\dagger D^\beta\Phi] \\
\mathcal{L}_{M,1} &= Tr[\hat{W}_{\mu\nu}\hat{W}^{\nu\beta}] \times [(D_\beta\Phi)^\dagger D^\mu\Phi] \\
\mathcal{L}_{M,2} &= [B_{\mu\nu}B^{\mu\nu}] \times [(D_\beta\Phi)^\dagger D^\beta\Phi] \\
\mathcal{L}_{M,3} &= [B_{\mu\nu}B^{\nu\beta}] \times [(D_\beta\Phi)^\dagger D^\mu\Phi]
\end{aligned}
\tag{2.7}$$

$$\begin{aligned}
\mathcal{L}_{T,0} &= Tr[\hat{W}_{\mu\nu}\hat{W}^{\mu\nu}] \times Tr[\hat{W}_{\alpha\beta}\hat{W}^{\alpha\beta}] \\
\mathcal{L}_{T,1} &= Tr[\hat{W}_{\alpha\nu}\hat{W}^{\mu\beta}] \times Tr[\hat{W}_{\mu\beta}\hat{W}^{\alpha\nu}] \\
\mathcal{L}_{T,2} &= Tr[\hat{W}_{\alpha\mu}\hat{W}^{\mu\beta}] \times Tr[\hat{W}_{\beta\nu}\hat{W}^{\nu\alpha}] \\
\mathcal{L}_{T,5} &= Tr[\hat{W}_{\mu\nu}\hat{W}^{\mu\nu}] \times B_{\alpha\beta}B^{\alpha\beta} \\
\mathcal{L}_{T,6} &= Tr[\hat{W}_{\alpha\nu}\hat{W}^{\mu\beta}] \times B_{\mu\beta}B^{\alpha\nu} \\
\mathcal{L}_{T,7} &= Tr[\hat{W}_{\alpha\mu}\hat{W}^{\mu\beta}] \times B_{\beta\nu}B^{\nu\alpha}
\end{aligned}
\tag{2.8}$$

Studying the  $W\gamma\gamma$  channel, one is only sensitive to the terms that effect the  $WWAA$  vertex. Because  $\gamma$  is a linear combination of the  $B_\mu$  and  $W_\mu^3$ , these effects are not always unique. The  $\mathcal{L}_{M,0}$  and  $\mathcal{L}_{M,2}$  have the same operators for the  $WWAA$  term, except the former has a factor of  $\frac{1}{2}\sin^2\theta_w$  and the later a factor of  $\cos^2\theta_w$ .

This means  $\mathcal{L}_{M,0}$  behaves equivalently to  $\mathcal{L}_{M,2}$  with a coupling strength 6.7 times stronger. A comparison of the  $\mathcal{L}_{M,0}$ ,  $\mathcal{L}_{M,2}$ , and the SM are show in Figure 2.5.

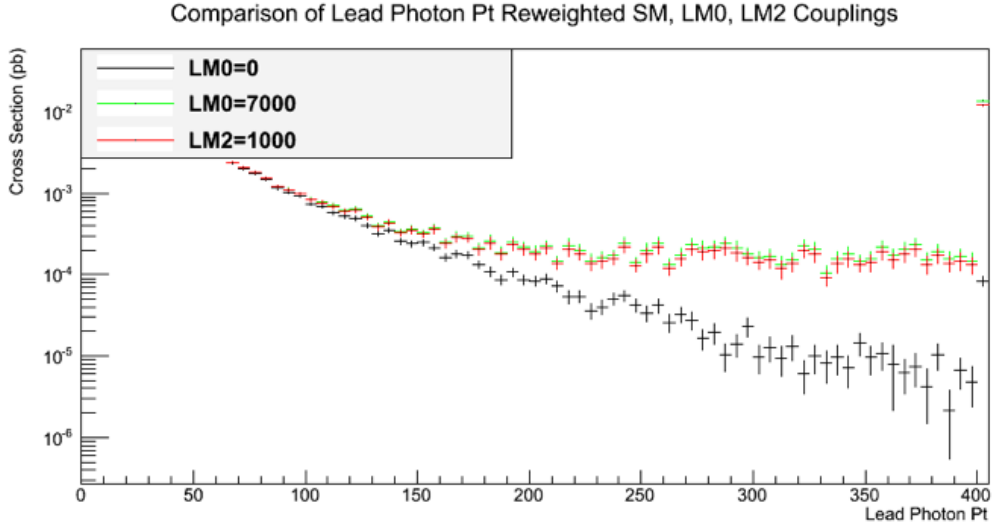
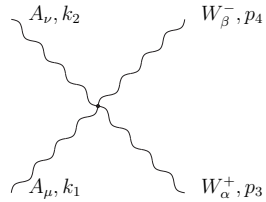


**Figure 2.5:** Cross section of the  $\mathcal{L}_{M,0}$ ,  $\mathcal{L}_{M,2}$ , and SM theories as a function of lead photon  $p_T$ . The  $\mathcal{L}_{M,0}$  and  $\mathcal{L}_{M,2}$  operators contribute in the same underlying way to the WWAA vertex, only with coefficients differing by a factor of  $2 \frac{\cos^2 \theta_w}{\sin^2 \theta_w} \sim 7$

The  $W\gamma\gamma$  channel is found to be particularly sensitive to the  $\mathcal{L}_{T,0}$  theory.

Shown below is an example of an EFT WWAA vertex and its Feynman rule:



Feynman Rule for  $\mathcal{L}_{T,0}$ , WWAA Vertex:

$$\frac{f_{T,0} \sin^2 \theta_w}{\Lambda^4} \frac{\sin^2 \theta_w}{4} \cdot [(k_1 \cdot k_2) g_{\mu\nu} - k_{1\mu} k_{2\nu}] [(p_3 \cdot p_4) g_{\alpha\beta} - p_{3\alpha} p_{4\beta}] \quad (2.9)$$

## 2.4.2 Anomalous Couplings

Effective Field Theories are not the only framework for studying new physics in the vector gauge couplings.

Earlier work, especially for TGCs, used an anomalous coupling approach [11].

Instead of being built around the composite  $W$  and  $B$  fields, the anomalous gauge

couplings are built around the interactions of the physical  $W$ ,  $Z$ , and  $\gamma$ . This has the advantage that the couplings can be easily related to experimental measurements. However, it comes at the theoretical cost that the  $SU(2)\times U(1)$  symmetry is no longer guaranteed.

### 2.4.3 Unitarity

In quantum mechanics, outcome probabilities must sum to 1. For scattering experiments, this is encompassed by a unitarity requirement on the matrix relating the initial quantum state to the final state (S-matrix). Through the generalized optical theorem, the unitarity condition is often reinterpreted as maximum bound on the cross section [12]. (See Appendix A.1 for details on Unitarity and the Optical Theorem).

For EFTs and anomalous couplings, cross sections can grow rapidly with energy eventually violating the unitarity bound. To address this fault in the theory, an additional form factor is sometimes added to the coupling constant. Depending on the energy at which unitarity is violated, the form factors have an energy scale parameter,  $\Lambda_{FF}$ , which damps out the anomalous couplings. The form factor acting on a coupling is defined as:

$$\Delta\kappa(s) = \frac{\Delta(\kappa)}{(1 + s/\Lambda_{FF}^2)^n}, \quad (2.10)$$

where  $n$  must be at least 2 for a dim-8 EFT.

For EFTs, the violation of unitarity is not alarming. The theory is only ex-

pected to be valid when  $\frac{s}{\Lambda^2}$  is small and contributions from higher-dimension operators can be ignored. Violations of unitarity occur at energies where  $\frac{s}{\Lambda^2}$  is greater than unity and the EFT approximation breaks down [10].

## Chapter 3

### Experiment

#### 3.1 The Large Hadron Collider

The Large Hadron Collider (LHC) is the largest, highest energy, particle accelerator in the world. Located along the French-Swiss border near Geneva, the LHC spans 26.7 km in circumference and is buried approximately 100 meters underground. The four main detectors (CMS, ATLAS, LHCb, and ALICE) are located at collision points around the LHC ring. Figure 3.1 shows the layout of the LHC and the position of the four detectors.

The LHC is a proton-proton collider designed to accelerate two beams of counter-rotating protons. At detector locations, the beams are crossed allowing protons to collide with design center-of-mass energies of 14 TeV. These collisions produce physical processes,  $pp \rightarrow X$ , where the rate of the processes ( $R$ ) is equal to the accelerator luminosity ( $L$ ) times the interaction cross section ( $\sigma$ ).

$$R(pp \rightarrow X) = L \cdot \sigma(pp \rightarrow X) \quad (3.1)$$

The luminosity depends on parameters of the accelerator, whereas the cross section depends on the underlying physics.

At the LHC, protons in the two beams are separated into bunches using radio

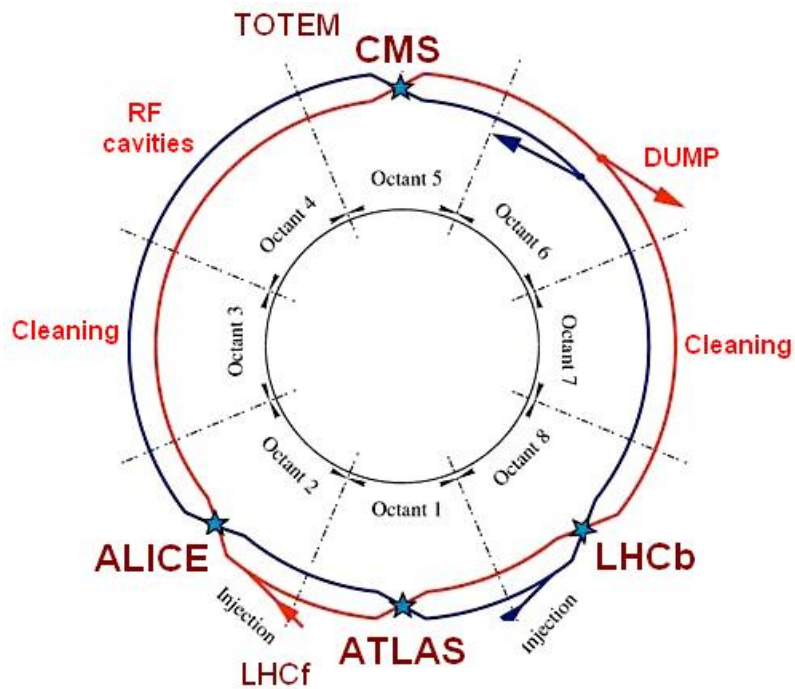


**Figure 3.1:** Layout of the LHC. The path of the two beams are shown in red and blue, and the location of the four main detectors at the beam crossings are indicated by stars.

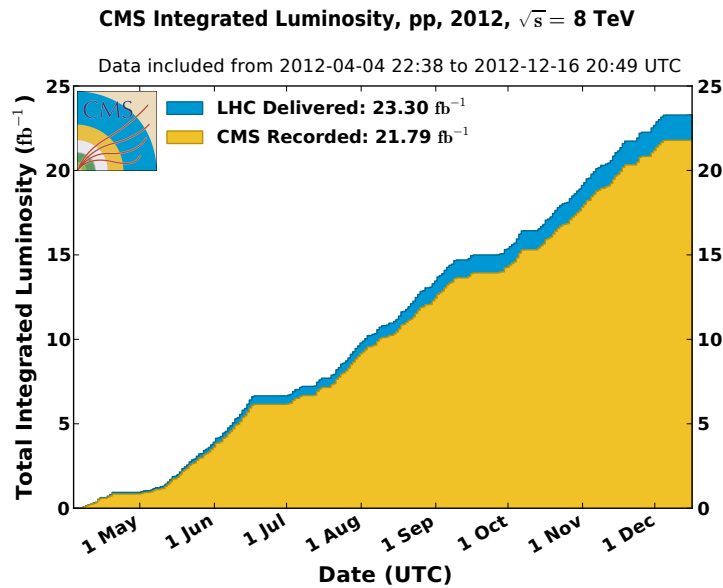


**Figure 3.2:** Cumulative integrated luminosity for the CMS detector over the 2012 run at a center-of-mass energy of 8 TeV.

frequency (RF) cavities. The LHC is designed for bunch spacings of approximately 25 ns corresponding to a frequency ( $f$ ) of 40.08 MHz. For each beam, a bunch contains approximately  $10^{11}$  protons ( $N_p$ ). Luminosity is defined as:

$$L = \frac{f \cdot N_p^2}{4\pi \sqrt{\sigma_x^2 \sigma_y^2}} \quad (3.2)$$

where  $\sigma_{x(y)}$  are the transverse profiles of the beams described by a gaussian density profile. The design luminosity of the LHC is  $10^{34} \text{ cm}^{-2}\text{s}^{-1}$ .

The total number of events observed over a period of time is proportional to the integrated luminosity  $\mathcal{L} = \int L(t)dt$ . Figure 3.2 shows the integrated luminosity collected by the CMS detector over the 2012 run. For the 2012 collected data, the LHC operated at beam energies of 4 TeV and bunch spacings of 50 ns. The detector received  $23.3 \text{ fb}^{-1}$  of integrated luminosity,  $21.8 \text{ fb}^{-1}$  of which were recorded, and  $19.4 \text{ fb}^{-1}$  of which were used in the  $W\gamma\gamma$  analysis.

To keep relativistic velocity, protons traveling inside the ring, powerful superconducting magnets bend the protons' trajectories. It is the strength of the magnetic field that limits the energy of collisions. LHC magnets are cooled with liquid helium and operate at 2 K. They produce magnetic fields of 8.3 Tesla, allowing proton energies of up to 7 TeV [13].

Since the two beams are moving in opposite directions, bending them requires oppositely directed magnetic dipole fields. To minimize the cost of cooling magnets and to save space, both beams are housed in the same cryostat and the LHC uses a "twin-bore" magnet design. Figure 3.3 shows the cross section of an LHC

## LHC DIPOLE : STANDARD CROSS-SECTION

CERN AC/OL/MM - HE107 - 30 04 1999

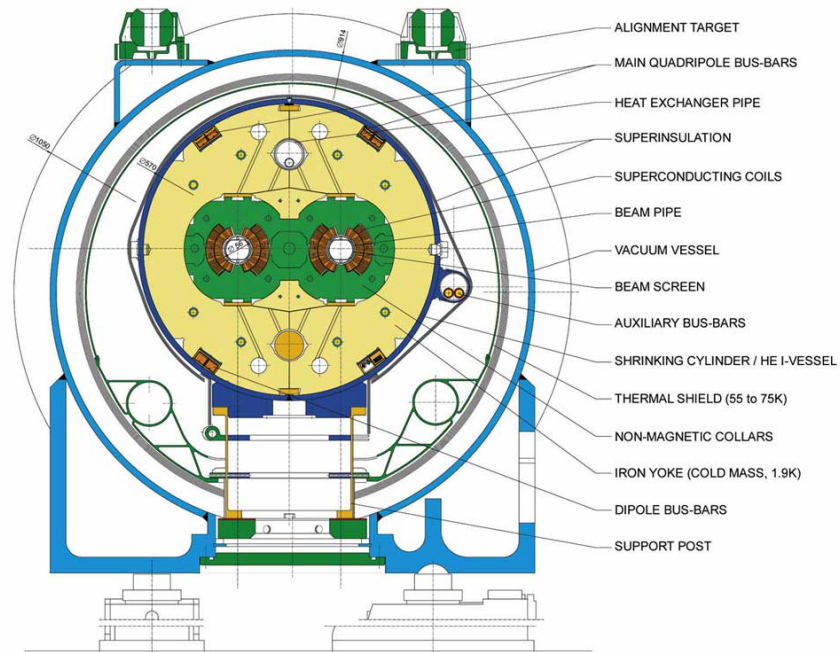


**Figure 3.3:** Cross section of an LHC cryodipole magnet showing the two beam pipes and the “twin-bore” magnet design.

cryodipole magnet. The coils for the superconducting magnet are constructed from NbTi Rutherford cables. There are 1,232 such magnets along the LHC ring [13].

Acceleration of protons at the LHC is carried out in multiple stages. First, the protons are generated from a pulsed ion source called a Duoplasmatron. They are accelerated through a linear accelerator, LINAC 2, to energies of 50 MeV. Next, the protons are injected into a series of increasingly large synchrotrons: the Proton Synchrotron Booster, the Proton Synchrotron (PS), and finally the Super Proton Synchrotron (SPS) in each stage reaching energies of 1.4, 26, and finally 450 GeV. At 450 GeV, the protons are injected into the main LHC ring and accelerated to their maximum energy [13]. Figure 3.4 shows an illustration of the LHC injection complex and the stages of acceleration.



## The LHC injection complex

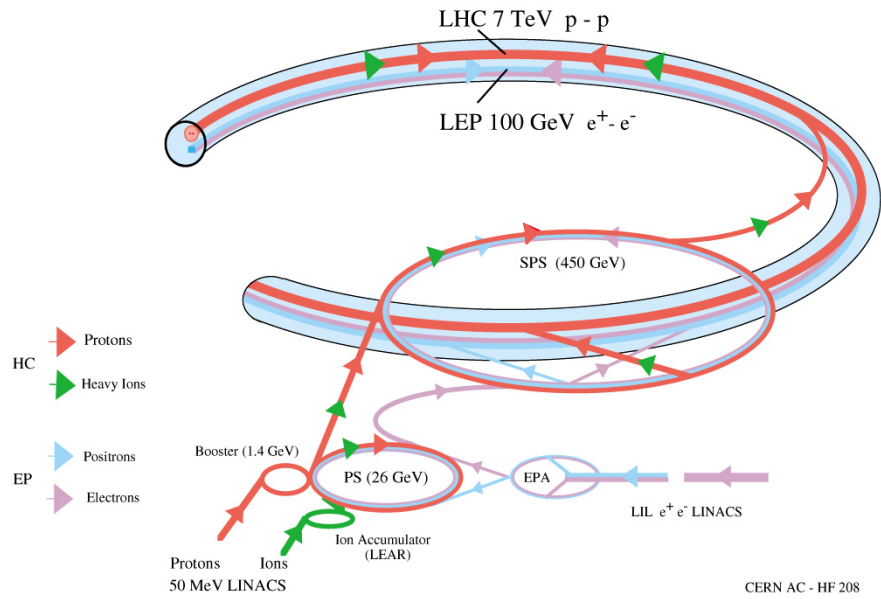


Figure 3.4: LHC Injection Complex

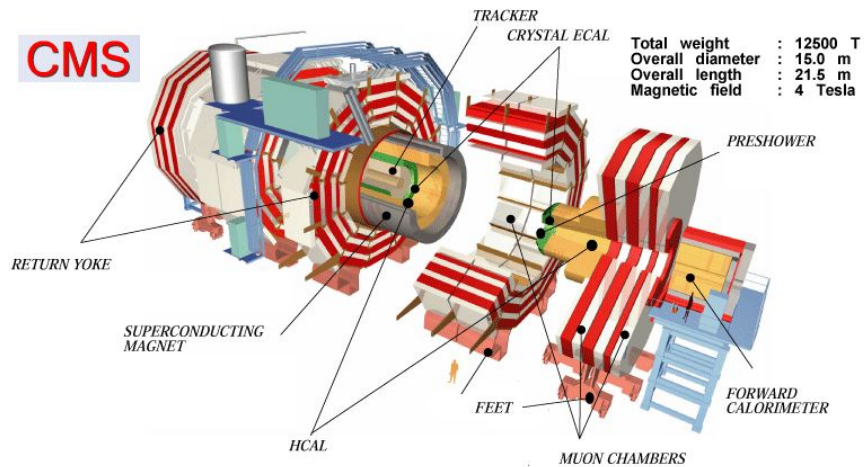


Figure 3.5: Labeled Components of the CMS detector

## 3.2 The Compact Muon Solenoid Detector

CMS is one of two general search detectors at the LHC, the other being ATLAS, A Toroidal LHC ApparatuS. This section describes the main components of the CMS detector. The detector is centered around the beam pipe, where the proton-proton beams cross and high energy collisions occur. Working outwards is the inner tracker, then the electromagnetic calorimeter (ECAL), the hadronic calorimeter (HCAL), the superconducting solenoid, and finally the Muon System. Each of the sub-detectors plays a unique role in identifying particles and measuring their kinematics information. Figure 3.5 shows a labeled diagram of the CMS experiment.

### 3.2.1 Position Notation

The CMS detector is shaped like a 22 meter long and 15 meter high cylinder. It has a long barrel section and two endcaps on either end. The detector can be described in terms of cartesian coordinates, with the origin at the center of the detector, the interaction point, and the z-axis along the LHC beam pipe. The x-y plane is transverse to the beam pipe with the x-axis directed towards the center of the LHC ring and the y-axis directed vertically up.

Because the detector enwraps the beam pipe, the transverse plane is often described by the azimuthal angle,  $\phi$ , and radius,  $r$ . CMS has near full  $2\pi$  coverage in  $\phi$ , important for energy balance measurements in the transverse direction [14].

Similarly, instead of the z coordinate, one can use the polar angle  $\theta$ . High

energy physicists prefer to use a related variable, pseudorapidity ( $\eta$ ),

$$\eta = -\ln \left[ \tan\left(\frac{\theta}{2}\right) \right] = \frac{1}{2} \ln \left[ \frac{p + p_L}{p - p_L} \right], \quad (3.3)$$

where  $p_L$  is the longitudinal momentum along the beam axis. An  $\eta$  of zero corresponds to motion perpendicular to the beam axis while an  $\eta$  of infinity corresponds to parallel motion. Pseudorapidity has the advantage that is easily described in terms of Lorentz boosts in the longitudinal direction, and particle distribution is expected to be approximately uniform in  $\eta$ . See Appendix A.2 for more details on pseudorapidity.

For CMS, the inner tracker covers a region of  $|\eta| < 2.5$ , the electromagnetic and hadronic calorimeter cover  $|\eta| < 3.0$ , an additional forward hadronic calorimeter extends the coverage to  $|\eta| < 5$ , and the muon system covers a range of  $|\eta| < 2.4$ . Particles with high  $\eta$  are lost down the beam pipe and are unobserved. The  $2\pi$  coverage in  $\phi$  combined with the large  $\eta$  range means that nearly the full angular phase space is enclosed. CMS is aptly known as a  $4\pi$  detector.

In analyzing particles, it is often necessary to consider nearby activity. The common practice is to select a cone in  $\eta$  and  $\phi$  space with a radius ( $\Delta R$ ) defined as:

$$\Delta R = \sqrt{(\Delta\eta)^2 + (\Delta\phi)^2} \quad (3.4)$$

### 3.2.2 Inner Tracking System

The inner tracker measures the position of charged particles as they move through the detector. Close to the beam pipe, the measurement is challenging because of the strong radiation flux. It is necessary for the inner tracker to have many detector channels each covering a small area. This has two benefits: the small area means that the particle's position can be measured with high precision, and the many detector channels mean that even in high fluxes most channels will be unoccupied and associated tracks will be distinguishable.

These two criteria are accomplished using pixel detectors and silicon microstrip detectors. Both are silicon detectors, and as charged particles pass through, they generate an electron-hole pair than can be detected without applying high voltages. Closest to the beam pipe, pixel detectors have the finest resolution, a surface area of  $100\ \mu\text{m} \times 150\ \mu\text{m}$ . For LHC luminosities of  $10^{34}\ \text{cm}^{-2}\text{s}^{-1}$ , the average occupancy of the pixel detectors is  $10^{-4}$  per bunch crossing. In the intermediate and outer layers of the tracker, the larger silicon microstrip detectors with cell sizes of  $10\ \text{cm} \times 80\ \mu\text{m}$  and  $25\ \text{cm} \times 180\ \mu\text{m}$  are used corresponding to occupancy levels of 2-3% and 1%, respectively [14].

### 3.2.3 Electromagnetic Calorimeter

Electromagnetic showers are the cascade of secondary electrons and photons produced when high energy photons or electrons interact with the detector material. The energy of these showers are absorbed and measured by the CMS Electromag-

netic Calorimeter (ECAL).

The ECAL is broken up into subsystems based on detector location: the barrel ECAL (EB) spanning  $|\eta| < 1.479$  and the endcap ECAL (EE) covering  $1.479 < |\eta| < 3.0$ .

Materials in the ECAL are described in terms of their radiation length ( $X_0$ ) and Moliere radius ( $R_M$ ). The radiation length is the distance an electron can travel before having its original energy reduced by a factor of  $\frac{1}{e}$ . The  $X_0$  is also  $\frac{7}{9}$  of a photon's mean free path. While  $X_0$  is useful for understanding both electrons and photons, the nature of how the two particles lose energy is different. Electrons lose energy continuously through interactions with the orbital electrons of the material, whereas photons can only be described by the probability an interaction occurs. The Moliere radius describes the size of a shower's transverse spread. The smaller  $R_M$ , the greater precision to which a shower's position can be measured.

The ECAL is composed of lead tungstate ( $PbWO_4$ ) crystal scintillators,  $X_0 = 8.9$  mm and  $R_M = 22$  mm. The barrel and endcap ECAL are 230 and 220 mm thick, respectively, corresponding to 25.8 and 24.7 radiation lengths. The crystals are  $22 \times 22$  mm<sup>2</sup> on the front side and  $29 \times 29$  mm<sup>2</sup> on the rear side, corresponding to  $0.0174 \times 0.0174$  in  $\eta - \phi$  space. Electromagnetic showers deposit 94% of their energy within a 3x3 crystal array. When the atoms in the  $PbWO_4$  are excited by the electromagnetic shower, they scintillate with a light yield of 4.5 photoelectrons per MeV[14].

The CMS detector also includes a laser system that takes continuous measurements ECAL crystal's light yields during data taking. This information is used for

calibration and is incorporated during reconstruction.

### 3.2.4 Hadron Calorimeter

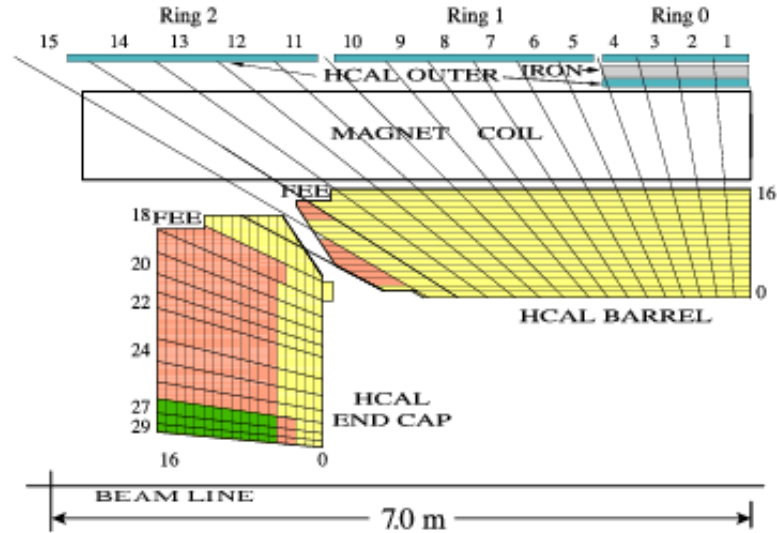


**Figure 3.6:** Quadrant of the HCAL showing the layout of the Barrel (HB) , EndCap (HE) , and Outer (HO) Hadron Calorimeters. Numbers on the top and the left show the segments in  $\eta$ , while the numbers on the bottom and right are scintillating layers.

Hadrons deposit their energy through hadronic showers. Even though hadrons are net color neutral, their composite quarks interact with the nuclei of material through the strong force. When an energetic hadron passes through matter, it creates a shower of particles, 90% of which are pions [15]. Energy is deposited into the calorimeter by two mechanisms. First, the neutral pions decay immediately via the electromagnetic force into a pair of photons, which generate electromagnetic showers. Second, during the hadronic shower there may be nuclear spallation, in which energetic hadrons knock protons and neutrons out of their nuclei. Most the energy deposited into the detector by relativistic hadrons comes from the electromagnetic

showers or freed low energy nucleons and not the relativistic particles themselves. In addition, there is a binding energy cost to ionize protons and neutrons, which shows up as lost energy. The fraction of energy deposited by electromagnetic showers increases logarithmically with the energy of the incoming hadron. This is because energetic charged pions produced in the initial hadronic shower are more likely to have secondary hadronic showers generating more neutral pions and subsequent electromagnetic showers[15]. Unlike the linear energy response of the ECAL, the HCAL response is nonlinear.

Just as radiation length describes energy loss in electromagnetic showers, the interaction length describes a similar exponential loss for hadronic showers in the material. CMS uses a sampling hadronic calorimeter made of alternating layers of brass absorber and active plastic scintillator. The HCAL has multiple subdetectors. The HB in the barrel region, the HE in the endcap region, the HF in the forward region (large  $\eta$ ), and the HO located outside the solenoid. Figure 3.6 show a diagram of the CMS HCAL.

The HCAL is also specifically designed for energy containment. It has many absorbing layers and minimum amount of dead space in  $\phi$ . This energy containment is crucial for measurements of the missing transverse energy ( $\cancel{E}_T$ ).

### 3.2.5 Superconducting Magnet

Between the Hadronic Calorimeter and the Muon System is CMS's 3.8 T superconducting solenoid magnet. It generates a magnetic field along the beam pipe,

so that charged particles' transverse trajectories are bent. Inside the solenoid the strength of the magnetic field is constant; outside the solenoid the field's direction is opposite and the strength is less uniform. The presence of the magnetic field is crucial for measuring transverse momenta.

### 3.2.6 Muon System

At the outer edge of the CMS detector, outside the solenoid, is the cavernous Muon System. It is not a muon calorimeter and muons lose only a fraction of their energy passing through. However, since other particle types are absorbed in the previous sub-detectors, ionizing events can be associated with a muon's passage. The muon's  $p_T$  is calculated by reconstructing the muon's path from tracks in the inner detector and the Muon System.

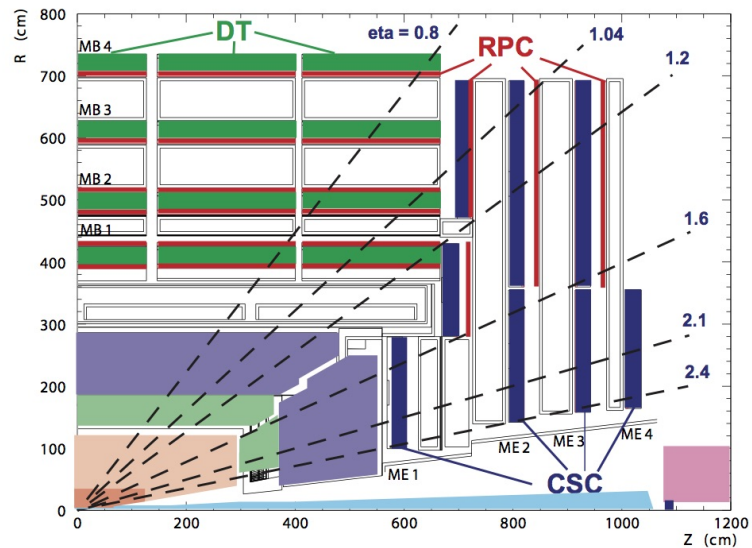


**Figure 3.7:** Layout of the Muon System. The drift tube (DT), resistive plate (RPC), and cathode strip (CSC) chambers are labeled.

Because of the large surface area to cover, gaseous detectors were utilized.



There are three different types in the Muon System. In the barrel, where the muon flux is low and the residual magnetic field is small, drift tube chambers (DT) are used. In the endcaps where the flux and magnetic field are both greater, cathode strip chambers (CSC) are used. In both the end cap and barrel, resistive plate chambers (RPC) are used. The RPC's have a coarser position sensitivity, but are faster, allowing muon events to be associated with a particular bunch crossing and are key for triggering [14]. The layout of the Muon System chambers are shown in Figure 3.7.

### 3.2.7 Triggers

CMS uses a two level trigger system. The Level-1 trigger is at the hardware level and is responsible for reducing the 40 MHz collision rate to 100 kHz. It makes use of custom hardware, in particular Field Programmable Gate Arrays (FPGAs) and fast Look-Up Tables (LUTs), to quickly perform logic operations. Information from the Calorimeters and the Muon System are used to make trigger primitives and decide whether the event passes the Level-1 trigger [14].

After the Level-1 trigger, the event is passed to the Higher Level Trigger (HLT). The HLT runs software similar to the off-line reconstruction. To quickly make decisions, the HLT is run over a processor farm and to reduce processing time, the reconstruction is only done in regions where Level-1 triggers are present. The reconstructed objects are used to select events that are of interest to physics analyses. The HLT trigger reduces the rate to approximately 100 Hz, the rate at

which events can be written to storage [14].

### 3.2.7.1 HO Minimum Ionization Bit Trigger

During the first long shut down (LS1), the HO was upgraded with new Silicon Photomultipliers (SiPM). These photodetectors had greatly improved signal to noise resolution and allowed for minimum ionization particles (MIP), such as muons, to be observed. Figure 3.8 shows a muon MIP signal in the HO easily distinguishable from the electronic noise.

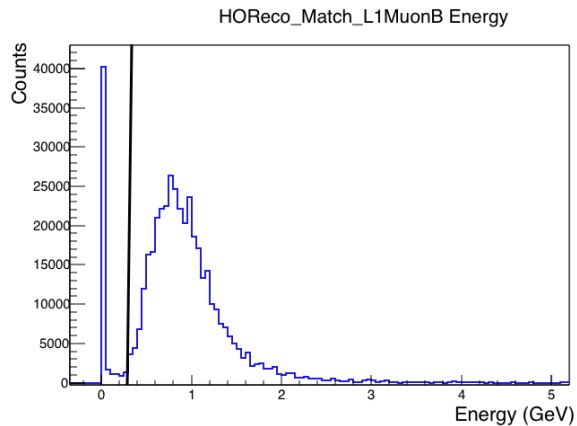


**Figure 3.8:** For simulated data, distribution of the maximum HO RecHit energy for hits within  $0.2 \Delta R$  of a L1 Muon. A clear MIP bump can be seen at 1 GeV separate from the noise pedestal. For the proposed L1 Muon + MIP trigger the black line represents a threshold energy cut of 0.3 GeV.

With the improved resolution, proposals were made to use the HO as part of the Level-1 Muon trigger. Located outside the solenoid, the HO is free from all particles except muons and high  $p_T$  jets. The geometry of the HO is also well suited for integration. The HO is the first layer of active material between the solenoid and the Muon System and is segmented into the same  $\phi$  sectors.

To remove muon fakes and reduce the Level-1 trigger rate, a new trigger with an added MIP bit requirement was proposed. The presence of an associated MIP in the HO was defined as a RecHit with an energy above 0.3 GeV that was within  $\Delta R < 0.2$  of the L1 Muon.

For the trigger's efficiency, signal muons were defined as L1 muons spatially matched to a HLT muon,  $\Delta R < 0.4$ . For the matching, the position of the HLT seed propagated with the stepping helix propagator from the interaction vertex to the entrance of the Muon System. The new trigger's efficiency was defined as:

$$\epsilon = \frac{\text{L1Muon \& MIP \& HLT}}{\text{L1Muon \& HLT}} \quad (3.5)$$

If the level-1 muon cannot be matched to a HLT, it was considered background. The background reduction was defined as,

$$f = \frac{\text{L1Muon \& MIP \& No HLT}}{\text{L1Muon \& No HLT}} \quad (3.6)$$

The efficiency of the L1Muon + MIP trigger as a function of  $p_T$  and as a function  $\eta$  is shown in Figure 3.9. The HO tiles are  $0.087 \times 0.087$  in  $\eta$  and  $\phi$  space. The average efficiency is  $88.9 \pm 1.2$  %. Meaning that most real muons are accompanied by a MIP in the HO. In fact, the efficiency can be as high as 98%, and the drop is mostly due to detector gaps in certain  $\eta$  regions of the HO.

However, level-1 muon triggers are mostly populated by real muons, which the MIP requirement does not filter [16]. The new trigger's background reduction,  $89.5 \pm 0.4$  %, was not statistically different from the efficiency. A comparison of

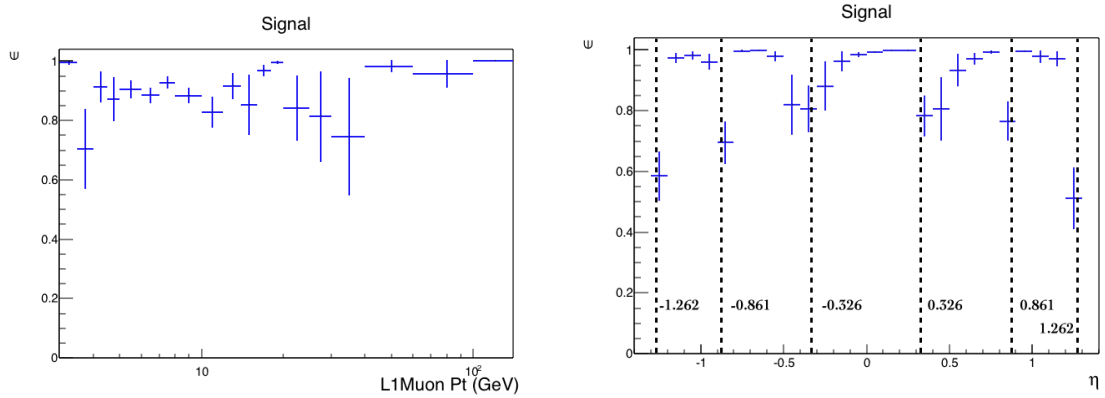


**Figure 3.9:** As a function of  $p_T$  the efficiency of the L1 Muon + MIP Trigger compared to the current L1 Muon Trigger (left), and the efficiency as a function of  $\eta$  (right). The location of the wheel separations are shown by the dotted black lines.

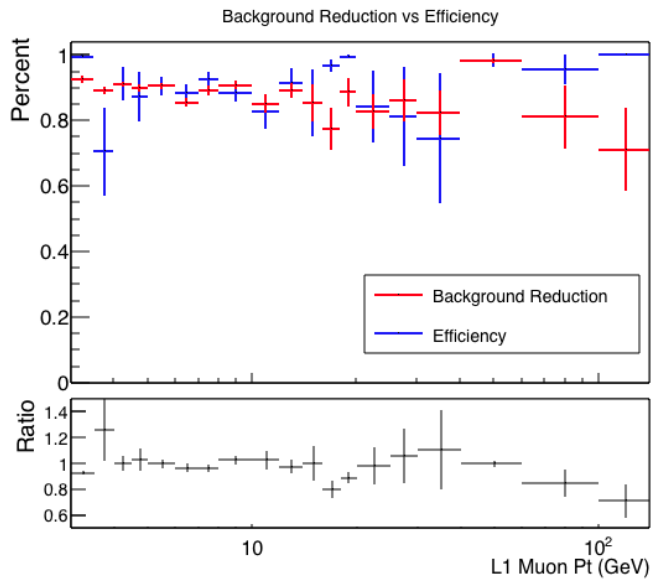


**Figure 3.10:** As a function of  $p_T$ , the background reduction of the L1 Muon+MIP trigger compared to the current L 1 Muon trigger (red) and the efficiency (blue). The ratio of background reduction over efficiency is shown on the bottom plot.

efficiency and background reduction is shown in Figure 3.10. Simulation confirms that the new HO will be able to identify muon MIPS, but more novel approaches are necessary to incorporate the HO information into the level-1 muon trigger.

## Chapter 4

### Event Reconstruction

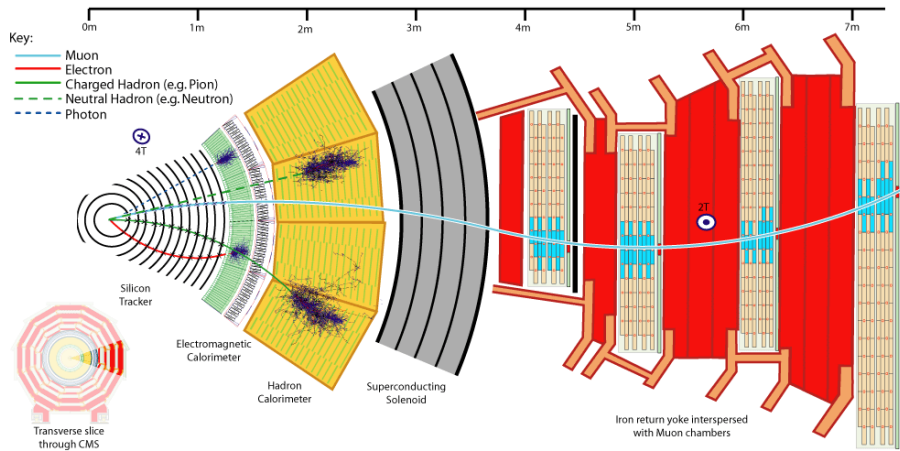


**Figure 4.1:** Diagram of how different particles interact with the CMS detector. Charged particles leaves tracks in the Inner Tracker, electrons and photons deposit energy in the ECAL, hadrons deposit energy in the HCAL, and muons leave tracks in the Muon System

Chapter 3 described the subdetectors of the CMS experiment and their interactions with particles. Figure 4.1 shows how different particles pass through the detector. This chapter describes event reconstruction, detailing the algorithms used to quantify particle interactions and build physics objects. The reconstructed object collections are used by the HLT for triggering and off-line for physics analyses.

Reconstruction takes place in three steps. At the first level is local reconstruction. It takes the digitized readouts of the CMS subsystems and makes “RecHits”. RecHits for the Inner Tracker and Muon System subsystems contain position and track segment information. RecHits for the calorimeters give position and energy

information. During local reconstruction, corrections for detector calibration and alignment are applied.

The second step is global reconstruction. In this step, the subsystems of a sub-detector are combined. For example, global reconstruction of the Muon System combines the CSC, DT, and RPC subsystems, but does not include hits from the Tracker. For this reason, these reconstructed muons are often known as “Stand-alone” muons. At the global level, pattern recognition for the tracker and grouping energy deposits in the ECAL and HCAL into “Calo Towers” also occurs.

In the last step, high level reconstruction, the full detector is used and the subdetectors are combined to make reconstructed particle collections. In this chapter, the procedure used for electrons, muons, jets, and missing transverse energy is described. Common to many of these reconstructed particle collection is the use of the Particle-Flow algorithm, described in Section 4.5.

The software handling event reconstruction is the CMS Software Framework (CMSSW). The framework is written in the C++ and Python programming languages with events stored in ROOT files [17].

## 4.1 Track and Vertex Reconstruction

Reconstructing a particle’s trajectory requires making multiple measurements of its position as it passes through the detector. The trajectory near the interaction point is of particular interest because it allows the detection of short lived particles, such as b-quarks. For charged particles, the Inner Tracker is used for the construc-

step	seed type	seed subdetectors	$p_T$ (GeV)	$d_0$ (cm)	$ z_0 $
0	triplet	pixel	$>0.6$	$<0.02$	$<4.0\sigma$
1	triplet	pixel	$>0.2$	$<0.02$	$<4.0\sigma$
2	pair	pixel	$>0.6$	$<0.015$	$<0.09$ cm
3	triplet	pixel	$>0.3$	$<1.5$	$<2.5\sigma$
4	triplet	pixel/TIB/TID/TEC	$>0.5 - 0.6$	$<1.5$	$<10.0$ cm
5	pair	TIB/TID/TEC	$>0.6$	$<2.0$	$<10.0$ cm
6	pair	TOB/TEC	$>0.6$	$<2.0$	$<30.0$ cm

**Table 4.1:** Seed types and the selection criteria for the six iterations of the Combinatorial Track Finder

tion of tracks. This is handled by the Combinatorial Track Finder (CTF) algorithm, a modified version of a combinatorial Kalman filter. The CTF is an iterative process. The algorithm starts by identifying a seed, from 2-3 hits. It then extrapolates the path of the particle to see if additional hits can be added. After a track is identified, the associated hits are removed from the search. The algorithm then repeats the search with the track identification criteria loosened. Table 4.1 shows the different seed types and selection criteria for the six iterations of the CTF.

The reconstructed tracks are then used to identify vertices. These include the hard scattering vertex as well as vertices from pileup. Tracks are required to pass selection criteria on their transverse impact parameter ( $d_0$ ) the number of strip and pixel hits, and on the normalized  $\chi^2$  of the track fit. The selected tracks are clustered into vertices using a deterministic annealing algorithm.

## 4.2 Muon Reconstruction

The CMS detector was designed to be especially sensitive to muon reconstruction. Within the Muon System’s range,  $|\eta| < 2.4$ , CMS has an efficiency of 95%



with a fake rate below 1% [18].

Muons are identified by tracks in the Inner Tracker combined with tracks in the Muon System. The reconstructed muon collection consists of 3 categories: Standalone Muons, Global Muons, and Tracker Muons. Standalone Muons are generated during the global reconstruction step and only use information from the Muon System. They account for less than 1% of final reconstructed muons. The other two categories combine the Inner Tracker and Muon System. At low momenta, the Tracker Muon method is effective. All tracks in the Tracker with  $p_T > 0.5$  GeV and  $p > 2.5$  GeV are extrapolated into the Muon System. If the Tracker tracks can be matched with a track segment in the Muon System, they qualify as a Tracker Muon [18]. The Global Muon method is preferred for high momenta muons, where the Muon System's larger size gives it the advantage in measuring the slight curvature of the muon's trajectory. The Standalone Muon track and Tracker track are combined using a Kalman-filter technique.

Muons identified as both Tracker Muons and Global Muons are merged into one candidate. A "sigma switch" method is used for momentum assignment. When both the tracker method and global muon method estimate a  $p_T > 200$  GeV and have a charge-to-momentum ratio within  $2\sigma$  of each other, the Global Muon measurement is taken. In the other cases, the tracker momentum measurement is selected.

### 4.3 Electron Reconstruction

Electrons are identified by hits in the Inner Tracker and energy deposits in the ECAL. For the CMS ECAL, electromagnetic showers deposit 94% of their energy within a 3x3 crystal array. However, as the initial electron interacts with matter in the detector it produces bremsstrahlung photons. These photons are not bent in the magnetic field, so the initial electron's energy will be distributed in multiple clusters at the same  $\eta$  but spread across  $\phi$ . The amount of bremsstrahlung radiation depends on the  $p_T$  of the electron and on the amount of detector material it passes through. However, 33% - 88% of the electron's energy can be radiated off, so collecting the bremsstrahlung photons is crucial. It is also possible for the bremsstrahlung photons to produce secondary electrons via pair production. If these electrons are soft and produced in the tracker material, they can be trapped by the  $\vec{B}$  field and not deposit energy in the ECAL.

Electron Reconstruction uses a "Super Clustering" algorithm to group these energy deposits. The algorithm starts by finding a seed crystal with an energy above a threshold value,  $E_T > E_{T,seed}^{min}$ . It then searches for nearby clusters within an array of crystals narrow in  $\eta$  and wide in  $\phi$ . If the energy in the array is above a threshold ( $E_{array}^{min}$ ) the array is identified as a clusters. Then all the clusters associated with the initial seed are grouped into a supercluster. The energy of the supercluster is the sum of the energy deposited in the crystals. The position of the supercluster is

found by taking the weighted average of the crystals' position:

$$\vec{x} = \frac{\sum \vec{x}_i \cdot w_i}{\sum w_i} \quad (4.1)$$

where the weight depends on the log of crystal energy.

$$w_i = w_0 + \log \frac{E_i}{\sum E_j} \quad (4.2)$$

Particle-Flow (Sec 4.5) uses its own version of clustering to create the Particle-Flow electrons.

The second part of Electron Reconstruction recreates the track. Normally, charged particle tracks are inferred from hits in the Inner-Tracker. However, since electrons lose a significant amount of energy in the Tracker to bremsstrahlung radiation, the curvature of their tracks changes, making them more difficult to reconstruct. A dedicated procedure is used for reconstructing electron tracks.

Two methods are used to join the Inner-Tracker and ECAL information, ECAL driven and Tracker driven. ECAL-driven is the general method. It propagates from the position of the supercluster back to the Tracker to search for hits. The Tracker driven method is used for low  $p_T$  cases where  $E_T < 4$  GeV. The Tracker driven method extrapolates from hits in the pixel detectors.

## 4.4 Photon Reconstruction

Photons are reconstructed from superclusters in the ECAL without associated tracks in the Inner-Tracker. The building of superclusters in the ECAL was described in section 4.3.

As photons travel through the detector, they can convert to electron-positron pairs. The trajectories of the charged electron and positron are bent away from the photon because of the magnetic field. To describe the spread of energy from these conversions, CMS uses the  $R_9$  variable.  $R_9$  is defined as the ratio of the energy within a 3X3 crystals array divided by the energy of the supercluster. If  $R_9$  is below 0.94 (0.95) for the barrel (endcap), then the energy of the photon is estimated as the energy in the supercluster. For the unconverted case where  $R_9$  is above the threshold values, the the energy is taken as the sum of energies deposited in a 5x5 crystal array [19].

If photons converts in the Tracker material, then the electron-positron pairs will leave hits in the Inner-Tracker. These hits are reconstructed into tracks. Particle-Flow and other more advanced algorithms include these conversion tracks in the identification of photons [19].

There are additional variables from the photon reconstruction that are important for the rejection of misidentified photons. For electron rejection, there are the Conversion-Safe and Pixel Seed Electron Vetoes. The Conversion-Safe Veto requires that there are no charged-particle tracks with a hit in the inner layer that point to the photon supercluster. The Pixel Seed Electron Veto is stronger, requiring that

no two pixel hits in the tracker can be extrapolated to the photon's supercluster position [19].

Photon reconstruction variables are also utilized to estimate jets misidentified as photons. The Charge Hadron Isolation variable quantifies the relative hadronic activity near a photon. It is defined as the ratio of  $\sum p_T$  for Particle-Flow charged hadrons within a cone around the photon and matched to the primary vertex, divided by the photon  $p_T$ . Describing the shape of the electromagnetic shower, the  $\sigma_{\eta\eta}$  variable is the shower's lateral extension. It is defined as the distribution of energy in a 5x5 crystal array centered on the seed crystal.

For the analysis, special distinction is also made between photons reconstructed in the barrel and endcap regions of the ECAL. Barrel photons are defined as those with  $|\eta| < 1.4442$  and the endcap photons are between  $|\eta| > 1.566$  and  $|\eta| < 2.5$ . Photons located in the gap region between the barrel and the endcap are not used in the analysis.

## 4.5 Particle-Flow

High level reconstruction often uses CMS's Particle-Flow algorithm. Particle-Flow is based on the philosophy that knowledge of how particles have already been reconstructed can improve the reconstruction of the remaining particles. The Particle-Flow algorithm was commissioned with the first of the LHC collisions in 2010 and outperforms simpler reconstruction methods, particularly for jet and  $\cancel{E}_T$  reconstruction [20].

Particle-Flow candidates are built from basic elements: charged tracks in the Inner-Tracker, energy clusters in the ECAL and HCAL, and muon tracks from the Muon System. These elements are constructed from the subsystem RecHits.

The elements are associated with each other using a linking algorithm. Each pair of elements are matched and a quality value is assigned based on the likelihood that the elements come from same particle. The group of links that produce the highest quality match are called a block and are sent forward to be analyzed [7].

In the Particle-Flow algorithm muons are identified first. If the tracks from the muon system and the tracker give consistent momentum measurements then the track is removed from the block. In addition, the muon's MIP energy is subtracted from the calorimeters. Second, electrons are identified by tracks in the Tracker linked with energy deposits in the ECAL. Once identified, the electrons' tracks and clusters are also removed from further analysis [7]. The remaining charged particle tracks are associated with charged hadrons. Charged hadrons leave clusters in both the ECAL and HCAL and their  $p_T$  can be extrapolated from their tracks. The tracks are then removed from further analysis and the energy of the particle is removed from the calorimeters. Preference is given for the charged hadron's energy to be removed from the HCAL. After the removal, excesses of energy deposited in the calorimeters are interpreted as coming from neutral particles. Excesses in the ECAL are associated with Particle-Flow photons and excesses in the HCAL with Particle-Flow neutral hadrons. Similarly, when there are clusters not matched to any tracks, those in the ECAL are identified as photons and those in the HCAL are identified as neutral hadrons. This method will sometimes mistake energy deposits

in the ECAL from neutral hadrons as coming from photons, but this is a small effect since neutral hadrons deposit only 3% of their energy into the ECAL [7]. The particles reconstructed through the Particle-Flow algorithm are then clustered into Particle-flow Jets using an iterative cone algorithm.

## 4.6 Jet Reconstruction

Jets are the collimated stable hadrons produced from the hadronization of a hard scatter quark or gluon. The LHC's large QCD cross section means that jets will dominate high  $p_T$  events. In preparation for hadron colliders, methods of jet reconstruction have received much study. CMS uses an anti-kt clustering algorithm [21].

Using the candidate particles' four vectors, distance parameters between two particles ( $d_{ij}$ ) and between a particle and the beam ( $d_{iB}$ ) are calculated:

$$d_{ij} = \min(k_{T_i}^{2p}, k_{T_j}^{2p}) \cdot \frac{\Delta R_{ij}^2}{R^2} \quad (4.3)$$

$$d_{iB} = k_{T_i}^{2p} \quad (4.4)$$

$\Delta R$  is the separation between two points in  $\eta$  and  $\phi$  space defined in equation 3.4. If the smallest distance is  $d_{ij}$  then the two particles are merged. If  $d_{iB}$  is the smallest, then the particle is identified as a jet and removed. For CMS's jet reconstruction  $\Delta R = 0.5$ , with the effect that any final jets must be separated by at least 0.5.

The input for the clustering is normally the particle-flow candidates (PF jets). However, alternative methods for jet reconstruction use the energy and position of the calorimeter towers (CALO jets) or the calorimeter towers plus information in the tracker (JPT jets).

## 4.7 MET Reconstruction

For any proton-proton collision, the net transverse momentum should balance to zero. CMS is a hermetic detector. Through the ECAL and strong energy containment in the HCAL, electrons, photons, and jets within the  $|\eta|$  coverage are expected to deposit all their energy inside the detector. From the Inner-Tracker and Muon System tracks, the transverse momenta of muons are measured. Therefore, an imbalance in the total transverse energy, missing transverse energy ( $\cancel{E}_T$ ), is assumed to be carried by non-interacting particles, such as neutrinos or new beyond the Standard Model particles.

Methods for measuring  $\cancel{E}_T$  include using just the calorimeters or calorimeters plus corrections from the track information. The best performance, though, comes from Particle-Flow. Particle-Flow measures  $\cancel{E}_T$  as negative the sum of all the Particle-Flow candidate's  $p_T$  [7]:

$$\cancel{E}_T = -\sum \vec{p}_T \quad (4.5)$$

In the analysis, Type-1 corrected missing transverse energy ( $\cancel{E}_T^{\text{Type-1}}$ ) is utilized. This is the same definition of  $\cancel{E}_T$ , but in the summation, jet  $p_T$  is replaced by jet  $p_T$



with energy corrections applied. Non-jet particles are unaffected.

$$\cancel{E}_T^{\text{Type-I}} = - \sum_{jet} \vec{p}_T^{JEC} - \sum_{non-jet} \vec{p}_T \quad (4.6)$$

The jet energy corrections include corrections for the offset from pile-up and electronic noise, variations in the jet response with  $p_T$  and  $\eta$ , variations with the electromagnetic energy fraction, and corrections for the underlying jet flavor (u, d, c, b, gluon) [22].

## Chapter 5

### Event Simulation

Simulations are frequently used in high energy physics. For this analysis, simulated signal events were used to calculate fiducial acceptances, simulated events were produced for dimension-8 EFTs, and certain background estimates were done through simulation. This section describes how LHC proton-proton collisions events are simulated. Event generation is a multi-step process, including matrix-element based generators, modeling of quark hadronization, and showering of initial and final state particles. These steps produce the generator level, “true”, state of the particles. Separate simulators are responsible for modeling how particle interact with the detector, and their output is fed into the CMS reconstruction algorithms.

#### 5.1 Generators

Colliding patrons interact through many physical processes each with its own cross section. Specialized software exists to handle the matrix element calculations and to produce sets of simulated events. These programs are designed to be highly automated and capable of running in parallel. Examples include ALPGEN [23], MADGRAPH [24], PYTHIA8 [25], SHERPA [26], and VBFNLO [35]. The matrix-element based generators follow a similar strategy. Initial and final state particles are specified, the generator creates a topology of physically allowed diagrams, ampli-

tudes are calculated, cross sections are integrated, and a set of events are produced. This dissertation focuses on MADGRAPH5-AMC@NLO and PYTHIA8, the generators used to produce the main MC samples of the analysis. VBFNLO was used for checking the unitarity bounds of the EFTs.

MADGRAPH5-AMC@NLO handles  $2 \rightarrow n$  matrix element calculations and can do so at LO or NLO in QCD. For the LO calculations, the software calculates the tree level matrix elements. For NLO, one-loop matrix elements corrections and the subtraction of infrared singularities are also computed [32]. For events generated at LO, it is possible to produce an unweighted sample. However at NLO, the integration of the one-loop contributions leads to interference effects and events with negative weights. Thus while their magnitudes may be equal, there must be a weight to account for the sign difference.

For the generation of events, MADGRAPH requires the user to specify a model, corresponding to the Lagrangian of the theory as well as its coupling and mass values. Mirroring the Feynman rules for a Lagrangian, the rules governing how matrix elements are built are standardized in the FEYNRULES package [27]. This standardization allows physicists to produce custom models using the Universal FEYNRULES Output format (UFO), ie models for EFTs .

The user also specifies kinematic cuts for the event generation. To avoid divergences in the matrix element calculations from radiation that is collinear or soft, cuts on a particle's energy and the  $\Delta R$  separation between two particles are introduced. To account for smearing during reconstruction, these cuts are made looser than the ultimate phase-space of the analysis.

MADGRAPH output is written in a standard Les Houches Events format (LHE)

[28], allowing for generated events to be easily fed to other simulators.

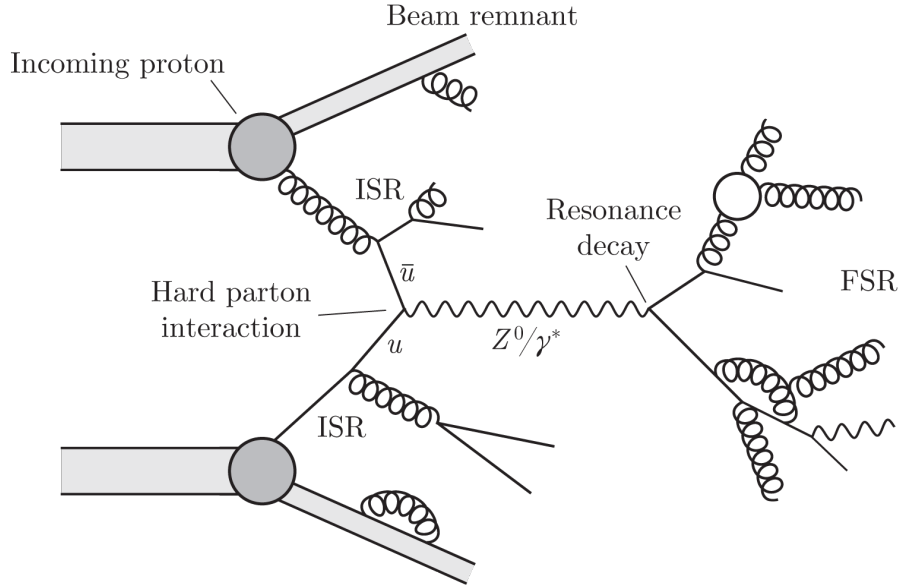


**Figure 5.1:** Example of a proton-proton collision, showing the incoming protons, the hard parton interaction, the outgoing partons. The Initial and Final State radiation is also labeled.

PYTHIA8 interfaces with MADGRAPH to handle the initial and final state gluon and photon radiation, as well as hadronization [25]. PYTHIA8 generates showers based on empirical models that have been “tuned“ to data. For the decay  $\tau$  particles, the TAUOLA package within PYTHIA8 is utilized [29].

## 5.2 PDF

In simulating collisions, event generators must specify the types of particles colliding and their center-of-mass energy. As noted in theory Section 2.1, the protons used at the LHC are not fundamental particles. They are composite particles made up of the three valence quarks and a quark gluon sea.

Deciding how the proton's momentum is distributed between the constituent particles is handled by Parton Distribution Functions (PDF). The PDF,  $f(x, Q^2)$ , is the probability density for finding a parton with a fraction of the proton's longitudinal momentum ( $x$ ) at the energy scale of the collision ( $Q$ ). PDFs are included in the cross-section calculation as:

$$\sigma = \int dx_1 dx_2 \cdot f_i(x_i, Q^2) \cdot f_j(x_j, Q^2) \cdot \hat{\sigma}_{ij}(x_1, x_2, Q^2) \quad (5.1)$$

where  $\hat{\sigma}_{ij}$  is the cross section for the process given just the two partons [30].

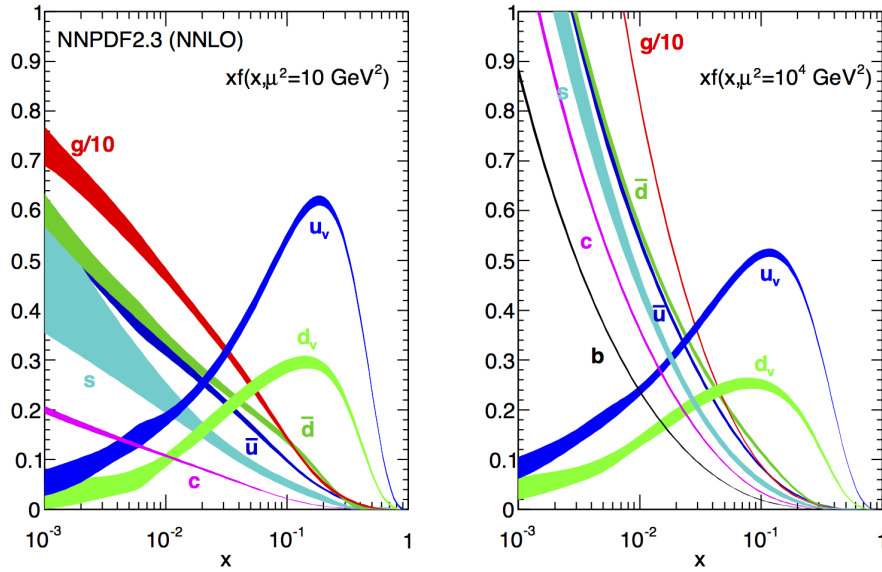


**Figure 5.2:** Next, Next to Leading Order Parton Distribution Functions calculated by NNPDF. The PDF at two different energy scales are shown,  $Q = 10$  GeV and  $Q = 10^4$  GeV. NB that the gluon PDF is scaled down by a factor of 10.

PDFs are calculated from experimental measurements, and differ depending on the choices made to model the proton. NLO and NNLO PDFs now exist. Common PDFs include the recent Neural Network Parton Distribution Function (NNPDF),

the 2010 results from the Coordinated Theoretical Experimental Project on QCD (CT10), and the Martin-Stirling-Thorne-Watt (MSTW) set. LHAPDF is a single C++ library where all of the major PDF sets can be accessed.

### 5.3 Reweighting

In many physics analysis, it is useful to simulate signal samples for a range of coupling strengths or in a new particle search, multiple masses. The generation of each of these samples, particularly the hadronization and the particle reconstruction can be computationally intensive. Reweighting streamlines the process, taking advantage of the insight that the new coupling strength or mass only affect the matrix element calculation. Hadronization and the detector response are not affected. For the parameter being scanned, reweighting works by having each value of the parameter use a single underlying set of events. For each event, a range of weights is calculated corresponding to the range of parameter values. Weight is defined as the ratio of the new parameter's matrix element squared divided by the square of the original matrix element:

$$W_{new} = |M_{new}|^2 / |M_{old}|^2 * W_{old} \quad (5.2)$$

In choosing the original value for the underlying set, it must be one that populates the tails of the event distribution. Events can always be weighted down, but a 0 event cannot be weighted up. For the  $W\gamma\gamma$  analysis, this means choosing a large magnitude, anomalous quartic gauge coupling just beyond the range of coupling

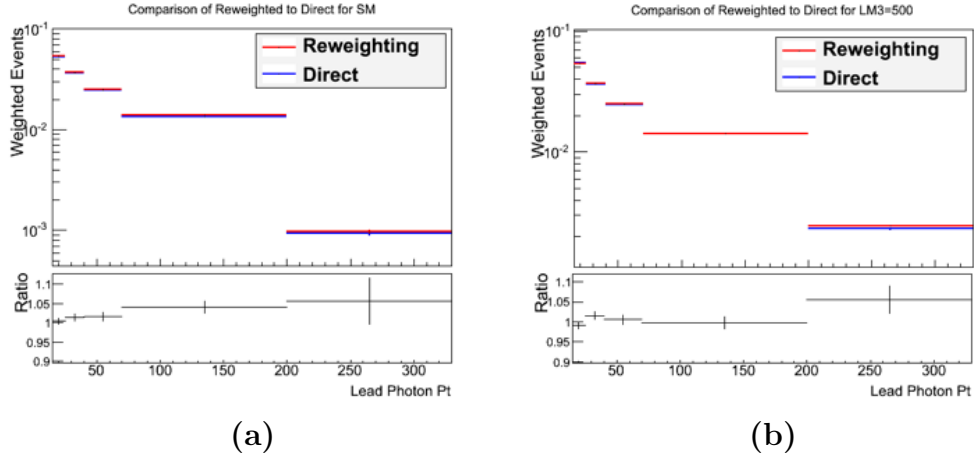


**Figure 5.3:** Comparison of the lead photon distribution of events generated with a reweighting method (red) and the standard production method (blue). Figure on the left is for a SM sample and the Figure on the right is for a sample with a dimension-8 effective field theory, LM3, with  $f_{M,3} = 500 \text{ TeV}^{-4}$ .

strengths being studied.

Using MADGRAPH produced events, the reweighting method is validated by comparing the distribution of events produced directly to events reweighted to that coupling strength. (See figure 5.3) The reweighting method is found to give consistent results.

## 5.4 Dressing Leptons

Lepton universality describes the feature of the SM that all three lepton flavors have the same couplings to the gauge bosons. In the limit that the electron and muon are approximated as massless, they behave as identical particles. This is advantageous for the analysis, because then the two channels can be combined, and the cross section for a single lepton flavor,  $\ell$ , decay can be measured.

The massless approximation breaks down when electrons or muons produce

collinear radiation. Because of their smaller mass, electrons are more likely than muons to emit collinear photons.

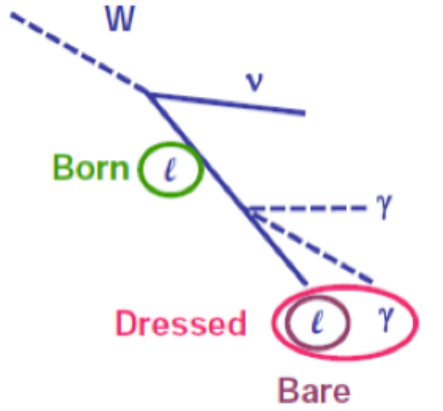


**Figure 5.4:** Diagram of the dressing procedure. A generator, such as PYTHIA8 radiates photons off the born lepton. Dressing adds back on the photons that are within a  $\Delta R$  cut of 0.1

This is accounted for by introducing a dressing procedure onto the generator level leptons. Photons above 500 MeV within  $\Delta R < 0.1$  of a lepton are designated as dressing photons. The four-vectors of the dressing photons are added onto the lepton's four-vector. Dressing photons are removed from the rest of the analysis and the dressed lepton's kinematics are used. After the dressing, the generator level electron and muon channel can once again be treated as the same. In addition, the kinematics of the new dressed leptons are closer to the born lepton produced by the initial matrix-element generator.



## 5.5 Detector Simulation

The generator produced hard-scatter events are often used as the input for simulation of the CMS detector. Simulation of the particles' path and their energy loss is handled by the GEANT toolkit [31]. For the greatest possible accuracy, the simulated detector geometry is highly detailed accounting for dead areas in the detector and including alignment and calibration information. The software produces simulated hits, called "SimHits". In the digitization step, SimHits are used to simulate the readout of the detector hardware. These simulated readouts are passed through the same CMSSW reconstruction algorithms as used with real collisions.

## Chapter 6

### Data Analysis

The  $W\gamma\gamma$  analysis uses a straight-forward “cut-and-count” approach. Selection cuts define a signal region and the number of observed events within the region are counted. For leptonic  $W\gamma\gamma$  events,  $pp \rightarrow \ell\nu\gamma\gamma$ , the signal region is a final state with a single lepton, two photons, and missing transverse energy. Two lepton channels are studied: the electron channel and the muon channel. To detect the presence of a neutrino, the analysis uses the  $\cancel{E}_T$  dependent variable, transverse mass ( $M_T$ ) (See Section 6.2.5). Events are chosen with a  $M_T$  consistent with  $W$  decay to a lepton and neutrino. The signal region is inclusive in jet multiplicity, allowing that EWK  $W\gamma\gamma$  production is often accompanied by additional QCD jets.

While  $W\gamma\gamma$  events are selected for, other processes also contribute to the signal region.  $Z\gamma\gamma$  production where a  $Z$  decays to a pair of leptons may also pass the cuts if one of the leptons is outside the acceptance of the ECAL ( $|\eta| < 2.5$ ) or is too soft to be selected. In other cases, processes like  $W$ + jets where the jets are misidentified as photons make it into the signal region. These non- $W\gamma\gamma$  processes are “the background”. The signal region is chosen to maximize the number of true  $W\gamma\gamma$  events while minimizing the background. A great deal of study is done to ensure that the number of background events is accurately estimated.

For the cross section measurement, a fiducial region is defined. Simulated

signal events are used to calculate the fiducial acceptance factor ( $C_{W\gamma\gamma}$ ) and to remove the  $\tau$  background.

Signal and background distributions for a number of variables are studied. In particular, binning the data as a function of the detector region of the two photons and the lead photon  $p_T$  is integral to the calculation of the  $W\gamma\gamma$  significance and the limit setting.

## 6.1 Samples

Two types of event samples are used in the analysis. The first are data samples physically collected from the detector. Named after the trigger used in their selection, data samples are used for observed event counts and in making data-driven background estimates. The second type of samples is simulated Monte Carlo (MC). Identified by the physics process they model, these samples are used for the expected  $W\gamma\gamma$  signal, calculating the fiducial acceptances, estimating backgrounds, and modeling anomalous quartic gauge couplings. Both types of samples are stored in the CMS standard Event Data Model (EDM) format.

### 6.1.1 Data Samples

The datasets used in this analysis are from the Run 1 2012, 8 TeV collisions. Events are selected that have a single electron or single muon trigger. The electron HLT is un-prescaled and corresponds to an electron  $p_T$  threshold of 27 GeV (HLT\_Ele27\_WP80'). For the muon channel, events are required to pass one of

Datasets
/SingleMu/Run2012A-22Jan2013-v1/AOD
/SingleMu/Run2012B-22Jan2013-v1/AOD
/SingleMu/Run2012C-22Jan2013-v1/AOD
/SingleMu/Run2012D-22Jan2013-v1/AOD
/SingleElectron/Run2012A-22Jan2013-v1/AOD
/SingleElectron/Run2012B-22Jan2013-v1/AOD
/SingleElectron/Run2012C-22Jan2013-v1/AOD
/SingleElectron/Run2012D-22Jan2013-v1/AOD

**Table 6.1:** Single lepton data sets from the CMS 2012 Run. Electron and muon channel each corresponds to an integrated luminosity of  $19.4 \text{ fb}^{-1}$ .

two HLT, un-prescaled triggers. The triggers correspond to a muon  $p_T$  threshold of 24 GeV with one of the triggers optimized for  $|\eta| < 2.1$  (HLT\_IsoMu24\_eta2p1 || HLT\_IsoMu24). Collisions are only included in the data if they occurred when both CMS and the LHC were fully operational. The integrated luminosity for the electron and muon datasets were  $19.4 \text{ fb}^{-1}$ .

## 6.1.2 Monte Carlo Samples

### 6.1.2.1 $W\gamma\gamma$ Samples

The  $W\gamma\gamma$  signal is modeled using two NLO MC samples, an ISR-enriched sample and an FSR-enriched sample. Two samples are made because the FSR diagrams dominate the total cross section, but the QGC diagrams are of physical interest. By making a separate sample in a kinematic region where the FSR contribution is suppressed (ISR-enriched) events sensitive to the QGC diagram are oversampled. The split is accomplished during MADGRAPH generation by introducing a discriminant on the sum of two body lepton and neutrino mass ( $M_{\ell\nu}$ ) and the three body lepton,

Signal MC Datasets	$\sigma$ (pb)
(NLO) /Wgg_enhanced_ISR_8TeV_madgraph_pythia8/Summer12DR53X-PU_S10_TuneCUETP8M1_START53_V19-v1/AODSIM	0.159
(NLO) /Wgg_enhanced_FSR_8TeV_madgraph_pythia8/Summer12DR53X-PU_S10_TuneCUETP8M1_START53_V19-v1/AODSIM	1.137
(LO) /LNUGG_enhanced_ISR_8TeV_madgraph/Summer12_DR53X-PU_S10_START53_V19-v1/AODSIM	0.319
(LO) /LNUGG_enhanced_FSR_8TeV_madgraph/Summer12_DR53X-PU_S10_START53_V19-v1/AODSIM	1.840
Background MC Datasets	$\sigma$ (pb)
/WJetsToLNU_TuneZ2Star_8TeV-madgraph-tarball/Summer12_DR53X-PU_S10_START53_V7A-v2/AODSIM	36257.2
ZGG_8TeV-madgraph-pythia8/Summer12DR53X-PU_S10_START53_V19-v1/AODSIM	0.125
/WH_ZH_HToGG_M-125_8TeV-pythia6/Summer12_DR53X-PU_RD1_START53_V7N-v2/AODSIM	2.5e-3
/ZZTo4e_8TeV-powheg-pythia6/Summer12_DR53X-PU_RD1_START53_V7N-v2/AODSIM	0.07691
/ZZTo4mu_8TeV-powheg-pythia6/Summer12_DR53X-PU_RD1_START53_V7N-v1/AODSIM	0.07691
/ZZTo4tau_8TeV-powheg-pythia6/Summer12_DR53X-PU_RD1_START53_V7N-v1/AODSIM	0.07691
/ZZTo2e2mu_8TeV-powheg-pythia6/Summer12_DR53X-PU_RD1_START53_V7N-v2/AODSIM	0.1767
/ZZTo2e2tau_8TeV-powheg-pythia6/Summer12_DR53X-PU_RD1_START53_V7N-v1/AODSIM	0.1767
/ZZTo2mu2tau_8TeV-powheg-pythia6/Summer12_DR53X-PU_RD1_START53_V7N-v1/AODSIM	0.1767
/GluGluToZZTo2L2L_TuneZ2star_8TeV-gg2zz-pythia6/Summer12_DR53X-PU_S10_START53_V7A-v1/AODSIM	12.03
/GluGluToZZTo4L_8TeV-gg2zz-pythia6/Summer12_DR53X-PU_S10_START53_V7A-v1/AODSIM	4.8
/WWJetsTo2L2Nu_TuneZ2star_8TeV-madgraph-tauola/Summer12_DR53X-PU_RD1_START53_V7N-v1/AODSIM	5.995
/WZJetsTo2L2Q_TuneZ2star_8TeV-madgraph-tauola/Summer12_DR53X-PU_RD1_START53_V7N-v1/AODSIM	1.755
/WZJetsTo3LNU_TuneZ2_8TeV-madgraph-tauola/Summer12_DR53X-PU_RD1_START53_V7N-v1/AODSIM	1.057
/ZZJetsTo2L2Nu_TuneZ2star_8TeV-madgraph-tauola/Summer12_DR53X-PU_S10_START53_V7A-v3/AODSIM	0.32
/WWGJets_8TeV-madgraph_v2/Summer12_DR53X-PU_RD1_START53_V7N-v1/AODSIM	2.17
/WWWJets_8TeV-madgraph/Summer12_DR53X-PU_RD1_START53_V7N-v1/AODSIM	0.08058
/WWZNoGstarJets_8TeV-madgraph/Summer12_DR53X-PU_RD1_START53_V7N-v1/AODSIM	0.05795
/WZZNoGstarJets_8TeV-madgraph/Summer12_DR53X-PU_RD1_START53_V7N-v1/AODSIM	0.01968
/ZZZNoGstarJets_8TeV-madgraph/Summer12_DR53X-PU_RD1_START53_V7N-v1/AODSIM	0.005527
/WZA_8TeV_CMSSW532_LHE2EDM/jfaulkne-WZA_lvjja_8TeV_CMSSW532_RECO-c8f8ed334db8a7d6f56c62266b1dfa5b/USER	0.0121

**Table 6.2:** List of Monte Carlo  $W\gamma\gamma$  signal and backgrounds samples. The table gives the CMS Data Aggregation Service (DAS) name and the sample's full cross section.

neutrino, and photon mass ( $M_{\ell\nu\gamma'}$ ), where  $\gamma'$  is the photon nearest to the lepton. The divide is set at approximately twice the  $W$  mass, 165 GeV ( See Equation 6.1). Separate ISR and FSR events are shown in Figure 6.1.

$$\text{ISR Enriched: } M_{\ell\nu} + M_{\ell\nu\gamma'} > 165\text{GeV} \tag{6.1}$$

$$\text{FSR Enriched: } M_{\ell\nu} + M_{\ell\nu\gamma'} < 165\text{GeV}$$

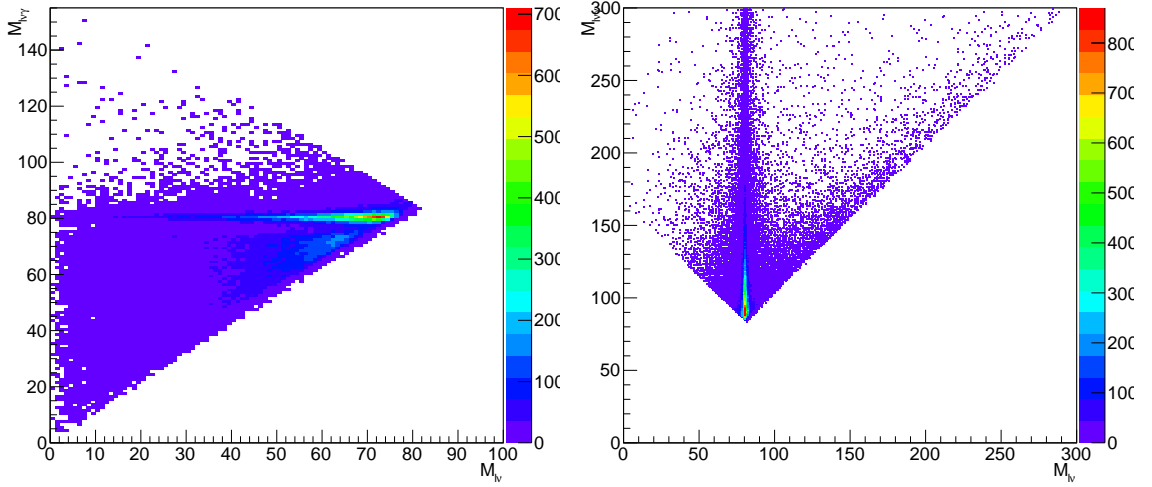


**Figure 6.1:** Separation of the FSR (left) and ISR (right) enriched samples discriminated with  $M_{\ell\nu} + M_{\ell\nu\gamma'}$ , where  $\gamma'$  is the photon closest to the lepton. Because adding an additional particle never decreases the total mass of the system, the region  $M_{\ell\nu\gamma'} < M_{\ell\nu}$  is empty.

A review of the principles of Event Simulation are covered in Chapter 5. For the NLO  $W\gamma\gamma$  samples specifically, the matrix element calculation is done with MADGRAPH interfaced with AMC@NLO [32]. The PDF set used is NNPDF and the physics model has a 5-flavor quark scheme that includes massless b quarks [33]. To account for smearing during reconstruction, events are generated in a phase-space

Dimension-8 Theory	Coupling Strength Range	Step Size	Generated Events
$L_{T,0}$ & $L_{T,1}$ & $L_{T,2}$	$-50 \times 10^{-12} : 50 \times 10^{-12}$	$5 \times 10^{-12}$	119,875
$L_{M,0}$ & $L_{M,1}$	$-5000 \times 10^{-12} : 5000 \times 10^{-12}$	$500 \times 10^{-12}$	120,665
$L_{M,2}$ & $L_{M,3}$	$-1000 \times 10^{-12} : 1000 \times 10^{-12}$	$100 \times 10^{-12}$	120,665

**Table 6.3:** The range and step sizes for Anomalous Quartic Couplings generated. Produced using the MadGraph Reweighting tool.

that is looser than the fiducial region. In the generated sample, jets are required to have  $p_T > 10$  GeV and photons must have  $p_T > 10$  GeV and  $|\eta| < 3.0$ . To avoid mathematical divergences in the matrix element calculation from collinear photons, a Frixione Isolation cut removes photons near other particles [34]. For photons within  $\Delta R < 0.05$  of a hadron or lepton, the cut requires:

$$\sum_i E_T^i \Theta(\delta - \Delta R_{i\gamma}) \leq E_T^\gamma \left( \frac{1 - \cos \delta}{1 - \cos \delta_0} \right) \quad (6.2)$$

Parton showering, final state radiation, and hadronization is handled by PYTHIA8 using the CUETP8M1 Tune [25]. The full CMS detector simulation and Reconstruction are done with *CMSSW\_5.3.X*.

A list of the signal samples and their cross sections can be found at the top of Table 6.2.

### 6.1.2.2 aQGC Samples

In addition to the SM  $W\gamma\gamma$  events, simulated datasets are produced for the dimension-8 EFTs. The datasets are produced at LO making use of the MADGRAPH reweighting tool (Section 5.3). Two MADGRAPH UFO files model the  $L_{T012}$  and  $L_{M0123}$  aQGC theories (See 2.4.1). Reweightings are generated over a range of

coupling strengths in standard step sizes. Additional reweightings are calculated around 0. Coupling range, step size, and the number of generated events are listed in Table 6.3.

### 6.1.2.3 Background Samples

Simulated samples are also used for background estimations. (Listed in Table 6.2). Simulated samples were originally also studied for the jet misidentification and electron misidentification rate. However, in control regions the MC was found to be a poor match to data. These background estimations were instead done with data driven methods.

### 6.1.2.4 Corrections to Monte Carlo

Simulated events are normalized to the integrated luminosity by applying a weight,

$$w = \frac{\sigma L}{N} \tag{6.3}$$

where  $\sigma$  is the sample's full cross section and  $N$  is the total number of simulated events. For NLO samples, events have positive and negative weights.  $N$  is the sum of weights ( $\sum w$ ).

To correct for differences between observed data and simulation, additional weights called scale factors are applied to the events. Scale factors are applied for the electron and muon trigger efficiency, photon identification, muon isolation, muon and electron identification, and for the Photon Electron Veto.



Pile-up reweighting weights are also applied to normalize the distribution of pile-up in MC to the CMS luminosity based measurements.

For the  $W\gamma\gamma$  signal samples, corrections are also made to the generator level information to account for the slight difference between the electron and muon channel. Following the procedure described in Section 5.4 generator level electrons and muons are dressed.

## 6.2 Object and Event Selection

### 6.2.1 Muon Selection

Selected muons are required to pass the Run1 Tight Muon ID. The Tight ID requires that candidate muons are reconstructed as both Global and Particle-Flow muons. To further suppress the presence of hadronic punch-through and decay in flight muons, the candidate muon is required to have a Global Track fit with  $\chi^2 < 10$ , at least one muon chamber must be part of the Global Track, the reconstructed muon must be matched to at least two muon stations, and there must be at least one pixel hit in the inner track.

To avoid selecting cosmic muons or decays in flight, Tight muons are also matched to the primary vertex. The reconstructed muon's transverse impact parameter ( $d_{xy}$ ) must be  $< 2$  mm from primary vertex and the longitudinal distance ( $d_z$ ) must be within 5 mm.

Lastly, to ensure accurate measurement of  $p_T$ , at least 5 layers in the Inner Tracker must have hits.

Selected muons are also required to be isolated. The analysis uses a Particle-Flow based, relative isolation parameter

$$\text{RelIso}_{\text{PF}} = \frac{I_{CH} + \max(0, I_N H + I_\gamma - \Delta\beta \cdot I_{CH-PU})}{p_T^\mu} \quad (6.4)$$

Within a  $\Delta R = 0.4$ . A  $\Delta\beta$  factor of 0.5 is used to infer the neutral pileup energy from the charged hadron pileup. To be selected, the  $\text{RelIso}_{\text{PF}}$  must be less than 0.12.

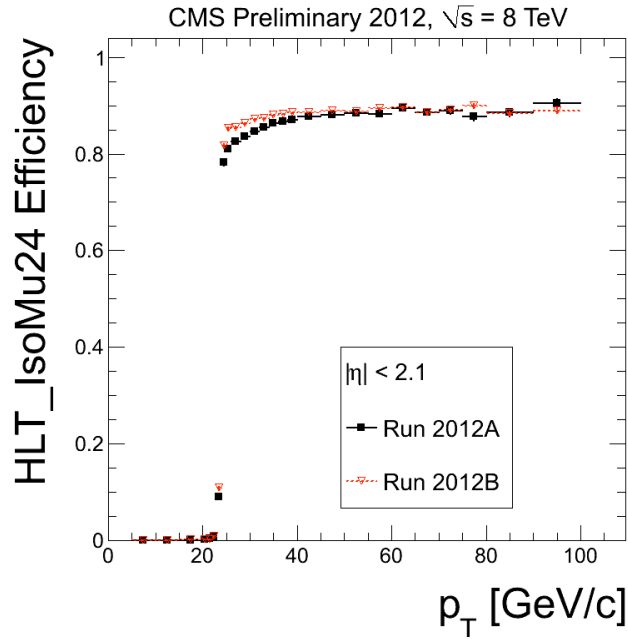


**Figure 6.2:** Efficiency of the HLT\_IsoMu24 trigger with respect to the off-line reconstructed muons. The selected muon's  $p_T$  threshold is 25 GeV, just where the efficiency starts to flatten.

Kinematic requirements are also made on the muon. To be above the turn-on threshold of the trigger (See Figure 6.2), the reconstructed  $p_T$  must be above 25 GeV. For pseudorapidity,  $|\eta| < 2.1$ .

## 6.2.2 Electron Selection

Selected electrons are required to pass a multivariate (MVA) ID, that is distinct from the MVA classifier used in electron reconstruction. The cut values on the MVA discriminate are tuned by the electron's  $|\eta|$ . In addition, there cannot be more than one missed hit on the track and a conversion veto is applied.

Selected electrons have their own isolation requirement. Again, a relative particle-flow based parameter is used:

$$\frac{\sum_{\Delta R < 0.4} p_T^{\text{PF}}}{p_T^e} \quad (6.5)$$

where the numerator is the sum of  $p_T$  for particle flow objects within a  $\Delta R$  cut of 0.4 and the denominator is the  $p_T$  of the electron. Corrections are made for the effects of pileup. To be selected electron must have a relative isolation parameter  $< 0.15$ ,

For the kinematic cuts, the electron trigger has a higher transition so the reconstructed  $p_T$  is required to be greater than 30 GeV. The  $|\eta|$  must be  $< 2.4$ .

## 6.2.3 Photon Selection

Photons are selected with the Medium Photon ID. These are Particle Flow photons, plus additional criteria based on the  $H \rightarrow \gamma\gamma$  measurement. The ratio of energy deposited in the HCAL to energy deposited in the ECAL,  $\frac{H}{E}$  must be less than 0.05. In the barrel and (endcap) the  $\sigma_{\eta\eta}$  value must be less than 0.011 (0.033). There are also photon isolation requirements: charge hadron isolation  $< 1.5$  (1.2), neutral hadron isolation  $< 1.0(1.5) + 0.04 \cdot p_T$ , and photon isolation  $< 0.7(1.0) + 0.005 \cdot p_T$ .

The efficiency of the Medium photon ID is 80% in the barrel and 75% in the endcap.

The kinematic selection cuts on the photon are a  $p_T$  greater than 25 GeV and  $|\eta| < 2.5$  GeV. The value of the photon  $p_T$  threshold was chosen to minimize the background from jets misidentified as photons.

#### 6.2.4 Overlap Removal

The same object can sometimes also be reconstructed as both a muon and an electron. If an electron is within  $\Delta R(e, \mu) < 0.4$ , the electron is removed from the analysis. Further, if a photon is reconstructed in the same location as a lepton  $\Delta R(\ell, \gamma) < 0.4$ , the photon is removed.

#### 6.2.5 Event Selection

Events are separated into three categories depending on the detector region in which the lead  $p_T$  and sub-lead  $p_T$  photons are reconstructed: both photons in the barrel (EBEB), lead in the barrel and sub-lead in the endcap (EBEE), and lead in the endcap and sublead in the barrel (EEEEB). Photon reconstruction is more accurate in the barrel than the endcap, and events without at least one photon in the barrel (EEEE) are not selected.

Selected events are required to have exactly one lepton and two photons passing the object selection criteria. To suppress backgrounds from processes producing a pair of leptons, ie  $Z\gamma\gamma$ , events containing a second lepton with  $p_T$  as low as 10 GeV are vetoed.

The selected objects in an events are also required to be spatially separated.  $\Delta R$  cuts on the lead and sub-lead photon,  $\Delta R(\gamma_1, \gamma_2) > 0.4$ , and between the lepton and photons,  $\Delta R(\ell, \gamma) > 0.4$ , are made. These cuts also ensures that the phase space of selected events does not include regions with collinear divergences in the matrix element calculation.

To select events consistent with leptonic  $W$  decay, a transverse mass variable is used. This variable is a handle on the mass of particles with invisible decay products, i.e. neutrinos and rejects backgrounds that have no  $\cancel{E}_T$ .  $M_T$  is defined as:

$$M_T = \sqrt{(E_{T,1} + E_{T,2})^2 - (p_{T,1}^{\vec{}} + p_{T,2}^{\vec{}})^2} \quad (6.6)$$

where the transverse energy is  $E_T = m^2 + p_T^2$ . For  $W$  decay to lepton and neutrino, we can approximate the electron and muon as massless, and assume the neutrino  $E_T$  equals the detector  $\cancel{E}_T$ . The equation for  $M_T$  simplifies to:

$$M_T(\ell, \cancel{E}_T) = \sqrt{2 \cdot E_\ell \cancel{E}_T \cdot (1 - \cos(\Delta\phi(\ell, \cancel{E}_T)))} \quad (6.7)$$

where  $\phi$  is the azimuthal angle between the lepton and the  $\cancel{E}_T$  in the transverse plane. Since the signal region is for  $W$  decays, the  $M_T(\ell, \cancel{E}_T)$  is required to be greater than 40 GeV.

To reduce backgrounds that are unique to the electron channel, an extra set of cuts are applied to electron events. One of the dominant electron backgrounds comes from  $Z \rightarrow ee$  decays, where one of the electrons is misidentified as a photon. To reduce its contribution, a Pixel Seed Electron Veto is introduced (See Section

4.4). In addition, mass cuts around the  $Z$  mass window for two and three body masses of electron-photon pairings are also made:  $86.2 \text{ GeV} < M_{e\gamma\gamma} < 96.2 \text{ GeV}$  and  $86.2 \text{ GeV} < M_{e\gamma\gamma} < 96.2 \text{ GeV}$ .

## 6.3 Background Estimation

Backgrounds are estimated with a combination of simulation and data driven methods. The main backgrounds are jets misidentified as photons, electrons misidentified as photons, and  $Z\gamma\gamma$  events.

### 6.3.1 Jets Faking Photons

High energy jets produce neutral pions ( $\pi^0$ ) that decay to photon pairs. When the  $\pi^0$  is sufficiently boosted, the pair of photons will overlap and can sometimes be reconstructed as a single photon. The off-line photon reconstruction and the analysis selection criteria are designed to reject these types of fakes. However, the  $W$ + jets and  $W\gamma$  + jets cross sections are several orders of magnitude larger than  $W\gamma\gamma$  cross section, resulting in a significant number of misidentified jet bleeding into the signal region.

The jet misidentification estimate is calculated using a two dimensional template method. Charged Hadron Isolation acts as a discriminating variable and separates the lead and sub-lead photon into tight (T) and loose (L) regions. Having both photons tight (TT) corresponds to the signal region and the other three pairings define the sideband regions.

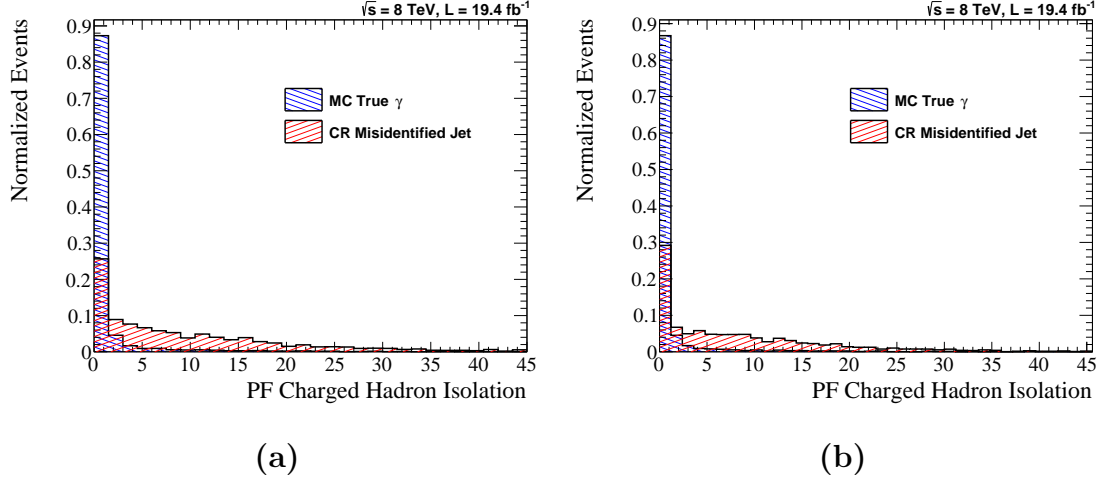


**Figure 6.3:** Shows a comparison of the real and fake photon templates as a function of charge hadron isolation. First bin corresponds to the tight region. On the left is the barrel region of the detector and on the right in the endcap. Figures are made for photons with  $p_T$  between 25-40 GeV.

The efficiency for real photon and fake photons to be reconstructed in the tight or loose regions comes from templates. A MC sample of  $W\gamma$  events is used for the real template. A data sample of  $Z + \text{jet}$  events with the real photon component subtracted via a  $Z\gamma$  MC sample accounts for the fake template. A special template is produced for events where both photons are misidentified jets. The fake-fake template is produced using a sideband region of events that fail to pass a  $\sigma_{\eta\eta}$  cut. To account for the reconstruction differences between the barrel and endcap, unique templates are made for the two detector regions and for different  $p_T$  ranges of the reconstructed photons (See Figure 6.3).

There are four possible cases for the lead and sub-leading photons: both photons are real (RR), the lead photon is real and the sub-lead is fake (RF), the lead is fake and the sub-lead is real (FR), or both are fake (FF). Efficiencies for each of these cases to fall within the signal or sideband regions are calculated. I.e.  $\epsilon_{FF}^{TL}$

represents the efficiency for an event with a fake lead and fake sub-leading photon to have the leading photon fall in the tight region and the sub-leading photon in the loose region. There are 16 efficiencies. With the exception of the correlated fake-fake processes, efficiencies are the product of their single object efficiencies. Real photons are rarely located in the loose region and these efficiencies can be approximated as zero.

With the efficiency matrix, the fake and real photons normalizations ( $\alpha$ ), can be related to the number of events in the four tight-loose regions ( $N$ ).

$$\begin{pmatrix} N_{TT} \\ N_{TL} \\ N_{LT} \\ N_{LL} \end{pmatrix} = \begin{pmatrix} \epsilon_{RR}^{TT} & \epsilon_{RF}^{TT} & \epsilon_{FR}^{TT} & \epsilon_{FF}^{TT} \\ \epsilon_{RR}^{TL} & \epsilon_{RF}^{TL} & \epsilon_{FR}^{TL} & \epsilon_{FF}^{TL} \\ \epsilon_{RR}^{LT} & \epsilon_{RF}^{LT} & \epsilon_{FR}^{LT} & \epsilon_{FF}^{LT} \\ \epsilon_{RR}^{LL} & \epsilon_{RF}^{LL} & \epsilon_{FR}^{LL} & \epsilon_{FF}^{LL} \end{pmatrix} \begin{pmatrix} \alpha_{RR} \\ \alpha_{RF} \\ \alpha_{FR} \\ \alpha_{FF} \end{pmatrix} \quad (6.8)$$

Inverting the efficiency matrix, one can calculate  $\alpha$  from the observed  $N$ , and solve for the jet misidentification background,

$$N_{bgd} = \epsilon_{RF}^{TT} \cdot \alpha_{RF} + \epsilon_{FR}^{TT} \cdot \alpha_{FR} + \epsilon_{FF}^{TT} \cdot \alpha_{FF} \quad (6.9)$$

In some cases, especially for large lead photon  $p_T$ , there are too few events in the sideband region to make an accurate jet fake estimate. In this scenario, a loosening procedure is used, and jet fakes estimates are made using photons on which the  $\sigma_{\eta\eta}$  constraint has been relaxed.

When initially testing this method of jet fake estimation, we kept ourselves



blind to the signal region.

### 6.3.2 Electrons Faking Photons

Important to the electron channel, electrons may be misidentified as photons. The electron fake background is estimated with another data driven method. A fake factor ( $ff$ ) is defined as the ratio of electron fakes that pass the Pixel Seed Electron Veto to those that fail. The  $ff$  is calculated in a control region expected to be mainly electron fakes; events with a reconstructed electron and photon at the two-body mass of the  $Z$ . Unique fake factors are measured for the lead and subleading  $p_T$  photons for each of the two photon detector regions. The electron misidentification background is calculated as the fake factor multiplied by the number of observed events in a sideband region passing all the analysis cuts except the PSEV. The sideband region includes a non-negligible number of events from jet fakes. The misidentified jets in the sideband is estimated using the procedure described in Section 6.3.1 and is subtracted off before estimating the electron fake background.

$$N_{\text{e bkgd}}^{SR} = ff(\eta^\gamma \eta^\gamma, p_T^\gamma) \cdot (N_{\text{obs}}^{SB} - N_{\text{jet bkgd}}^{SB}) \quad (6.10)$$

### 6.3.3 $Z\gamma\gamma$ Background

The next most important background is  $Z\gamma\gamma$ . It is a multiboson process similar to  $W\gamma\gamma$ , and it can mimic the  $W\gamma\gamma$  signal when the second  $Z$ -decay lepton fails to pass the electron or muon selection criteria. The  $Z\gamma\gamma$  background is modeled with

NLO simulation. To avoid double counting fakes, the selected photons are truth matched to generator level photons.

### 6.3.4 Other Diphoton Backgrounds

In addition to  $Z\gamma\gamma$ , other two photon final states have a small probability of entering the signal region:  $WW\gamma\gamma$ ,  $WZ\gamma\gamma$ ,  $ZZ\gamma\gamma$ , and  $t\bar{t}\gamma\gamma$ . The contribution of these processes is also modeled with simulation. The  $t\bar{t}$  process is normalized to the NNLO cross-section prediction, and the other multiboson processes are normalized to NLO. Only a fractional number of such events are expected.

### 6.3.5 Negligible Backgrounds

This section briefly describes other backgrounds that were considered, but the contributions of which were negligible. Jets can potentially be misidentified as electrons. The process sourcing such events is rare because of the small cross section of real diphoton events and further suppressed by the low fake rates of the MVA Electron and Tight Muon IDs. Another potential background is multiple proton collisions during a single bunch crossing. Because photons are not associated with a vertex, the second collision would not be distinguishable. Estimates for the probability of  $W\gamma$  and  $\gamma$  double hard scatter events found the background to be less than 1% of the expected signal.

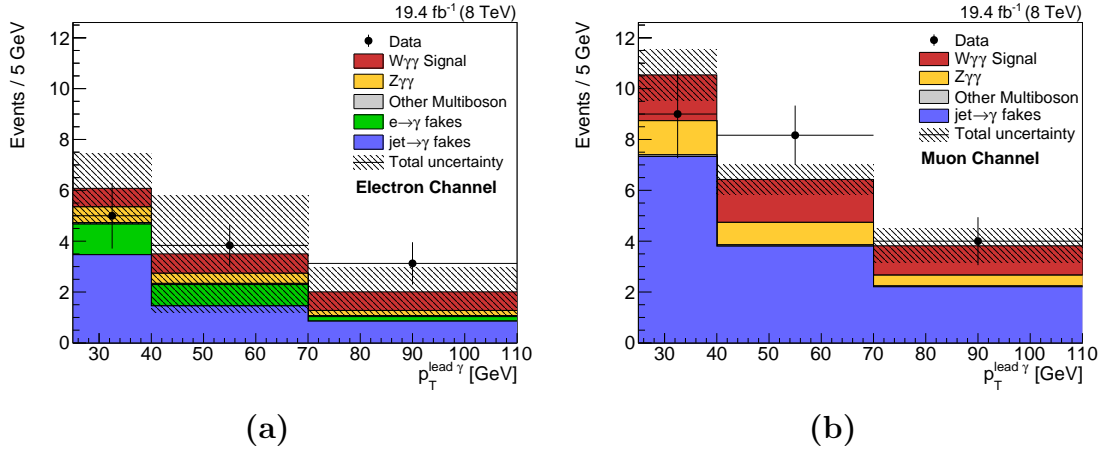


**Figure 6.4:** Lead photon  $p_T$  distribution for the electron and muon channel. Shows the data, expected  $W\gamma\gamma$  signal, as well as estimates for the jet misidentification, electron misidentification, and other di-photon backgrounds.

## 6.4 Summary of Signal and Background

This section summarizes the results of the selected data, expected signal, and estimated backgrounds. Figure 6.4 shows a comparison of data to the expected events as a function of lead photon  $p_T$ . Table 6.4 has the backgrounds broken down between jet misidentification, electron misidentification, and  $Z\gamma\gamma$  + diphoton backgrounds.

## 6.5 Fiducial Cross Section

The fiducial cross section is calculated using the formula:

$$\sigma(pp \rightarrow l\nu\gamma\gamma)_{\text{Fiducial}} = (1 - f_\tau) \cdot \frac{N_{\text{obs}} - N_{\text{bkgd}}}{C_{W\gamma\gamma} \cdot \mathcal{L}}, \quad (6.11)$$

Where  $N_{\text{obs}}$  is the number of observed events,  $N_{\text{bkgd}}$  is the estimated background,  $C_{W\gamma\gamma}$  is the fiducial acceptance factor,  $f_\tau$  is the fraction of  $\tau$  events, and  $\mathcal{L}$  is the

Region	jet misID	e misID	$Z\gamma\gamma$ + Diphoton	Total Background	Data	Expected signal
Muon Channel						
Barrel-Barrel	$25 \pm 6$	–	$9 \pm 1$	$34 \pm 6$	62	$16.5 \pm 1.8$
Barrel-Endcap	$17 \pm 3$	–	$1.8 \pm 0.4$	$19 \pm 3$	26	$4.1 \pm 0.5$
Endcap-Barrel	$21 \pm 4$	–	$2.4 \pm 0.4$	$24 \pm 4$	20	$4.1 \pm 0.5$
Sum	$63 \pm 11$	–	$13 \pm 2$	$77 \pm 11$	108	$25 \pm 3$
Electron Channel						
Barrel-Barrel	$14 \pm 4$	$5 \pm 6$	$4.7 \pm 0.6$	$24 \pm 4$	37	$9 \pm 1$
Barrel-Endcap	$6 \pm 1$	$3 \pm 3$	$1.1 \pm 0.3$	$10 \pm 2$	15	$2.0 \pm 0.2$
Endcap-Barrel	$6 \pm 1$	$0 \pm 2$	$0.8 \pm 0.2$	$7 \pm 2$	11	$2.0 \pm 0.2$
Sum	$26 \pm 4$	$8 \pm 7$	$6.6 \pm 0.8$	$41 \pm 5$	63	$13 \pm 1$

**Table 6.4:** Summary table of the background estimates, the expected  $W\gamma\gamma$  signal, and the number of observed events in the data. Estimates are broken up between the different regions of the detector. The expected number of signal and background events are normalized to the integrated luminosity for the data sample collected,  $19.4 \text{ fb}^{-1}$ .

integrated luminosity.

### 6.5.1 Definition of Fiducial Region

Definition of $W\gamma\gamma$ Fiducial Region
$p_T^\gamma > 25\text{GeV},  \eta^\gamma  < 2.5$
$p_T^\ell > 25\text{GeV},  \eta^\ell  < 2.4$
Exactly one candidate lepton and two candidate photons
$M_T > 40\text{GeV}$
$\Delta R(\gamma, \gamma) > 0.4$ and $\Delta R(\gamma, \ell) > 0.4$

**Table 6.5:** Definition of the Fiducial Region used for the  $W\gamma\gamma$  Cross-Section measurements.  $M_T$  is the transverse mass of the Candidate Lepton and Neutrino(s).

For a fiducial cross-section measurement, a fiducial region must be defined. The fiducial cuts are made at the generator level using the simulated NLO signal events. The generator leptons have been dressed following the procedure described in Section 5.4.

The fiducial region is well defined, so that divergences in the theoretical cross

section because of low photon  $p_T$  or small photon-lepton separations are avoided. As closely as possible, the fiducial region matches the off-line selection requirements described in Section 6.2. The definition of  $W\gamma\gamma$  fiducial region is given in Table 6.5.

Fiducial Cuts	Electron Channel	Muon Channel
Exactly 1 Candidate Lepton	$3533.5 \pm 10.1$	$3600.3 \pm 10.1$
Exactly 2 Candidate Photons	$225.5 \pm 2.0$	$225.2 \pm 2.0$
$\Delta R(\text{photon, photon}) > 0.4$	$212.4 \pm 1.9$	$211.3 \pm 1.9$
$\Delta R(\text{photon, lepton}) > 0.4$	$127.8 \pm 1.2$	$129.5 \pm 1.2$
$M_T(\text{lepton, neutrino(s)}) > 40$	$94.6 \pm 1.0$	$95.2 \pm 1.0$

**Table 6.6:** Fiducial Cut Flow for the  $W\gamma\gamma$  signal. Weighted combination of ISR and FSR samples normalized to the  $19.4 \text{ fb}^{-1}$  luminosity.

The fiducial definition is mainly kinematic cuts on a particle’s  $p_T$  and  $\eta$  or event cuts on particle multiplicity,  $\Delta R$ , and  $M_T$ . To select true  $W\gamma\gamma$  events the generator parentage information was utilized. To ensure that leptons and photons were from the hard-scatter, the parentage was recursively checked to make sure the particles were not from jet decays. Since MADGRAPH assigns the initial parton as the parent of an off-shell  $W$  decay, leptons were required to have a parent ID, matching a  $W$ ,  $\tau$ , quark, or gluon. Further, parentage was used to confirm that the lepton came directly from the  $W$  or via an intermediate  $W \rightarrow \tau$  decay. Table 6.6 shows the cut-flow for the fiducial definition and the expected number of events within the fiducial region.

## 6.5.2 Fiducial Acceptance

Acceptances are the ratio of reconstructed events passing the selection criteria to the generator events within the fiducial region. They are calculated from

simulation.

$$C_{W\gamma\gamma} = \frac{N_{reco}[W \rightarrow \ell\nu\gamma\gamma] + N_{reco}[W \rightarrow \tau\nu\gamma\gamma \rightarrow \ell\nu\nu\gamma\gamma]}{N_{gen}[W \rightarrow \ell\nu\gamma\gamma(\text{fiducial})] + N_{gen}[W \rightarrow \tau\nu\gamma\gamma \rightarrow \ell\nu\nu\gamma\gamma(\text{fiducial})]} \quad (6.12)$$

The Acceptance accounts for the detector reconstruction efficiency as well as extrapolates over regions within the fiducial definition but outside the selection cuts. This includes the gap between the barrel and endcap, as well as extrapolations to lower electron  $p_T$ , to higher muon  $\eta$ , and over the phase-space of events where both photons are reconstructed in the endcap.

### 6.5.3 $\tau$ Subtraction

The  $pp \rightarrow \ell\nu\nu\gamma\gamma$  final state produced by a  $W$  decaying through a  $\tau$  is a distinct physical process from  $W$  decaying directly to an electron or muon. The  $\tau$  decays are treated as a background. Since the number of  $\tau$  events is estimated using the signal samples, its removal is best treated as part of the acceptance. Within the fiducial region,  $f_\tau$  is small because of the  $\tau$  branching fraction and because leptons from  $\tau$  decays are softer and more affected by the lepton  $p_T$  and  $M_T$  cuts.  $f_\tau$  is 2.2% for the electron channel and 2.5% for the muon channel.

$$f_\tau = \frac{N_{gen}[W \rightarrow \tau\nu\gamma\gamma \rightarrow \ell\nu\nu\gamma\gamma(\text{fiducial})]}{N_{gen}[W \rightarrow \ell\nu\gamma\gamma(\text{fiducial})] + N_{gen}[W \rightarrow \tau\nu\gamma\gamma \rightarrow \ell\nu\nu\gamma\gamma(\text{fiducial})]} \quad (6.13)$$

To calculate the cross section, the combined quantity  $\frac{C_{W\gamma\gamma}}{1-f_r}$  is used. This quantity is observed to increase with lead photon  $p_T$  (See Table 6.7), however only the total fiducial acceptance factor (lead photon  $p_T > 25$  GeV) is used in the cross section calculation.

Lead Photon $p_T$	Electron Channel	Muon Channel
25-40	$14.57 \pm 1.04 \pm_{-0.62}^{+0.65}$	$25.10 \pm 1.39 \pm_{-0.63}^{+0.63}$
40-70	$16.31 \pm 0.74 \pm_{-0.88}^{+0.88}$	$26.76 \pm 1.05 \pm_{-0.72}^{+0.72}$
70+	$19.95 \pm 0.78 \pm_{-1.03}^{+1.04}$	$27.62 \pm 0.94 \pm_{-0.77}^{+0.78}$
Total	$17.25 \pm 0.48 \pm_{-0.69}^{+0.70}$	$26.69 \pm 0.64 \pm_{-0.68}^{+0.68}$

**Table 6.7:**  $\frac{C_{W\gamma\gamma}}{1-f_r}$  as function of Lead Photon  $p_T$  with statistical and systematic errors. "Total" is the  $\frac{C_{W\gamma\gamma}}{1-f_r}$  for all events with lead photon  $p_T$  above 25 GeV

## 6.6 Selection for aQGC Study

For the anomalous quartic gauge couplings, a modified search strategy is employed. SM events that were signal for the cross-section measurement become an additional background. In the dimension-8 EFT models, deviations from SM occur at high photon  $p_T$ . We use the same object requirements and backgrounds estimation methods described earlier in this method, but the event selection is redefined to require a lead photon with  $p_T$  above 70 GeV. As with the cross section measurement, the analysis is broken up by the detector region of the two photons.

The aQGC samples are produced at LO, while the  $W\gamma\gamma$  signal sample is generated at NLO. The aQGC samples with an anomalous coupling strength of zero are normalized to the  $W\gamma\gamma$  signal sample, introducing an effective k-factor. A separate k-factor is calculated for each of the detector region categories. The events

are then re-weighted, to the desired coupling strength. Figure 6.5 shows the ratio of aQGC to SM yields as a function of the coupling strength.

Under the assumption that the energy reach of the analysis does not violate unitarity, no form factor is applied to the aQGC models. Using VBFNLO, this assumption is confirmed by checking the vertex energy at which unitarity is violated [35]. Values for the unitarity bounds are given in Appendix A.1. A negligible number of events are predicted above these energies.



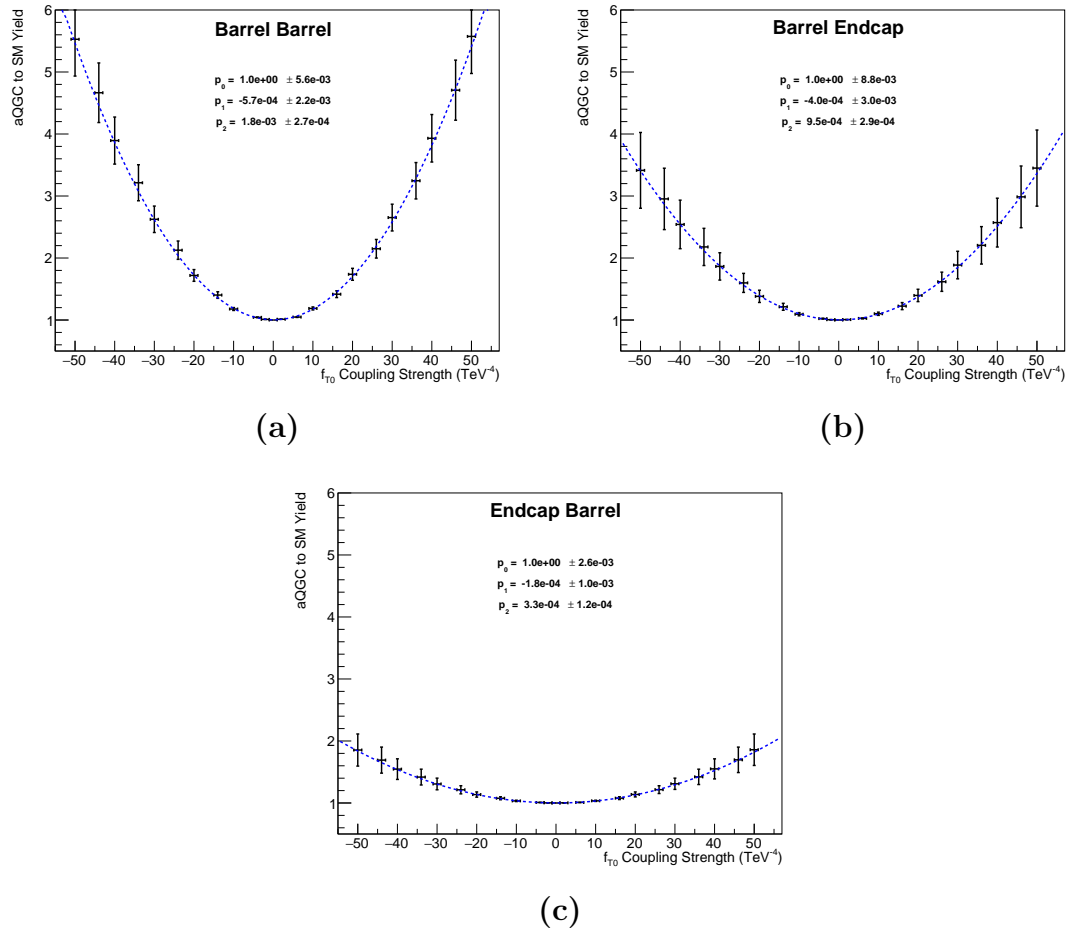


**Figure 6.5:** aQGC to SM yields for the LT0 dim-8 theory. Ratios are calculated using reconstructed muon events with a lead photon  $p_T > 70$  GeV. The three plots show the three separate  $\eta\gamma\eta\gamma$  classifications: (a) Barrel Barrel, (b) Barrel EndCap, and (c) EndCap Barrel. Limit setting power comes mainly from the Barrel Barrel events. Correlations between the samples caused by the reweighting procedure are accounted for when calculating the error bars and the fit.

## Chapter 7

### Statistical and Systematic Uncertainties

This chapter describes the statistical and systematic uncertainties affecting the analysis. A list of the systematics and their impact on the electron and muon channels cross section is given in Table 7.1. A list of signal systematics and their impact on the aQGC limit setting bins are given in Table 7.2.

#### 7.1 Statistical Uncertainties

For a random process, the possible outcomes are described by a probability distribution. The spread of the distribution represents a statistical uncertainty. For counting experiments, the number of observed events ( $N$ ) follows a Poisson distribution and has a standard deviation equal to  $\sqrt{N}$ . Counted events in the signal region and the sideband regions are sources of statistical uncertainty. The electron channel has additional sidebands because of the electron misidentification estimate. As a result, the electron channel has larger sideband statistical uncertainties (See Table 7.1).

To calculate the impact on the cross-section measurement, statistical errors are propagated. The effect is not always direct. A single source can impact multiple variables in the cross section formula (Equation 6.11). For example, the uncertainty on the number of signal region events affects  $N_{\text{obs}}$ , but also affects the jet fake

**Table 7.1:** Systematic and statistical uncertainties effecting the  $W\gamma\gamma$  fiducial cross section measurement in the electron and muon channels.

Systematic	$W\gamma\gamma \rightarrow e\gamma\gamma$	$W\gamma\gamma \rightarrow \mu\gamma\gamma$
Acceptance and Tau Fraction Systematics	$\delta(\sigma_{W\gamma\gamma})$	
MC Statistics	2.78%	2.40%
Trigger	0.46%	0.26%
Photon Identification	2.06%	2.04%
Muon Identification and Isolation		0.27%
Electron MVA Identification	0.12%	
Photon Pixel Seed Electron Veto	3.04%	
Photon and Electron Energy Scale	1.84%	2.10%
Muon Energy Scale	–	0.19%
$\cancel{E}_T$ Scale	1.52%	1.39%
PDF	1.25%	1.45%
Renormalization and Factorization	0.78%	0.77%
Pile-up	0.49%	0.17%
Total Acceptance and Tau Fraction	5.44%	4.38%
Background Systematics	$\delta(\sigma_{W\gamma\gamma})$	
Jets Misreconstructed	6.13%	35.24%
Electrons Misreconstred	4.09%	–
$Z\gamma\gamma$	3.44%	4.78%
Other Multiboson Backgrounds	1.18%	0.70%
Total Background	8.22%	35.57%
Statistical Uncertainties	$\delta(\sigma_{W\gamma\gamma})$	
Signal Region	27.65%	28.41%
Sidebands	20.72%	4.38%
Total Statistical	34.55%	28.75%

Systematics	Electron Channel			Muon Channel		
	(EBEB)	(EBEE)	(EEEB)	(EBEB)	(EBEE)	(EEEB)
MC Stats	4.0%	9.1%	11.1%	3.6%	7.4%	8.1%
Factorization	3.1%	3.5%	2.1%	2.8%	3.1%	3.1%
PDF	8.7%	9.6%	9.0%	7.7%	8.5%	8.1%
Pile-up	0.2%	0.3%	1.3%	1.1%	0.6%	1.7%
Renormalization	6.5%	6.1%	4.2%	6.5%	6.2%	5.3%
Scale Factor	3.4%	4.5%	4.5%	2.1%	2.1%	2.1%

**Table 7.2:** Systematic uncertainties on the expected number of  $W\gamma\gamma$  reconstructed events. These are for the events with lead photon  $p_T > 70$  GeV, separated between the electron and muon channel and by  $\eta^\gamma\eta^\gamma$ . These values are used as nuisance parameters in the aQGC limit setting.

estimate within  $N_{\text{bkgd}}$ . When propagating the error, the net effect on  $N_{\text{obs}} - N_{\text{bkgd}}$  is what must be considered. When propagating the error, the subtraction leads to cancellation and smaller net statistical errors.

A total statistical uncertainty on the cross section is quoted by summing the signal region and sideband region uncertainties in quadrature.

## 7.2 Signal Simulation Systematics

There are a number of systematics associated with the signal samples and they impact the calculation of the  $C_{W\gamma\gamma}$  and  $f_\tau$ . For any MC sample, there is an uncertainty due to the finite number of events generated. This is described by the Poisson of a weighted distribution,

$$\sigma^2 = \sum_i w_i^2 \tag{7.1}$$

There are also systematics associated with the event generator: renormalization, factorization, and the PDF. To calculate the renormalization and factorization systematics, events are reweighted for renormalization and factorization scales varied to  $\frac{1}{2}$  and 2 times their nominal values. For the PDF there are two systematics. One from the choice of the PDF set and the second from the set's error matrix. For the set systematic, three different PDF sets are compared, NNPDF-NLO, CT10-NLO, and MSTW-NLO. Events are reweighted by taking the ratio of the new

partons' distribution function to the original.

$$\frac{f(x, Q)_{1,\text{new}} \cdot f(x, Q)_{2,\text{new}}}{f(x, Q)_{1,\text{old}} \cdot f(x, Q)_{2,\text{old}}} \quad (7.2)$$

The systematic is taken as the standard deviation of the three sets. The error matrix is an  $N \times N$  matrix, where  $N$  is the number of variables used by the PDF to model the proton. When the matrix is diagonalized, there are  $N$  independent eigenvectors. For NNPDF-NLO, the set used in the event generation, there are 51 eigenvectors. Systematics are calculated using the ‘‘master equation’’ method described by Bourilkov et al. [36]. The upper and lower pdf error matrix systematic for a variable  $X^\pm$ , is defined as:

$$\begin{aligned} \Delta X^+ &= \sqrt{\sum_i^N \max(X_i^+ - X_0, X_i^- - X_0, 0)^2} \\ \Delta X^- &= \sqrt{\sum_i^N \min(X_i^+ - X_0, X_i^- - X_0, 0)^2} \end{aligned} \quad (7.3)$$

where  $X_0$  is the nominal value for the PDF's central value, and  $X_i^+$ ,  $X_i^-$  are the values for the  $i$ th eigenvector varied up or down.

There is a systematic for pile-up (PU). In the MC, pile-up is simulated by adding additional min-bias events to the hard-scatter. The distribution of pile-up in the data is found from a luminosity measurement based on pixel seed counting [37]. The MC is re-weighted, so that its distribution of PU matches the data [38]. For the systematic, the distribution of the number of PU vertices is varied 5% up

or down, and new reweightings are calculated.

As described in 6.1.2.4, scale factors are applied to account for the difference between data and MC. Official scale factors for the triggers, identification, and isolation are provided by the CMS Physics Objects Groups (POG). For the electron trigger and identification scale factors, the comparison of data to MC is done using a tag and probe method for  $Z \rightarrow ee$  decay. For the muon trigger, identification, and isolation scale factors a tag and probe method for the  $Z \rightarrow \mu\mu$  decay is used. Since electrons and photons deposit energy in the ECAL through similar mechanisms, the electron shower energy from a tag and probe of the  $Z \rightarrow ee$  decay is used to calculate the photon identification scale factor [19]. A custom scale factor is calculated for the Pixel Seed Electron Veto, using  $Z \rightarrow \mu\mu + \gamma_{\text{FSR}}$  events, where the dimuon plus photon mass are required to be within 10 GeV of the  $Z$  mass. The standard deviations in the value of the scale factors are calculated. By varying the scale factors  $1\sigma$  up and down the systematics are determined.

Estimates of the electron, muon, and photon energy scale uncertainty come from comparisons of the  $Z$  mass lineshape in data versus MC. Uncertainties on the MET energy scale are estimated by propagating the individual energy scale uncertainties for each object used in the MET calculation.

### 7.3 Background Systematics

Systematics are also associated with the background estimates. There are a range of systematics from the jet misidentification templates. For the real photon

template, the systematic is calculated by comparing efficiencies from simulation to those from data. Like the MC, the data sample comes from  $Z\gamma$  events, where the  $Z$  decays to a pair of muons and the selected photon is tagged as FSR.

In constructing the fake template, simulated  $Z+\gamma$  events are subtracted from  $Z+\text{jet}$  data. The  $Z+\gamma$  sample is normalized to the NLO cross section. To account for the theoretical uncertainties on the cross section, a 20% systematic is applied to the normalization. For the fake-fake template, a systematic is assigned corresponding to variations in the definition of the sideband region.

There is also a systematic for the loosening procedure. When the selection definition on one of the photons is changed, this effects the shape of the other photon's template. The size of the effect is approximated by selecting a diphoton region and modifying the selection criteria of one of the photons.

During error propagation, templates are used in both the jet misidentification estimate and in subtracting jets from the sideband region used for the electron misidentification estimate. The systematics impact on the two backgrounds are anti-correlated, leading to a partial cancelation of the effect on the cross section.

For the electron misidentification, there is a systematic on the electron fake factor. It comes from the choice of how the  $Z$ -peak in the data driven estimate was fit. The difference between the fit for a Breit-Weigner function vs a MC template is taken as the systematic.

As described, the  $Z\gamma\gamma$  background is modeled using simulation. There are two systematics, one associated with the finite statistics of the MC sample and a second 12.5% systematic applied to account for the theory uncertainty on the  $Z\gamma\gamma$

cross section. Likewise there are MC and theory systematics associated with the estimates of the other multiboson backgrounds.



## Chapter 8

### Results

This chapter presents the result of the  $W\gamma\gamma$  analysis. The selected events, background estimates, and fiducial acceptances described in Chapter 6 are interpreted as a combined cross-section measurement and as limits on anomalous quartic gauge couplings. The cross section results are compared to the theory expectation and the significance above the background only hypothesis is calculated.

#### 8.1 Combined Cross Section

Following Equation 6.11, cross sections are calculated for the electron and muon channels:  $\sigma_{W\gamma\gamma}^{\text{fid}} \cdot \text{BR}(W \rightarrow e\nu) = 6.6 \pm 2.3(\text{stat}) \pm 0.5(\text{syst}) \pm 0.2(\text{lumi})\text{fb}$  and  $\sigma_{W\gamma\gamma}^{\text{fid}} \cdot \text{BR}(W \rightarrow \mu\nu) = 6.0 \pm 1.8(\text{stat}) \pm 2.2(\text{syst}) \pm 0.2(\text{lumi})\text{fb}$ . By lepton universality, the two cross section are expected to be the same. To reduce uncertainties, the channels are combined into a single measurement of  $\sigma_{W\gamma\gamma}^{\text{fid}} \cdot \text{BR}(W \rightarrow \ell\nu)$ .

The combination is done using the Best Linear Unbiased Estimator (BLUE) method [39]. The BLUE method is a weighted average where the channel weights ( $\alpha_i$ ) are set so as to minimize the combined measurement's uncertainty. Given the result of each channel ( $y_i$ ), the BLUE combined result is defined as:

$$\hat{y}_i = \sum_i \alpha_i \cdot y_i \tag{8.1}$$

where weights are constrained such that  $\sum_i \alpha_i = 1$ . For the minimization, the combined uncertainty ( $\hat{\sigma}^2$ ) is defined in terms of an error matrix ( $\mathbf{E}$ ),

$$\hat{\sigma}^2 = \vec{\alpha}^T \cdot \mathbf{E} \cdot \vec{\alpha} \quad (8.2)$$

where  $\vec{\alpha}$  is a vector of weights and  $\vec{\alpha}^T$  is its transpose.

For the two channel case,  $\mathbf{E}$  is defined as:

$$\mathbf{E} = \begin{pmatrix} \sigma_{y1}^2 & \text{cov}(y_1, y_2) \\ \text{cov}(y_1, y_2) & \sigma_{y2}^2 \end{pmatrix} \quad (8.3)$$

where the standard deviations and covariances are defined using the statistical and systematic uncertainties detailed in Table 7.1. Between the two channels, statistical uncertainties are uncorrelated and systematics present in both are treated as fully correlated.

The combined  $W\gamma\gamma$  fiducial cross-section measurement for the electron and muon channels is:

$$\sigma_{W\gamma\gamma}^{\text{fid}} \cdot \text{BR}(W \rightarrow \ell\nu) = 6.4 \pm 1.3 \text{ (stat)} \pm 1.8 \text{ (syst)} \pm 0.2 \text{ (lumi)} \text{ fb.}$$

The result is compared to the NLO theory predicted cross section of the fiducial phase space. The theoretical cross section is a combined electron, muon result obtained from MADGRAPH generated events. Its uncertainties come from the limited simulation statistics, renormalization, factorization, and the PDF. The theory

value is consistent with the measured results.

$$\sigma_{W\gamma\gamma}^{\text{NLO}} \cdot \text{BR}(W \rightarrow \ell\nu) = 4.76 \pm 0.53\text{fb}$$

### 8.1.1 Significance

The statistical strength of the cross section measurement is quantified using a profile likelihood approach. (Likelihoods and likelihood ratios are described in detail in Section 8.2.) For the profile likelihood calculation, events are split between the two channels and the three detector region categories for a total of six bins. The ratio of likelihoods for the best fit to data compared to the background only hypothesis is interpreted as a significance. Calculations are implemented with the Higgs Combine tool [40]. The observed events correspond to a significance over the background only hypothesis of  $2.9 \sigma$ .

## 8.2 Limit Setting

A likelihood method is also used for defining a 95% confidence interval (CI) and setting upper-bounds on the dimension-8 EFT. Events with lead photon  $p_T > 70$  GeV are split into six bins corresponding to the two channels and the three detector region categories. Assuming the number of observed events follow a Poisson distribution, likelihood is defined as:

$$\mathcal{L}(f) = \prod_{i=1}^{n\text{bins}} \text{Pois}(x_i | \mu \cdot s_i(\theta) + b_i(\theta)) \times P_n(\theta) \quad (8.4)$$

where  $s_i$  is the expected signal events,  $b_i$  is the expected background, and  $P_n(\theta)$  accounts for the systematic uncertainties through nuisance parameters.

A test statistic,  $t_f$ , is defined as the negative log of the ratio of the likelihood for a specific coupling to the maximum likelihood.

$$t_f = -2 \ln \frac{L(f, \hat{\theta})}{L(\hat{f}, \hat{\theta})}, \quad (8.5)$$

where  $f$  is the anomalous coupling parameter,  $\hat{\theta}$  are the nuisance parameters maximizing likelihood for a single  $f$  value, and  $\hat{f}$  and  $\hat{\theta}$  are the coupling strength and nuisance parameters for the global maximum likelihood [40].

From Wilk's theorem,  $t_f$  behaves as a  $\chi^2$  distribution with one degree of freedom. The 95% confidence interval corresponds to couplings with  $t_f < 3.84$ .

Observed and expected log-likelihood ratios for the  $f_{T,0}$  coupling strengths are displayed in Figure 8.1. Coupling strengths with a  $t_f > 3.84$  are excluded. The small rise in the shape of the observed likelihood ratio is caused by an excess of events beyond the SM expectation. The excess is not statistically significant but causes the observed limits to be slightly weaker than the expected ones.

A summary of the combined limits on the dimension-8 EFT are displayed in Table 8.1. The  $W\gamma\gamma$  analysis is particularly sensitive to the  $f_{T,0}$  coupling, finding  $-35.9 < \frac{f_{T,0}}{\Lambda^4} < 36.7$ .

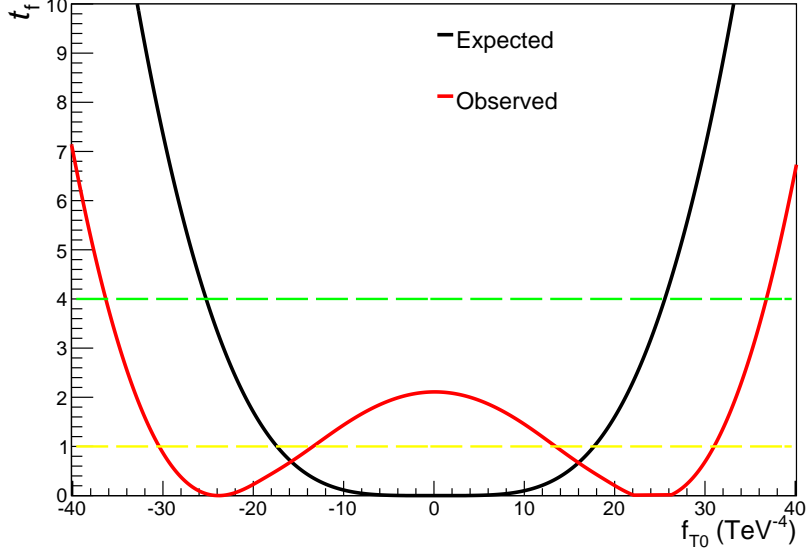


**Figure 8.1:** Test statistic,  $t_f$  (negative log likelihood ratio), value as a function of the  $f_{T,0}$  coupling strength. The expected distribution is marked in black and the observed distribution in red. The  $1\sigma$  and  $2\sigma$  exclusion levels are shown in yellow and green. The 95% confidence interval corresponds to coupling strength with a  $t_f < 3.84$ .

**Table 8.1:** 95% exclusion limits on the anomalous couplings for the combined electron and muon channels

Expected Limits ( $\text{TeV}^{-4}$ )	Observed Limits ( $\text{TeV}^{-4}$ )
$-24.9 < \frac{f_{T0}}{\Lambda^4} < 25.3$	$-35.9 < \frac{f_{T0}}{\Lambda^4} < 36.7$
$-33.1 < \frac{f_{T1}}{\Lambda^4} < 33.3$	$-46.3 < \frac{f_{T0}}{\Lambda^4} < 46.9$
$-71.0 < \frac{f_{T2}}{\Lambda^4} < 70.2$	$-99.8 < \frac{f_{T2}}{\Lambda^4} < 99.8$
$-521 < \frac{f_{M2}}{\Lambda^4} < 503$	$-741 < \frac{f_{M2}}{\Lambda^4} < 719$
$-863 < \frac{f_{M3}}{\Lambda^4} < 896$	$-1050 < \frac{f_{M3}}{\Lambda^4} < 1050$

**Table 8.2:** Comparison of the limits set on the  $f_{T,0}$  coupling for the ATLAS  $W\gamma\gamma$ , CMS  $W\gamma\gamma$  and CMS  $WV\gamma$  analyses.

Limits	ATLAS $W\gamma\gamma$	CMS $W\gamma\gamma$	CMS $WV\gamma$
Observed	$16 < \frac{f_{T0}}{\Lambda^4} < 16$	$-36 < \frac{f_{T0}}{\Lambda^4} < 37$	$-25 < \frac{f_{T0}}{\Lambda^4} < 24$
Expected	$22 < \frac{f_{T0}}{\Lambda^4} < 22$	$-25 < \frac{f_{T0}}{\Lambda^4} < 25$	$-27 < \frac{f_{T0}}{\Lambda^4} < 27$

### 8.3 Other Triboson Measurements

In addition to the the CMS  $W\gamma\gamma$  measurement, the ATLAS experiment also measured the  $W\gamma\gamma$  process, and both experiments have made measurements of other triboson processes.

The ATLAS and CMS  $W\gamma\gamma$  cross section cannot be directly compared because they correspond to two different fiducial regions. However, the ATLAS experiment also observes a result with a  $3\sigma$  significance, and their cross section deviates by  $1.9\sigma$  from the theoretically expected SM value [41].

CMS made a measurement of  $WV\gamma$  production ( $V$  is a  $W$  or  $Z$ ). The analysis was unable to measure a cross section and instead set an upper-bound that was a factor of 3.4 above the SM prediction [42].

The triboson analyses also set limits on the dimension-8 couplings. Table 8.2 shows a comparison of the expected and observed limits on the  $f_{T,0}$  parameter for this dissertation and for the ATLAS  $W\gamma\gamma$  and CMS  $WV\gamma$  analyses. For  $W\gamma\gamma$ , both ATLAS and CMS have comparable expected limits. The difference in the observed limits reflects a deficit of events observed by ATLAS compared to an excess observed by CMS.

## Chapter 9

### Extensions to $Z\gamma\gamma$

This Chapter discusses an extension of the methods use in the  $W\gamma\gamma$  analysis to a separate measurement of the  $Z\gamma\gamma$  cross section. For both analyses, NLO signal samples are produced with MADGRAPH generators, the jet misidentification estimates are made with a two dimensional template method, fiducial regions are defined for the cross section, a BLUE combination is made, and many of the systematics are shared. The cross section results, its significance, and a comparison with the SM expectation are presented.

#### 9.1 Feynman Diagrams

For  $Z\gamma\gamma$ , again the leptonic decays of the gauge bosons are studied  $pp \rightarrow \ell\bar{\ell}\gamma\gamma$ , where the leptons are a pair of same type electrons or muons. Contributing Feynman diagrams include a pair of photons produced through ISR or FSR. Example diagrams are shown in Figure 9.1. Not included are TGC or QGC modes of  $Z\gamma\gamma$  production, which are forbidden in the SM. Simulated  $Z\gamma\gamma$  events are produced at NLO using MADGRAPH.

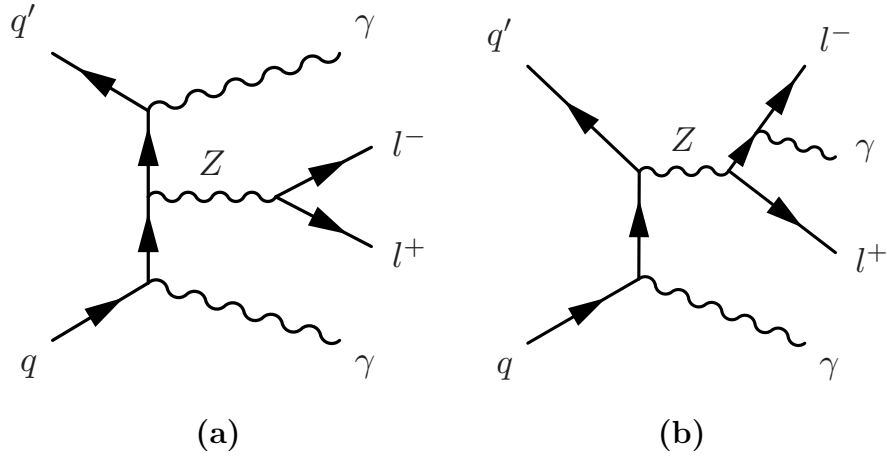


**Figure 9.1:** Examples of  $Z\gamma\gamma$  production, through double ISR (a) and through ISR plus FSR (b). Quartic and triple neutral gauge couplings are forbidden in the SM

## 9.2 Selection

A selection strategy, similar to  $W\gamma\gamma$ , is used, except with cuts that preference the presence of a Z boson. Instead of a single lepton trigger, there is a double lepton trigger. For lepton object selection, both muons and electrons are required to be isolated. Muons must have a  $p_T > 10$  GeV and  $|\eta| < 2.4$ , and electrons a  $p_T > 10$  GeV and  $|\eta| < 2.5$ . Photons are required to have  $|\eta| < 2.5$ , and in a deviation from the  $W\gamma\gamma$  analysis, the photon  $p_T$  cut is reduced to 15 GeV.

For the event cuts, there must be exactly two opposite sign leptons and two photons. The selected particles are required to be separated with  $\Delta R$  cuts of 0.4. Again, events where both photons are reconstructed in the endcap are not used. Playing a similar role to the  $M_T$  cut, the  $Z\gamma\gamma$  analysis requires a lepton two-body mass,  $m_{\ell\ell} > 40$  GeV. The  $p_T$  of the lead lepton is required to be  $> 20$  GeV.



Region	jet misID	Diphoton	Total Background	Data	Expected Signal
Muon Channel					
Barrel-Barrel	$28 \pm 5$	$0.4 \pm 0.1$	$29 \pm 5$	72	$47 \pm 8$
Barrel-Endcap	$21 \pm 3$	$0.1 \pm 0.1$	$21 \pm 3$	29	$13 \pm 2$
Endcap-Barrel	$19 \pm 3$	$0.1 \pm 0.1$	$19 \pm 3$	40	$14 \pm 3$
Sum	$68 \pm 9$	$0.6 \pm 0.2$	$68 \pm 9$	141	$73 \pm 10$
Electron Channel					
Barrel-Barrel	$21 \pm 4$	$0.2 \pm 0.1$	$21 \pm 4$	65	$37 \pm 6$
Barrel-Endcap	$21 \pm 3$	$0.1 \pm 0.1$	$21 \pm 3$	28	$9 \pm 2$
Endcap-Barrel	$20 \pm 3$	$0.01 \pm 0.01$	$20 \pm 3$	24	$11 \pm 2$
Sum	$62 \pm 8$	$0.3 \pm 0.1$	$62 \pm 8$	117	$56 \pm 8$

**Table 9.1:** Estimated background events, observed data, and expected signal for the  $Z\gamma\gamma$  analysis. Results are separated by channel and photon region.

### 9.3 Backgrounds

The selected  $Z\gamma\gamma$  events are generally cleaner with fewer background sources. Within the analysis phase space, there is no source of three leptons, so there are no background from lost leptons or from electrons misidentified as photons. Again, the main background is from jet misidentified as photons. They are estimated using the two dimensional template method. There is also a small contribution from other diphoton processes, as with the  $W\gamma\gamma$  case, the contribution is estimated through simulation.

Table 9.1 shows a summary of the background estimates, expected signal, and selected events. The events are broken up between the electron and muon channel for the three categories based on the two photons' location.

### 9.4 Fiducial Region

Following the same procedure described in Section 6.5 the  $Z\gamma\gamma$  analysis measured a fiducial cross section for  $\sigma(pp \rightarrow \ell\ell\gamma\gamma)_{\text{Fiducial}}$ . Using generator level information, a fiducial region is chosen that mirrors the off-line selection cuts and is the

same for the electron and muon channels. The definition of the  $Z\gamma\gamma$  fiducial region is given in Table 9.2.

Definition of $Z\gamma\gamma$ Fiducial Region	
$p_T^\gamma > 15\text{GeV}$ , $ \eta^\gamma  < 2.5$	
$p_T^\ell > 10\text{GeV}$ , $ \eta^\ell  < 2.5$	
Exactly two candidate leptons and two candidate photons	
lead $p_T^\ell > 20\text{GeV}$	
$M_{\ell\ell} > 40\text{GeV}$	
$\Delta R(\gamma, \gamma) > 0.4$ , $\Delta R(\gamma, \ell) > 0.4$ , and $\Delta R(\ell, \ell) > 0.4$	

**Table 9.2:** Definition of the Fiducial Region used for the  $Z\gamma\gamma$  Cross-Section measurements.

The fraction of events where a  $Z$  decays to a  $\tau$  pair falls within the signal region is 0.3%. This is less than the  $W\gamma\gamma$  analysis, because in the  $Z\gamma\gamma$  scenario both taus must decay to the same type of lepton.

A fiducial acceptance factor is calculated following Equation 6.12. The ratio of  $\frac{C_{Z\gamma\gamma}}{1-f_\tau}$  and the systematic uncertainties are given in Table 9.3.

	Electron Channel	Muon Channel
$\frac{C_{Z\gamma\gamma}}{1-f_\tau}$	$22.5 \pm_{1.4}^{1.6} \%$	$29.1 \pm_{1.4}^{1.8} \%$

**Table 9.3:** For the  $Z\gamma\gamma$  analysis, total fiducial acceptance factor divided by  $1 - f_\tau$  for the electron and muon channels.

## 9.5 Systematics

Many of the systematics from the  $W\gamma\gamma$  analysis are also present in the  $Z\gamma\gamma$  analysis. The main sources of uncertainty again come from the limited statistics and from templates used for the jet misidentification estimate. New systematics are

calculated for the dilepton trigger, and instead of using a PSEV the  $Z\gamma\gamma$  analysis uses a Conversion Safe Electron Veto (CSEV). A summary of the systematics and their impact on the cross-section measurement are given in Table 9.4.

Systematic Uncertainties	$Z\gamma\gamma \rightarrow ee\gamma\gamma$	$Z\gamma\gamma \rightarrow \mu\mu\gamma\gamma$
Signal Simulation Systematics	$\delta(\sigma_{Z\gamma\gamma})$	
Simulation Statistics	3.25%	2.89%
Dilepton Trigger	1.33%	1.20%
Photon Identification	2.78%	2.82%
Muon Identification and Isolation		0.46%
Electron loose Identification	3.71%	
Photon Conversion Safe Electron Veto	0.76%	0.76%
Photon and Electron Energy Scale	2.52%	2.62%
Muon Energy Scale	–	1.60%
PDF	1.05%	1.11%
Renormalization and Factorization	0.55%	0.68%
Pile-up	1.31%	0.43%
Total Signal Simulation	6.60%	5.46%
Background Systematics	$\delta(\sigma_{Z\gamma\gamma})$	
Misidentified Jet	15.08%	12.51%
Other Multiboson Backgrounds	0.21%	0.26%
Total Background	15.08%	12.51%
Statistical Uncertainties	$\delta(\sigma_{Z\gamma\gamma})$	
Signal Region	16.54%	13.64%
Sidebands	1.39%	1.20%
Total Statistical	16.60%	13.70%
Total Systematic	16.46%	13.64%
Total Luminosity	2.60%	2.60%

**Table 9.4:** Systematic and statistical uncertainties affecting the  $Z\gamma\gamma$  fiducial cross section for events with a leading photon having  $p_T > 15$  GeV.

## 9.6 Results

For the BLUE combined electron and muon channels, the  $Z\gamma\gamma$  leptonic fiducial cross section is measured as:

$$\sigma_{Z\gamma\gamma}^{\text{fid}} \cdot \text{BR}(Z \rightarrow \ell\ell) = 12.7 \pm 1.4(\text{stat}) \pm 1.8(\text{syst}) \pm \text{fb}$$

Comparison with theory is made using the NLO prediction:

$$\sigma_{Z\gamma\gamma}^{\text{NLO}} \cdot \text{BR}(Z \rightarrow \ell\ell) = 12.95 \pm 1.47 \text{ fb}$$

The measurement is in strong agreement with the SM prediction, and has a significance over the background only hypothesis of  $5.9 \sigma$ .

## Chapter 10

### Conclusion

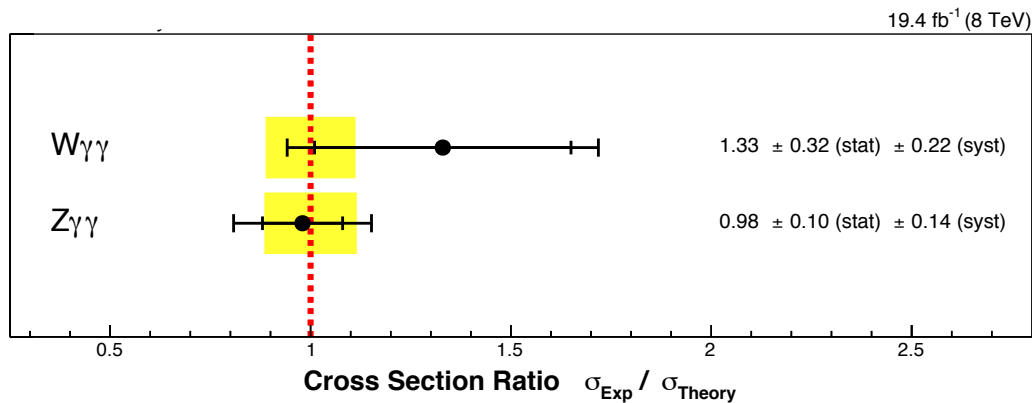


**Figure 10.1:** Ratio of the measured to theoretical cross sections for  $W\gamma\gamma$  and  $Z\gamma\gamma$ . Both cross sections are consistent with the SM prediction, the agreement for the  $Z\gamma\gamma$  measurement is particularly strong. The theoretical cross sections are calculated at NLO, the yellow band marks the theoretical uncertainties.

This dissertation presents a measurement of the  $W\gamma\gamma$  fiducial cross section,  $6.3 \pm 1.5(\text{stat}) \pm 1.1(\text{syst}) \pm 0.2(\text{lum})$  fb, that is in agreement with the SM prediction. The observed events are  $2.9 \sigma$  above the background only hypothesis. A measurement of the  $Z\gamma\gamma$  fiducial cross section is also presented,  $12.7 \pm 1.4(\text{stat}) \pm 1.8(\text{syst}) \pm \text{fb}$ , with a significance of  $5.9 \sigma$  and stringent agreement with the SM. For the two processes, Figure 10.1 shows the ratio of the measured cross sections to the theory prediction.

For the  $W\gamma\gamma$  measurement, new physics is searched for in the form of dimension-8 EFT. The analysis has particular sensitivity to the  $f_{T,0}$  coupling parameter and observed limits are set at:  $-35.9 < \frac{f_{T,0}}{\Lambda^4} < 36.7$ .

## Appendix A

### Appendix

#### A.1 Unitarity

Quantum mechanics requires that the S-matrix me unitarity. In most scattering experiments, the colliding particles pass by each other unaffected, so to leading-order the S-matrix is the identity matrix ( $I$ ). Interactions between the particles are described by the scattering amplitude ( $\mathcal{M}$ ). The unitarity condition can be re-written in terms of  $\mathcal{M}$ , giving the generalized optical theorem,

$$\mathcal{M}(i \rightarrow f) - \mathcal{M}^\dagger(f \rightarrow i) = -i \sum_X \int (2\pi)^4 \delta^4(p_i - p_x) \mathcal{M}(i \rightarrow X) M^\dagger(X \rightarrow i) \quad (\text{A.1})$$

Here,  $i$  is the initial state,  $f$  is the final state, and  $X$  are intermediate states [11] [12]. Decomposing  $\mathcal{M}$  into the angular momentum components, leads to a partial wave expansion where each term has its own unitarity requirement. Reworking the optical theorem, it can be shown that for a given center-of-mass energy ( $\sqrt{s}$ ) the total cross section has a maximum bound.

The calculation of this upper bound has been automated by the VBFNLO form factor calculator. The energy at which unitarity is violated is calculated for each of the analysis's observed 95% limits (See Table A.1). Bounds set for the

Coupling	Strength (TeV <sup>-4</sup> )	Unitarity Bound (TeV)
$f_{T0}$	37	2.3
$f_{T1}$	47	1.8
$f_{T2}$	100	2.0
$f_{M2}$	719	1.3
$f_{M3}$	1050	1.6

**Table A.1:** Unitarity bounds for the couplings considered in this analysis. Bounds are the vertex energy at which a theory with the given energy would violate unitarity.

$W\gamma W\gamma$  vertex using the  $W\gamma \rightarrow W\gamma$  process.

## A.2 Pseudorapidity

Pseudorapidity is closely related to the special relativity concept of rapidity, ( $\chi$ ). Rapidity comes from rewriting the Lorentz transformation matrix in terms of hyperbolic angles instead of velocities.

$$\Lambda = \begin{pmatrix} \cosh \chi & -\sinh \chi & 0 & 0 \\ 0 & 1 & 0 & 0 \\ 0 & 0 & 1 & 0 \\ 0 & 0 & -\sinh \chi & \cosh \chi \end{pmatrix} \quad (\text{A.2})$$

In the massless limit, pseudorapidity corresponds to the boost on a particle such that the resulting motion is perpendicular to the beam axis.

## A.3 Collision Energy Loss

When describing how particles interact with the electrons in a material, there is the energy,  $E$  and mass  $M$  of the incoming particle and the stationary electron

inside the material,  $m_e$ .

The maximum energy an incoming particle can lose in a single collision is defined by the equation [43]:

$$\Delta E = 2m_e \left( \frac{E^2 - M^2}{M^2 + m_e^2 + 2m_e E} \right) \quad (\text{A.3})$$

In the limit where  $M \gg m_e$  this reduces to  $\frac{4m_e K}{M} (1 + \frac{K}{2M})$ , where  $K$  is the kinetic energy of the incoming particle. Thus, the maximum possible energy loss is limited by the ratio of  $\frac{m_e}{M}$ . Looking at what this means for specific particles, in a single collision a muon ( $\mu$ ) can only lose  $\frac{1}{50}$  of its energy and a charged pion ( $\pi^\pm$ ) can lose only  $\frac{1}{70}$ .

#### A.4 Blue Combination

Table A.2 shows the NLO theory prediction for  $W\gamma\gamma$  events within the fiducial region at  $19.4 \text{ fb}^{-1}$ . Results are split between the electron channel, muon channel, and their blue combination. The sources of uncertainty used in the BLUE combination and whether or not they are correlated between the two channels is also included.

#### A.5 Optimization of Limit Setting

For the region used in the limit setting, a range of alternative lead photon  $p_T$  and the sublead  $p_T$  cut were scanned. Table A.3 show the observed and expected



	Correlated	Electron Channel	Muon Channel	Combined
Expected Events		92.23	92.89	92.43
MC Stat	False	$\pm 1.01$	$\pm 1.02$	
Factorization	True	$\pm 1.33$	$\pm 1.08$	
Renormalization	True	$\pm 7.02$	$\pm 7.07$	
PDF	True	$\pm 7.30$	$\pm 7.34$	
Total Systematic		$\pm 10.26$	$\pm 10.30$	$\pm 10.25$

**Table A.2:** Generator systematics for the expected number of  $W\gamma\gamma$  events at  $19.4\text{ fb}^{-1}$ . MadGraph NLO calculation. The electron and muon channel are combined using the BLUE method.

Subl Photon $p_T$ Cuts (GeV)	20	25	30	35	40
Expected	24.7	25.3	24.3	24.3	23.9
Observed	34.5	36.7	33.5	34.9	25.3

**Table A.3:** Expected and observed limits on  $f_{T,0}$  as a function of the sublead photon  $p_T$  cut

limits on the  $f_{T,0}$  parameter as a function of the sublead photon  $p_T$  cut. Since the improvements in the expected limits were small, we were conservative and stayed with the nominal cut values.

## Bibliography

- [1] Gargamelle Neutrino, F. J. Hasert et al., “Observation of Neutrino Like Interactions Without Muon Or Electron in the Gargamelle Neutrino Experiment,” *Phys. Lett.* **B46** (1973) 138–140.  
doi:10.1016/0370-2693(73)90499-1. 1
- [2] DELPHI, OPAL, LEP Electroweak, ALEPH, L3, S. Schael et al., “Electroweak Measurements in Electron-Positron Collisions at W-Boson-Pair Energies at LEP,” *Phys. Rept.* **532** (2013) 119–244, arXiv:1302.3415.  
doi:10.1016/j.physrep.2013.07.004. 2
- [3] CMS, S. Chatrchyan et al., “Observation of a new boson at a mass of 125 GeV with the CMS experiment at the LHC,” *Phys. Lett.* **B716** (2012) 30–61, arXiv:1207.7235. doi:10.1016/j.physletb.2012.08.021. 2
- [4] ATLAS, G. Aad et al., “Observation of a new particle in the search for the Standard Model Higgs boson with the ATLAS detector at the LHC,” *Phys. Lett.* **B716** (2012) 1–29, arXiv:1207.7214.  
doi:10.1016/j.physletb.2012.08.020. 2
- [5] O. J. P. Eboli, M. C. Gonzalez-Garcia, and J. K. Mizukoshi, “ $p p \rightarrow j j e^+ e^- \mu^+ \mu^- \nu \nu$  and  $j j e^+ e^- \mu^+ \mu^- \nu \nu$  at  $O(\alpha(\text{em})^6)$  and  $O(\alpha(\text{em})^4 \alpha(s)^2)$  for the study of the quartic electroweak gauge boson vertex at CERN LHC,” *Phys. Rev.* **D74** (2006) 073005, arXiv:hep-ph/0606118. doi:10.1103/PhysRevD.74.073005. 3, 17
- [6] LHCb, R. Aaij et al., “Observation of  $J/\Psi\rho$  Resonances Consistent with Pentaquark States in  $\Lambda_b^0 \rightarrow J/\Psi K^- p$  Decays,” *Phys. Rev. Lett.* **115** (2015) 072001, arXiv:1507.03414. doi:10.1103/PhysRevLett.115.072001. 6
- [7] CMS Collaboration, “Particle-Flow Event Reconstruction in CMS and Performance for Jets, Taus, and MET,” . 9, 47, 48, 49
- [8] S. Weinberg, “A Model of Leptons,” *Phys. Rev. Lett.* **19** (1967) 1264–1266.  
doi:10.1103/PhysRevLett.19.1264. 11
- [9] David Griffiths, “Introduction to Elementary Particles”. Wiley-VCH, 2008.  
ix, 12
- [10] C. Degrande, N. Greiner, W. Kilian, O. Mattelaer, H. Mebane, et al., “Effective Field Theory: A Modern Approach to Anomalous Couplings,” *Annals Phys.* **335** (2013) 21–32, arXiv:1205.4231.  
doi:10.1016/j.aop.2013.04.016. 16, 21
- [11] U. Baur and D. Zeppenfeld, “Unitarity Constraints on the Electroweak Three Vector Boson Vertices,” *Phys.Lett.* **B201** (1988) 383.  
doi:10.1016/0370-2693(88)91160-4. 19, 103

- [12] V. D. Barger, K.-m. Cheung, T. Han, and R. J. N. Phillips, “Strong  $W^+W^+$  scattering signals at  $pp$  supercolliders,” *Phys. Rev.* **D42** (1990) 3052–3077. doi:10.1103/PhysRevD.42.3052. 20, 103
- [13] L. Evans and P. Bryant, “LHC Machine,” *JINST* **3** (2008) S08001. doi:10.1088/1748-0221/3/08/S08001. 24, 25
- [14] CMS Collaboration, G. Bayatian et al., “CMS technical design report,” *J.Phys.* **G34** (2007) 995–1579. doi:10.1088/0954-3899/34/6/S01. 27, 29, 30, 34, 35
- [15] R. Wigmans, “Calorimetry,” *AIP Conf.Proc.* **674** (2003) 144–168. doi:10.1063/1.1604077. 31, 32
- [16] CMS Collaboration, C. et al., “Performance of CMS muon reconstruction in  $pp$  collision events at  $\sqrt{s} = 7$  TeV,” *J. Instrum.* **7** (Jun, 2012) P10002. 81 p. Comments: Submitted to the Journal of Instrumentation. 36
- [17] R. Brun and F. Rademakers, “ROOT: An object oriented data analysis framework,” *Nucl. Instrum. Meth.* **A389** (1997) 81–86. doi:10.1016/S0168-9002(97)00048-X. 40
- [18] CMS, S. Chatrchyan et al., “Performance of CMS muon reconstruction in  $pp$  collision events at  $\sqrt{s} = 7$  TeV,” *JINST* **7** (2012) P10002, arXiv:1206.4071. doi:10.1088/1748-0221/7/10/P10002. 42
- [19] CMS, V. Khachatryan et al., “Performance of Photon Reconstruction and Identification with the CMS Detector in Proton-Proton Collisions at  $\sqrt{s} = 8$  TeV,” *JINST* **10** (2015), no. 08, P08010, arXiv:1502.02702. doi:10.1088/1748-0221/10/08/P08010. 45, 46, 87
- [20] CMS, “Commissioning of the Particle-Flow reconstruction in Minimum-Bias and Jet Events from  $pp$  Collisions at 7 TeV,”. 46
- [21] M. Cacciari, G. P. Salam, and G. Soyez, “The Anti- $k(t)$  jet clustering algorithm,” *JHEP* **04** (2008) 063, arXiv:0802.1189. doi:10.1088/1126-6708/2008/04/063. 48
- [22] CMS, D. Dobur, “Jets and Missing Transverse Energy Reconstruction with CMS,” *PoS* **2008LHC** (2014) 039, arXiv:0904.0391. 50
- [23] M. L. Mangano, M. Moretti, F. Piccinini, R. Pittau, and A. D. Polosa, “ALPGEN, a generator for hard multiparton processes in hadronic collisions,” *JHEP* **07** (2003) 001, arXiv:hep-ph/0206293. doi:10.1088/1126-6708/2003/07/001. 51
- [24] J. Alwall, M. Herquet, F. Maltoni, O. Mattelaer, and T. Stelzer, “MadGraph 5 : Going Beyond,” *JHEP* **06** (2011) 128, arXiv:1106.0522. doi:10.1007/JHEP06(2011)128. 51

- [25] T. Sjostrand, S. Mrenna, and P. Z. Skands, “A Brief Introduction to PYTHIA 8.1,” *Comput.Phys.Commun.* **178** (2008) 852–867, [arXiv:0710.3820](#).  
doi:10.1016/j.cpc.2008.01.036. 51, 53, 64
- [26] T. Gleisberg, S. Hoeche, F. Krauss, A. Schalicke, S. Schumann, and J.-C. Winter, “SHERPA 1. alpha: A Proof of concept version,” *JHEP* **02** (2004) 056, [arXiv:hep-ph/0311263](#). doi:10.1088/1126-6708/2004/02/056. 51
- [27] A. Alloul, N. D. Christensen, C. Degrande, C. Duhr, and B. Fuks, “FeynRules 2.0 - A complete toolbox for tree-level phenomenology,” *Comput. Phys. Commun.* **185** (2014) 2250–2300, [arXiv:1310.1921](#).  
doi:10.1016/j.cpc.2014.04.012. 52
- [28] J. Alwall et al., “A Standard format for Les Houches event files,” *Comput. Phys. Commun.* **176** (2007) 300–304, [arXiv:hep-ph/0609017](#).  
doi:10.1016/j.cpc.2006.11.010. 53
- [29] Z. Was, “TAUOLA the library for tau lepton decay, and KKMC / KORALB / KORALZ /... status report,” *Nucl. Phys. Proc. Suppl.* **98** (2001) 96–102, [arXiv:hep-ph/0011305](#). [,96(2000)]. doi:10.1016/S0920-5632(01)01200-2. 53
- [30] A. Buckley, J. Ferrando, S. Lloyd, K. Nordstrom, B. Page, M. Rüfenacht, M. Schönherr, and G. Watt, “LHAPDF6: parton density access in the LHC precision era,” *Eur. Phys. J.* **C75** (2015) 132, [arXiv:1412.7420](#).  
doi:10.1140/epjc/s10052-015-3318-8. 54
- [31] GEANT4, S. Agostinelli et al., “GEANT4: A Simulation toolkit,” *Nucl. Instrum. Meth.* **A506** (2003) 250–303.  
doi:10.1016/S0168-9002(03)01368-8. 58
- [32] J. Alwall, R. Frederix, S. Frixione, V. Hirschi, F. Maltoni, et al., “The automated computation of tree-level and next-to-leading order differential cross sections, and their matching to parton shower simulations,” *JHEP* **1407** (2014) 079, [arXiv:1405.0301](#). doi:10.1007/JHEP07(2014)079. 52, 63
- [33] NNPDF, R. D. Ball et al., “Parton distributions for the LHC Run II,” *JHEP* **1504** (2015) 040, [arXiv:1410.8849](#). doi:10.1007/JHEP04(2015)040. 63
- [34] S. Frixione, “Isolated photons in perturbative QCD,” *Phys.Lett.* **B429** (1998) 369–374, [arXiv:hep-ph/9801442](#). doi:10.1016/S0370-2693(98)00454-7. 64
- [35] K. Arnold et al., “VBFNLO: A Parton Level Monte Carlo for Processes with Electroweak Bosons – Manual for Version 2.5.0,” [arXiv:1107.4038](#). 51, 81
- [36] D. Bourilkov, R. C. Group, and M. R. Whalley, “LHAPDF: PDF use from the Tevatron to the LHC,” [arXiv:hep-ph/0605240](#). 86

- [37] CMS Collaboration, “CMS Luminosity Based on Pixel Cluster Counting - Summer 2013 Update,” Technical Report CMS-PAS-LUM-13-001, CERN, Geneva, 2013. 86
- [38] ATLAS, G. Aad et al., “Measurement of the top pair production cross section in 8 TeV proton-proton collisions using kinematic information in the lepton+jets final state with ATLAS,” *Phys. Rev.* **D91** (2015), no. 11, 112013, arXiv:1504.04251. doi:10.1103/PhysRevD.91.112013. 86
- [39] L. Lyons, D. Gibaut, and P. Clifford, “How to combine correlated estimates of a single physical quantity,” *Nuclear Instruments and Methods in Physics Research Section A: Accelerators, Spectrometers, Detectors and Associated Equipment* **270** (1988), no. 1, 110 – 117. doi:http://dx.doi.org/10.1016/0168-9002(88)90018-6. 90
- [40] The ATLAS Collaboration, The CMS Collaboration, The LHC Higgs Combination Group, “Procedure for the LHC Higgs boson search combination in Summer 2011,” Technical Report CMS-NOTE-2011-005. ATL-PHYS-PUB-2011-11, CERN, Geneva, Aug, 2011. 92, 93
- [41] ATLAS, G. Aad et al., “Evidence of  $W\gamma\gamma$  Production in pp Collisions at  $s=8\text{TeV}$  and Limits on Anomalous Quartic Gauge Couplings with the ATLAS Detector,” *Phys. Rev. Lett.* **115** (2015), no. 3, 031802, arXiv:1503.03243. doi:10.1103/PhysRevLett.115.031802. 95
- [42] CMS, S. Chatrchyan et al., “Search for  $WW\gamma$  and  $WZ\gamma$  production and constraints on anomalous quartic gauge couplings in  $pp$  collisions at  $\sqrt{s} = 8\text{TeV}$ ,” *Phys. Rev.* **D90** (2014), no. 3, 032008, arXiv:1404.4619. doi:10.1103/PhysRevD.90.032008. 95
- [43] G. Knoll, “Radiation Detection and Measurement”. 2000. 105